Thesis for the Degree of
Master of Science

Thermoelectric Materials: Synthesis and Electrical Characterization

by

Xin Song

Master in Matrials, Energy and Nanotechnology
-Material Physics

Department of Physics

The Faculty of
Mathematics and Natural Sciences

University of Oslo

Oslo 2010

Thermoelectric materials: Synthesis and Electrical Characterization

by

Xin Song

Master Thesis

Materials, Energy and Nanotechnology - Material Physics
Department of Physics

Faculty of Mathematics and Natural Science
University of Oslo

December 1st, 2010

Abstract

The objective of the current work has been to synthesize the thermoelectric materials ZnSb with additions of Cr and Mn, respectively, and prepare the samples suitable for measurement of electrical properties and implement locally measurement techniques for the electrical characterization of these kind of samples.

ZnSb doped with 4% percentage and 0.5% percentage Cr and Mn, respectively, were studied in this master thesis. These additions to ZnSb have not been reported before. The materials were synthesized in annealing and reported a low ductility and more cracks. By contrast, the fine grains were found in the sintered materials and showed a high handleability. Samples were prepared as a bar-shape and disk-shape, respectively. The structures were studied by SEM (scanning electron microscope) and XRD (X-ray diffraction). The electrical properties investigation showed that the contact resistance was low, proved the reliability of measurements. By van der Pauw method, the resistivity of disk-shape samples was found around $2 \sim 2.5 \times 10^{-2}\Omega$cm in $Zn_{1-x}Cr_xSb$ and $1 \sim 2 \times 10^{-2}\Omega$cm in $Zn_{1-x}Mn_xSb$ at RT. The different pieces of materials have also given high values. The carrier type has been determined to be p-type by Hall measurement. The carrier concentration p for all samples are also similar $\sim 10^{17}\text{cm}^{-3}$ (RT), close to intrinsic value. The value of p, carrier concentration, is not proportional to the overall content of Cr and Mn, implying a low doping efficiency. Hall mobilities (RT) have been to determined in the range of 30$\sim$70 cm^2/Vs.The temperature-dependency of resistivity was measured in the range of 25$\sim$350°C by cryogenic measurement and showed a increase with temperature decrease. Thermal conductivity was measured by laser flash, reported at a range of 1.8$\sim$2.2$\text{WK}^{-1}\text{m}^{-1}$, which is comparable with those done by previous measurements. At the end of this thesis, there are also some interesting phenomena left. The temperature-dependence of resistivity leaves some interesting phenomena which cannot be interpret immediately. However, it could be an attractive topic to be researched in a large temperature range.

Foreword

I am pleased to introduce this master thesis, for the purpose of participate into the research of thermoelectricity. This thesis is the most important part of the study in physics materials in MENA (Materials, Energy and Nanotechnology) program at University of Oslo.

As the crisis of energy, thermoelectric materials plays more and more important role in the research of functional energy materials. I am proud of to denote myself to the study of this topic. As a candidate of thermoelectric material, ZnSb and its doped material have a lot of properties have not been discovered well yet. The experimental methods and their results are unknown as well. Therefore, this thesis is a great challenge for me. I intended to find out the better synthesis method to be suitable for the electrical characterizations at the beginning of my master work. There were a lot of practical and detailed issues. However, it was proved how important a good sample is to the reliable measurement. Building up the model of measurements was also a long but interesting term, which excited lots of fantastic ideas. Finally, analysis of those data and results was a seriously test for my whole master study. Even though, the whole process to build up the thesis was fruitful.

It is a helpful to refer to a lot of previous work. Some literatures gave me valuable informations and thoughts to construct the work of this thesis, for instance the model of electron poor framework semiconductor model by Hausserman et al. guided me to confirm the carrier type before other electrical properties.

Moreover but important, before readers start to go into this thesis, I would like to announce that all of the notation $Zn_{46}Cr_4Sb$, $Zn_{49.5}Cr_{0.5}Sb$, $Zn_{46}Mn_4Sb$ and $Zn_{49.5}Mn_{0.5}Sb$ in this thesis only the composition of samples, not the phases.

I am grateful to my supervisor, Terje Finstad, for the great helps in the whole process of the development of this thesis. Also I appreciate to Ole Bjørn Karlsen and PhD Michael Boettger for the helpful suggestions in the experiments. Also, I want to thank to support of Basic and Applied ThermoElectrics(BATE) group and peoples in MiNaLab those helped me to run the experiments and improved the thesis.

Xin Song
Oslo, Dec.2010

Contents

List of Figures

List of Tables

Chapter 1

Background on thermoelectricity and materials

1.1 Motivation to this topic

This work described in this thesis deals with characterization of materials that have a potential for thermoelectric applications. It is thus natural to introduce the reader, firstly, to thermoelectricity and, then, a short review of the status of knowledge and utilization of thermoelectric materials. Several recent reviews can be found in the literature [3][6][25], and the topic is described in textbooks[10][5] and the interested reader can find more extensive information there and in the references of the listed texts than what is provided in this short overview.

The main points, which this introduction tries to communicate, are that even thermoelectric materials have been know for a long time, they have not played any important role mainly in the contest of global energy management because of the low conversion efficiency of the materials. One can view this thesis as a part of a global effort to explore a more significant and wider utilization of thermoelectricity through research aimed at understanding of the materials.

1.2 History and development of thermoelectric materials

Theromoelectricity refers to a class of phenomena where electrical signals (electrical fields, current or charge) are generated by a thermal gradient or by a heat flow, or related phenomena observed by changing the stimuli and responses. There are large differences in the effects for different materials, and loosely speaking thermoelectric materials are those which have properties making an utilization attractive.

Thermoelectricity was discovered and described for a long time. However several breakthroughs have happened. With the attention of the current energy crisis, the research on thermoelectric materials has a renewed interest. The main advantage of thermoelectric technology are compactness, quiet, no moving parts, no pollution in the energy conversion process. Using the heat from our daily life, for instance exhausted from industries or the radioactive isotopes, even from solar system, the output are only electricity and heat.

Almost 200 years ago, in 1823, Seebeck found that an electrical field is induced when a temperature gradient is applied for a material; a voltage was measured between two different conductors when the junction between them was held at a different temperature than that of the measurement instrument. Following Seebeck's research Peltier did experiments on the thermal properties of materials, and found a variable temperature increase or decrease when he passed current in different directions between two conductors, so heat was liberated or absorbed in the process. Later, in 1851, Thompson (Lord Kelvin) found that a conductor carrying current in a temperature gradient can be heated or cooled. In 1854 he found the connection between the work of Seebeck and Peltier and the coefficients bearing their names by the application of equilibrium thermodynamics.(Today this relation is usually derived by the application of irreversible thermodynamics[5])

The earliest practical application of thermoelectricity appears to have been for refrigeration in the 1890s. The bottleneck is the lack of the good thermoelectric materials, which experiences a large Seebeck coefficient with low thermal conductivity and low electrical resistance, expressed by a parameter which is known as the figure-of-merit ZT. and this parameter is being using till now.

There was a large boost in research activity and progress following discoveries[5] of new semiconductors and their understandings around the 1950s. However the conversion efficiency was too low for a widespread utilization. Actually little improvements were made until the late 1990s with the nanotechnology age coinciding with the discoveries of some new materials. There is no fundamental limit - except the Carnot limit set by the 2nd law of thermodynamics - in respect to conversion efficiency. There is currently a large worldwide research effort with the ultimate goal of making thermoelectricity technology more attractive. The main effort is on materials research.

1.3 Physical principles

1.3.1 Seebeck effect

The Seebeck effect is the generation of an electrical field ε over a materials by the application of a thermal gradient ∇T. It is characterized by the Seebeck coefficient α defined by

$$\alpha = \frac{\varepsilon}{\nabla T} \tag{1.1}$$

or by the electrostatic potential difference ΔV over a materials with a temperature difference ΔT

$$\alpha = \frac{\Delta V}{\Delta T}. \tag{1.2}$$

The Seebeck coefficient, which can be positive or negative depending on the sign of the voltage, is considered a property of the materials. That is, generally, the case for a pure metal when it is allowed for the coefficient to be a function of temperature; for a semiconductor the Seebeck coefficient will depend upon the dopant concentration as well.

The qualitative explanation for the Seebeck effect is that heating of a region of the material will cause the charge carriers, i.e. electrons or holes, to flow out (or possibly in!) of the hot region. The change of the temperature gives rise to the kinetic energy, resulting in intense vibrations. When the kinetic energy is high enough to overcome the potential barrier, carriers have more possibility to make a excursion, creating a space charge, which will be accompanied by an electrical

field. The direction of the field will be such that it opposes the charge generated by the local rise in temperature.

Seebeck coefficient is an intrinsic property, i.e. it exists both in present and absent of the thermoelectric circuit. At a steady state with no external connection the net current will be zero and the electrical field generated will cancel the thermal gradient generated current. Zero net current is also the conditions used for measuring the Seebeck coefficient.

In most textbooks it is assumed that electrons will flow out of the hot region. This is similar to the behavior o a classical gas. However whether electrons will flow out or into the hot region depends upon a few factors[7]: i) the sign of the derivative of the density of states at the Fermi level with respect to the energy; ii) the energy dependence on the relaxation time of electrons. If we think of two parts of the materials side by side, the first factor has to do with how many states a hot electron can scatter into and the second factor has to do with how often a hot electron will scatter into the neighboring states. However these details are considered beyond the scope of the present thesis.

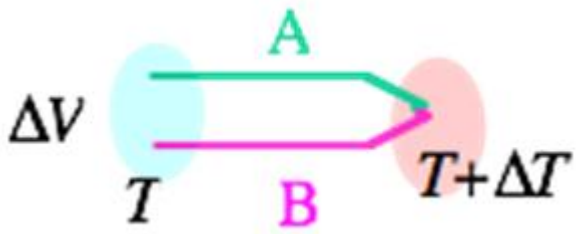

Figure 1.1: Schematic drawing of a thermocouple for Seebeck effect. Two different materials, A and B, are joined at a junction and the same temperature difference ΔT is applied over both materials.[7]

On usual, the Seebeck coefficient of a pair of materials is given, as being directly related to what can be measured with a thermocouple as shown in Fig.1.1. Then the Seebeck coefficient of a couple, α is given as the potential difference being proportional to the temperature difference:

$$\Delta V = \alpha_{AB}\Delta T = \alpha_A \Delta T - \alpha_B \Delta T \tag{1.3}$$

1.3.2 Peltier effect

The peltier effect is the generation of a temperature difference by applying a voltage between two electrodes connected to a material. This phenomenon can be used to transfer heat from one medium to another. For a thermocouple the effect can be parameterized by the Peltier coefficient, π_{AB}, defined by

$$I_{QAB} = \pi_{AB} I \tag{1.4}$$

where I is the electrical current and I_{QAB} (Q stands for heat) is the rate of heat absorbed or liberated at the junction between A and B, which is schematically drawn in Fig.1.2. Note that for the definition of the coefficient, the rate of heat is measured at zero difference of temperature; whilst in application such as cooling, it may be the development of a temperature gradient that is of interest.

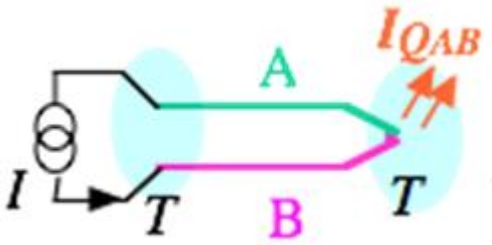

Figure 1.2: Schematic drawing of a thermocouple for Peltier effect. Two different materials, A and B, are joined at a junction and the same current is passed through them. Heat is released at the junction.[7]

When a DC voltage is applied to the electrodes to force electrical current through the semiconductor, thermal energy flows in the direction of the charge carriers. When there is no temperature difference, there is no heat absorbed in the conductor, except for dissipative heat loss by Joule heating. When the current passes through the circuit, the heat is absorbed or emitted reversibly at:

- the interface between two dissimilar conductor;
- non-homogeneous conductor with concentration gradient;
- the phase interface in multiphase materials

depending on the current direction.

1.3.3 Thomson effect

When an electric current is flowing through a conductor, an increase or decrease in the heat current follows along the conductor. The effect is characterized by the Thomson coefficient β, which is defined by

$$I_Q = \beta I \Delta T \tag{1.5}$$

where I is the electric current, I_Q is the heat current and ΔT is the temperature difference across the conductor. For a pair of different conductors we may have heat absorption or desorption for the different conductor as illustrated in Fig.1.3.

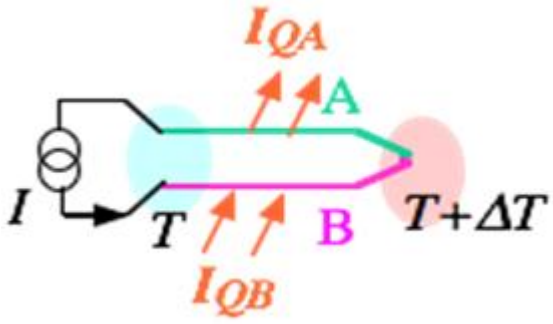

Figure 1.3: Schematic drawing of a thermocouple for Thomson effect. Two different materials, A and B, are joined at a junction and the same current is passed through them. When there is a temperature gradient in the wire then heat is accumulated or released along the wire. This is the Thompson effect and involves the heat that is not dissipated as Joule heat. The heat associated with the Peltier effect is omitted here.[7]

1.3.4 Figure-of-merit

The efficiency of a machine is usually defined as the amount of work which the machine can do per energy into the machine, so it is effective energy output divided by energy input. For a device which converts one form of energy into another, it is similarly the quotient between converted energy out divided by energy in. When a thermoelectric materials is used for producing electricity from a temperature

difference the efficiency is the electrical energy E_{out} output divided by the thermal energy (heat) input Q_{in}. Therefore from thermodynamics second law, we know that the maximum efficiency is the Carnot efficiency given by

$$\eta_C = \frac{E_{out}}{Q_{in}} = 1 - \frac{T_{low}}{T_{high}} = \frac{\Delta T}{T + \Delta T} \tag{1.6}$$

An actual device will have an efficiency smaller than the Carnot efficiency. Some reasons will have its origin in the practical design while others are limited by the thermoelectric materials itself. The parameters entering in the latter are grouped into a parameter called the "figure-of-merit" Z. Often, it is convenient to use a dimensionless figure-of-merit, which is defined by

$$ZT = \frac{\alpha^2 \sigma}{\kappa} = \frac{\alpha^2}{\rho \kappa} \tag{1.7}$$

where α is the Seebeck coefficient, ρ is the resistivity, σ is the electrical conductivity and κ is the thermal conductivity, which is contributed by both lattice thermal conductivity κ_l and electrical thermal conductivity κ_e. In the case or a pair of thermoelectric junction, which consists of n-type and p-type materials, the figure-of-merit is modified as:

$$ZT = \frac{(\alpha_p - \alpha_n)^2}{(\sqrt{\rho_p \kappa_p} + \sqrt{\rho_n \kappa_n})^2} \tag{1.8}$$

The intuitive understanding of the inclusion of these parameters are as follows: the larger the Seebeck coefficient, the larger the output of voltage and the larger the output of power. Some power is lost as Joule heat or resistive heat loss. Therefore the electrical conductivity should be as large as possible.The thermal conductivity is expected to be small in order to maintaining a large temperature difference. It preferred that the figure-of-merit is as large as possible and there is not established any fundamental limits as to how large it can be. ZT tells much of the usability of a materials, for instance how good a materials can perform as a cooler (i.e. Peltier element). It is usually desirable that this number is larger than 1 and of course preferably much larger than 1. The figure-of-merit of some thermoelectric materials will be presented in chapter 1.4.

Either increasing $\alpha^2\sigma$, called power factor, or decreasing κ can enhance the figure-of-merit. The power factor is performed as a function of carrier concentration. However, κ increased with respect to the increasing of conductivity σ due to κ_e. Therefore, some of researches devote to find the new materials with broadening

temperature range, especially at low temperature, as one part of the measurements in this thesis.

1.3.5 Thermodynamics of thermoelectricity

The thermoelectric parameters that have been introduced are related to each other. Their relationship can be derived by thermodynamics. Here we only state the relation instead of derive. Readers who is interested in can find more details in the textbook[5][28].

The relationship between Seebeck and Peltier maybe nest illustrated by Onsager relations. Let us consider a flow of electrical current I and an heat current I_Q through a conductor. The driving force for the electrical current is the gradient in the electrostatic potential φ plus the driving force for heat current is the gradient in temperature or conveniently the gradient in the logarithm to the temperature.

$$I = L_{11}\Delta\varphi + L_{12}ln\Delta T \tag{1.9}$$

$$I_Q = L_{21}\Delta\varphi + L_{22}ln\Delta T \tag{1.10}$$

L_{11}, L_{12}, L_{21}, L_{22} are then transport coefficients between conductors. The Peltier coefficient is found from the definition in section 1.3.2 and

$$\frac{I_Q}{I}\Big|_{\Delta T=0} = \pi = \frac{L_{21}}{L_{11}} \tag{1.11}$$

The Seebeck coefficient is defined by zero electrical current. Setting I=0 in equation (1.9) yields the potential gradient expressed by the temperature gradient and the transport coefficients:

$$I = 0 \Rightarrow \Delta\varphi = -\frac{L_{12}}{L_{11}}ln\Delta T \tag{1.12}$$

The coefficients L_{12}=L_{21}, as one Onsager relations

$$\Delta\varphi = -\frac{L_{12}}{L_{11}}ln\Delta T \overset{L_{12}=L_{21}}{=} \frac{\pi}{T}ln\Delta T = \alpha ln\Delta T \tag{1.13}$$

where shows the relation between π and α is

$$\alpha = \frac{\pi}{T} \tag{1.14}$$

If the Peltier coefficients for a pair of materials A and B are known as π_A and π_B, the relation is modified as

$$\frac{d\alpha_{AB}}{dT} = \frac{\pi_A - \pi_B}{T} \tag{1.15}$$

1.4 Common types of thermoelectric materials

Except for the metals used in thermocouples, which is a reliable way of measuring the temperature, most of the materials under consideration for energy conversion applications are semiconductors. Fig.1.4 shows the figure-of-merit of some of the materials that holds high ZT for different temperature ranges.

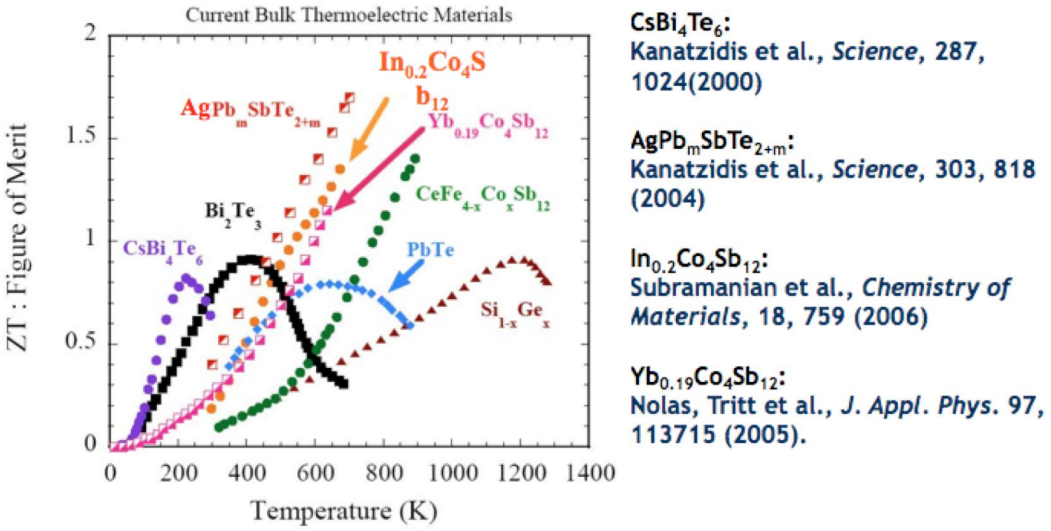

Figure 1.4: The figure-of-merit for some relatively recent developed bulk thermoelectric materials

It can be seen that ZT is above 1 for several materials. Here the Bi_2Te_3-, PbTe-compounds and the SiGe alloys are "traditional" semiconductors that have been around a long time and used in practical thermoelectric applications, while the others are new semiconductors.

The materials that are explored for thermoelectric applications are first of all aimed at having a large ZT. Several of these materials tend to have complicated crystal

structures with large units cells. These are characteristics compatible with low lattice thermal conductivity for varying reasons.

One interesting group of material sharing a common lattice structure are the Skutterudites based upon the crystal structure of $(Co/Ni/Fe)(P/Sb/As)_3$[28] with space group *Im3*. The unit cell of the structure contains "cages" which can be filled with guest interstitial atoms with the intention of creating localized vibrational modes which are efficient for scattering phonons so that the lattice thermal conductibvity can be reduced efficiently. These atoms are named 'rattlers' and a high mass and weak bonding to the atoms defining the cage are considered favorable[28]. Examples of these type skutterudites are $In_{0.2}Co_4Sb_{12}$[12], $Yb_{0.19}Co_4Sb_{12}$[22]. Since its thermal properties are similar with that of a glass and the electrical properties are similar with that of a perfect single crystal, which conforms to the requirement of poor thermal conductivity and good electrical conductivity. Hence Skutterudites is called phonon-glass-electron crustal as well

Another related class of materials are the clathrates [27] [21]. These also contain cages in their structures which can be filled with guest atoms as a means of providing phonon scattering and thus lower the lattice thermal conductivity.

Oxides are also potential thermoelectric materials. The lattice formed by the layered structure in homologous compound are considered being applied for high temperature within the thin layers, for instance $NaCo_2O_4$. The electrical conductivity is maintained while the thermal conductivity is lowered down. Another advantage of oxides is its enhanced thermal stability.

Antimonides has been researched as a candidate of thermoelectric materials for years. Zinc-antimony system is a good candidates for thermoelectric materials since its high figure-of-merit. The thermal conductivity can be decreased by reduced lattice conductivity due to the disordered crystal structure.

Nanostructures became an interest for thermoelectric materials. The thin film formed by superlattice, for instance PbTe/PbSeTe quantum dot has a enhanced ZT, approximately 1.5 at room temperature, than bulk structure. The silicon nanowires acts as efficient thermoelectric materials has the ZT=1.0 even is bulk silicon has a high thermal conductivity.

Other interesting materials have been studied by groups, for instance lead telluride, silicon germanium alloys, half-Heusler compound, metal silicide, Boron carbide, which is beyond this thesis. However, readers can refer to the reference for details[10][5][28].

1.5 A note on applications of thermoelectric materials

The most straightforward application is power generator and cooling system, which convert the heat into valuable energy by Seebeck effect and Peltier effect in the former case, respectively. For the many applications thermoelectric materials work as couples or they are put into modules. This usually involves alternating between n-type and p-type semiconductors as these have different sign of the Seebeck coefficient, thus the maximum difference between the Seebeck coefficients. An example of the construction of a Peltier element for cooling is shown in Fig.1.5.

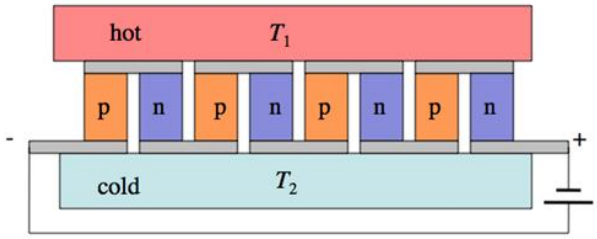

Figure 1.5: Schematic drawing of a Peltier element module[7]

The use of thermoelectric coolers in electronic instrumentation is common. Peltier elements offer a convenient way of cooling semiconductor detectors, for example photon detectors, thus achieving much higher signal to noise ratios, caused by the reduced reverse leakage at low temperatures. This is necessary for low band gap infrared detectors and allows photon counting in Silicon detectors. It is also used as cooling for devices that may require a stable operation temperature such as lasers.

The Peltier effect is employed in the domestic applications, particularly in the refrigerators. Compared with the vapor compressive refrigerators, the Peltier,

which is also called thermo-electric cooling (TEC), is much smaller.

Thermocouples are used in many industrial process monitoring and control, which slightly ironic ensures energy saving and efficient industrial processes. Thermocouples also find use in bolometers where many thermocouples are coupled in series to have a good sensitivity in measuring the temperature rise caused by absorption of infrared radiation by a small absorbing body(platelet).

Moreover, one of the thermoelectric modules based on Si-Ge have been developed for gasoline engine, by which uses the waste heat from the exhausted gas, resulting in a reduction of the fuel consumption by approximately 10%.

Similar model is called HVAC (heat, ventilation and air conduction). Which applied for the hybrid vehicles, to generate an electrical potential with an combination of n-type and p-type by means of exchanging the liquid heat and air heat.

Micro-electromechanical system(MEMS) provides a series of good methods to make the micro thermoelectric generators (μTEGs), which can widely used in the microelectronic components. A prominent technique is flexible μTEGs chip processing, which consists of electrochemical deposition, photolithography and etching steps. A good materials is $Bi_{2+x}Te_{3+x}$.

A more sophisticated research on thermoelectricity is the radioisotope thermoelectric generator, abbreviated RTG, with which the heat is released by the isotopes decay, and then it is converted into energy by the Seebeck effect. It is poplar applied for the cosmos science to supply energy to space station or satellites. The same technology with radioactive heating has also been used in remote areas, for instance light houses along the coasts which is fairly attractive.

It should be emphasized that while there is a strong need to make more efficient thermoelectric materials with better figure of merit yielding better energy conversion efficiency and better cooling efficiency, there are several application areas where this is not a considered a big issue. In a global energy aware society the economics of efficiency is very important as are the hazards of pollution, but for niche applications the efficiency may not be that important.

To give one example : platinum is one part of a widely used high temperature thermocouple used as temperature sensor. The reliability and stability are the major strength. It efficiency are ,however, poor. The Seebeck coefficient of Pt is around 5.15 μV/K at 300 K [20], the electrical resistivity is 105 nΩm and the thermal conductivity 71.5 W$\cdot$(mK)$^{-1}$ so the dimensionless figure-of-merit ZT is around 1×10^{-3} at 300K which is very low compared to the values for ZT for the most efficient materials presented in section 1.4.

Chapter 2

Introduction of semiconductor materials

2.1 Motivation of introduction to semiconductor

The materials that are investigated in this thesis are considered semiconductors. Beyond that the materials have a priori unknown electronic structure and characteristics. Therefore some concepts from semiconductor theory are useful for describing and interpreting the measurements. The basics of semiconductors can be found in most introductory texts on solid state physics [31], materials science[4] and electronic devices[31]. and here is only included a minimum. It is assumed that the reader is familiar with concepts such as density of states, band gaps and charge carriers. It is considered helpful for later descriptions to define some concepts such as "'idealized semiconductor" as these will be used through the discussion without every time repeating the definition.

The current research on thermoelectric materials is interested in semiconductor. In fact, it took many years to find good thermoelectric materials till Abraham Ioffe discovered the good thermoelectric performance from the research on doped semiconductor in 1950s. Bi_2Te_3 showed the much larger thermoelectric effect at room temperature than metals. It, in further, led to the interests of research on

binary semiconductor.

It is observed that the Seebeck coefficient is low in metal which is of order of 1 to 10 μV/K; whilst it is much larger in semiconductor which is of order of 102 to 103 μV/K. As the properties of semiconductor mentioned in last section, it is realizable to maximize the electrical conductivity in high temperature by doping. In metals, the electrical conductivity decrease with temperature increasing depends on the current goes through. Since the motion of conducting electrons become more random due to gaining the more kinetic energy, the lifetime of free electrons is shortened. As a result, the electrical conductivity is declined. However, in the case of semiconductor, with the temperature increase, more electrons in valence band are excited into conduction band. Both the hole they left behind in valence band and themselves participate in the charges carrier. Consequently, attributing to the enhancement of carrier concentration, the electrical conductivity is turned up. Furthermore, the thermal conductivity can be diminution by reducing the lattice thermal conductivity, thereby optimizing the figure-of-merit. Additionally, a high charge mobility is required so as enhance the electrical conductivity. This, of course, can be achieved by semiconductor rather than other materials.

2.2 Basis of semiconductors: idealized semiconductor

Solids are categorized as a conductor, semiconductor or insulator dependent on the value of the electrical conductivity. Many semiconductors share other common characteristics. Here is introduced an idealized semiconductor, IS, with many of the characteristics found approximately in Si and GaAs which are common semiconductors for electronic devices. An IS has a band gap with no electron states. The valence band states are completely delocalized as are the conduction band states. The conductivity of an IS can be varied by many orders of magnitude by doping and by varying the temperature. Doping an IS is done by adding atoms that each either donates an electron to the conduction band, a donor, forming n-type semiconductor, or accepts an electron from the valence band, an acceptor, forming p-type semiconductor, and thus contributes a hole to the valence band. The ionization energy of the donors and acceptors in the IS are small compared

to thermal energy k_BT.

In an IS the electrons occupying states around the minimum of conduction band are well described by the effective mass approximation as are holes near the top of the valence band. Fig.2.1 shows the density of states as a function of energy for an IS. The conduction band and valence band are equal for an IS but have energy states.

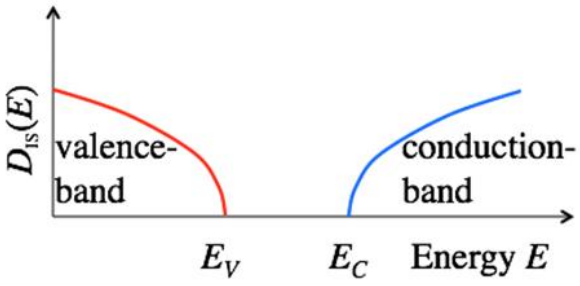

Figure 2.1: Schematic drawing of the density of states for an idealized semiconductor as a function of energy.[7]

The density of states is proportional to the square root of the energy E

$$D_{IS}(E) = \frac{1}{2\pi^2}\left(\frac{2m^*}{h^2}\right)^{\frac{3}{2}} E^{\frac{1}{2}}, \tag{2.1}$$

where m^* is effective mass and the band edge is at E=0 for convenience. There is only one single band contributing states to IS. Further the density of states effective mass is equal to the acceleration of effective mass.

2.3 Carrier concentration

The charge carriers in the idealized semiconductor can be electrons or holes and contributes to the electrical conduction. At T=*0* there are no free carriers. Electrons can be thermally excited to the conduction band from the valance band or from donor levels. The concentration of electrons n is given by

$$n = \int_{CB} D(E) f(E, E_F) dE \tag{2.2}$$

where "CB" stands for conduction band, E_F is the Fermi level and *f(E,E_F)* the Fermi-Dirac distribution function. The integration is over the whole band. For an IS the electron concentration is given by

$$n = \int_0^{\pi} D_{IS} f(E, E_F) dE \overset{E_c - E_F \gg k_B T}{=} N_c exp\left(- \frac{E_c - E_F}{k_B T} \right) \tag{2.3}$$

where

$$N_c \equiv 2\left(\frac{2\pi m^* k_B T}{h^2} \right)^{\frac{3}{2}} \tag{2.4}$$

where E_c is the conduction band minimum and N_c is called the effective density of states of the conduction band. The last form in equation (2.3) applies for moderate, non degenerate doping and involves using the Maxwell-Boltzmann approximation to the Fermi-Dirac distribution. Equation (2.3) may not be directly applicable for the parameter space where thermoelectric materials are most efficient in application, but may apply to the characterization of materials.

As can be seen from (2.2) or (2.3), in order to calculate the carrier concentration one must be known is the Fermi level, E_F. The Fermi level can be found in equilibrium by the application of the law of mass action and by the charge neutrality principle, expressed respectively as

$$n \cdot p = n_i^2 \tag{2.5}$$

and

$$n + N_A^- - p + N_D^+ = 0 \tag{2.6}$$

where p is the hole concentration, and N_A^- andN_D^+ are the ionized acceptor and donor concentration respectively. Alternatively, n can be measured and other parameters entering into the formulas are determined. Fig.2.2 shows n as a function of T for n-type silicon. In the case of n-type semiconductor, if the donor concentration is not too different in magnitude from the intrinsic carrier concentration, the thermal equilibrium concentration is influenced by the intrinsic carrier concentration. However, if the semiconductor is heavy doped, i.e.$N_D \gg n_i$, the electron concentration is essentially equal to the donor concentration.

The best thermoelectrical performance for a semiconductor is achieved at fairly high doping concentrations. Thus it is in place to consider the case of a degenerate semiconductor. For a degenerate semiconductor the Fermi level will be positioned in the conduction band for an n-type semiconductor and in the valence band for

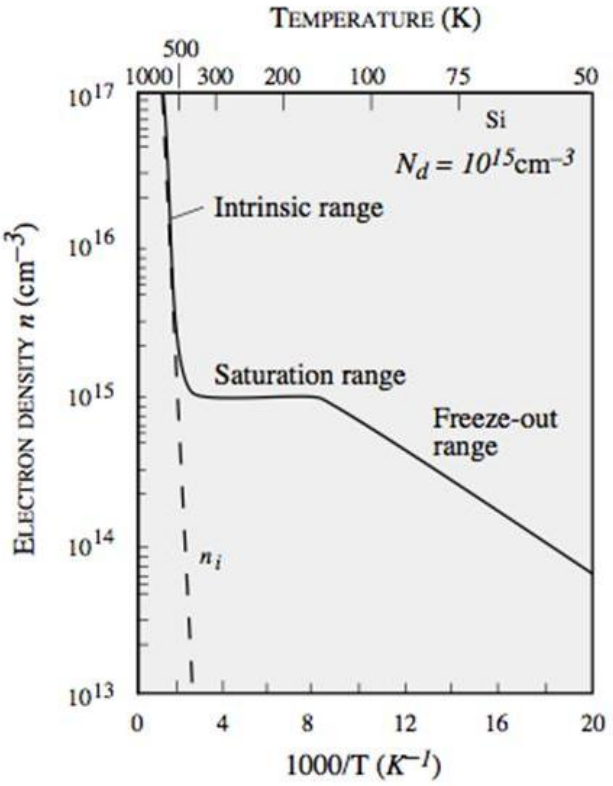

Figure 2.2: Electron density as a function of temperature for a Si sample with donor impurity concentration of 10^{15}cm^{-3}. It is preferable to operate devices in the saturation region where the free carrier density is approximately equal to the dopant density.

a p-type semiconductor, see Fig.2.3. In a real semiconductor the high doping and carrier concentration will have a significant effect on the density of states (Delocalized band tales into the band gap due to interactions between the carriers and smearing of the donor levels to a band of localized states merging with the conduction band.) It is however possible to consider an idealized semiconductor to not including these high doping effects.

2.4 Carrier mobility

The current density j of an extrinsic (here n-type) semiconductor subjected to an electrical field ε is given by

$$j = qnv_d \tag{2.7}$$

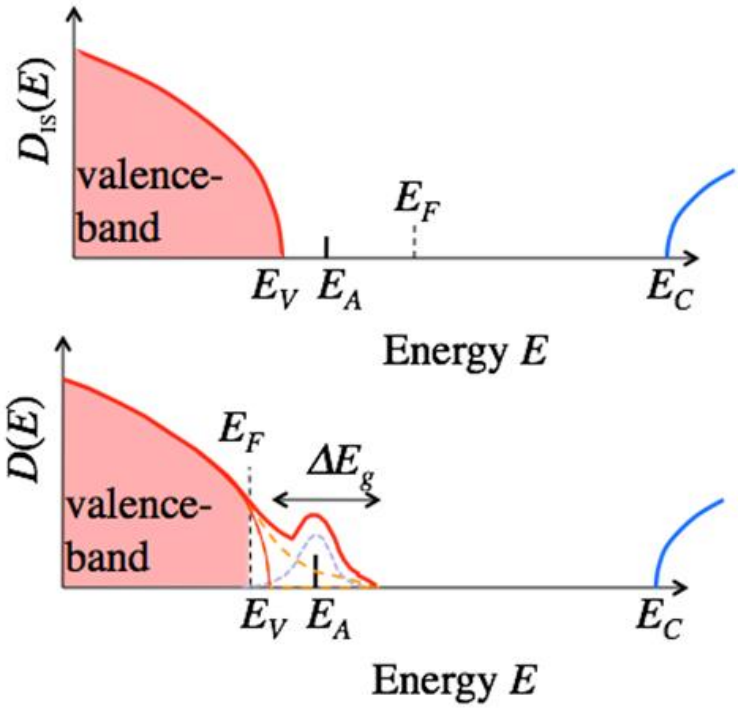

Figure 2.3: Schematic drawing of the density of states vs energy. The valence band is shown (left solid line) and a small portion of the conduction band (right solid line). At the top: An idealized semiconductor with a small acceptor doping concentration with a level at E_A. At the bottom: Schematic drawing of the situation with heavy doping showing delocalized band tail states due to interactions in between holes (dash line) and smearing of the localized acceptor states due to acceptor state interactions (dash line above E_A).[7]

here, the conductivity σ and mobility has such relation

$$\sigma = qn\mu \tag{2.8}$$

where μ is the carrier mobility, v_d is the drift velocity of the electron (average velocity of all carriers). The mobility is thus an important parameter for a semiconductor. It is the charge carrier drift velocity per unit field, which is indicated from equation (2.7) and (2.8) $\sigma = \frac{v_d}{\varepsilon}$ and it is related to the ionization energy in doped semiconductor. Particularly, in heavy doped semiconductor, the mobility decreases obviously due to the ionized doping atoms. However, in light doped semiconductor, it is almost constant and it is dominated by the phonon scattering. In the case of intrinsic semiconductor, the mobility, on the other hand, depends upon the effective mass of the charge carrier and upon the scattering of charge

carriers. There are several charge carrier scattering mechanisms which depends differently external parameters such as doping, temperature, and defects.

2.5 A note on polycrystalline semiconductors

The semiconductors investigated in this thesis are considered polycrystalline, while the treatment above on idealized semiconductors are primarily for single crystalline material and the parameters considered to be specific material parameters are generally single crystal. The electrical properties of polycrystalline semiconductors can in general be quite different than that of single crystal material. For example for Si the resistivity can be different by orders of magnitude for the same doping concentration is briefly sketched in Fig.2.4, which is a summary of the electrical properties of polycrystalline material based upon existing models for Si is given in the model of Wu and Ken[37].

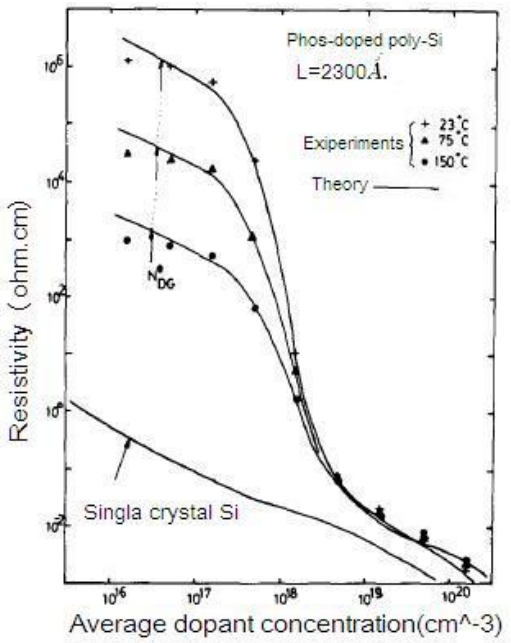

Figure 2.4: The variation of the resistivity with respect to average dopant concentration and temperature for the fabricated phosphorus-doped polysilicon film resistors with the grain size of 2300Å.[37]

Obviously if a single crystal shows anisotropy, then the anisotropy in a polycrystalline material is likely weaker or absent. Another, less predictable effect, is the effect of the grain boundaries surrounding each crystallite. They will obviously contribute to scattering of both electrons and phonons. Thus the mobility and the thermal conductivity will be influenced by grain boundaries.

The grain boundaries may additionally contain localized electron states. These electron states may trap free carriers. Trapped carriers will charge the grain boundary and repel other free carriers; a depletion region surrounding the grain boundary is thus created. The width of this depletion region depends upon the doping concentration. For light doping the depletion region will be large and the the complete grain may depleted of free carriers. For heavy doping the depletion region is smaller. So for light and moderate doping the grain boundaries will greatly influence the number of carriers that can participate in the conduction; the effective carrier density is influenced.

A further effect of localized grain boundary electron states is that an energy barrier may arise as a consequence of charge trapping, pinning of the Fermi level at the grain boundary and electrical field in the depletion region. The carriers will have to pass above this energy barrier in order for current to flow from one grain to the next. This energy barrier will reduce limitation of the mobility and yield a higher resistivity compared to no barrier.

Finally the grain boundaries may trap dopant atoms during heat treatment, by doping atoms diffusion and segregating in grain boundaries. The final conclusion is that the electrical properties of polycrystalline material can not be reliably predicted from that of bulk material. It can be influenced by several factors that are typically not well characterized for many materials such as grain boundary states.

2.6 Thermoelectric parameters

The dimensionless figure of merit, ZT, was introduced in section 1.3.4. It can be calculated for semiconductors if the thermal conductivity is given. It is beyond the

scope of the current thesis to analyze critically the models for these calculations, and here is only referred to the results of the simple model for semiconductors. Clearly an important parameter is the Seebeck coefficient, α, for an idealized (non degenerate) semiconductor is given by [9]

$$\alpha = \mp\frac{k_B}{q}\left\{\eta - \left(r + \frac{5}{2}\right)\right\} \tag{2.9}$$

where the plus sign is for electrons, minus for holes and η is the reduced Fermi energy given by

$$\eta = \frac{E_F - E_0}{k_B T} \tag{2.10}$$

in which either E_0=E_v for p-type orE_0=E_c for n-type. The most essential additional assumption and simplification made is perhaps the energy relaxation approximation. The factor r is considered a characteristic for the scattering process and that the energy relaxation time τ can be written on the form:$\tau(E) = \tau_0(E - E_0)^r$, where τ_0 and r are constants.The former depends upon the particular scattering process while the later depends upon both the scattering processes and material properties. It is usual to consider values of r equal to -$\frac{1}{2}$, 0, +$\frac{1}{2}$, +$\frac{3}{2}$ for the scattering from acoustic lattice vibrations, neutral impurity atoms, strongly screened impurity atoms and ionized weakly screened impurity atoms respectively [25]. So in the case of a p-type IS where acoustic phonon scattering dominates equation (2.9) can also be written as

$$\alpha = \frac{k_B}{q}\left(ln\frac{p}{N_v} - 2\right) \tag{2.11}$$

whereN_v is the (temperature dependent) effective density of states of the valence band defined quite analogous to N_c defined in equation (2.4).

The phonon drag effect on the Seebeck coefficient also has to be considered [25]. It is caused by phonon-electron interaction and will have the strongest influence at a temperature around 1/5 of the Debye temperature. It is weaker at lower temperatures as a consequence of fewer phonons and again weaker at higher temperature because phonon-phonon interactions are then dominating momentum exchange. The phonon drag is caused by the phonons not being in local thermal equilibrium. The phonons lose energy by scattering mechanisms. When phonon-electron interactions are dominating, momentum is transferred to charge carriers which then are dragged along with the phonons. This cause of redistribution of carriers comes in addition to the other processes found in the Seebeck effect and enhances it. This effect has been observed in lightly doped (10^{15}cm^{-3}) Ge at temperatures below

15 K, leading to the following optimization of a semiconductor. This requires one knows the parameters entering and know how to manipulate them in practice. That is not possible for the materials under investigation in this thesis.

2.7 Effect of nanostructuring

As mentioned in section 1.4 there is an activity on nanostructuring as a means of obtaining a good thermoelectrical material. One of the philosophies is to use that as a means of increasing the phonon scattering in the material and thus minimize the thermal conductivity. Another philosophy is to radically change the density of states by quantum confinement and in such a way that the Seebeck coefficient is increased. Finally nanostructuring which achieve energy filtering of the electrons can enhance the efficiency. The enhancement of density of states near Fermi level induced by nanostructuring leads to a large Seebeck coefficient. And the boundary scattering affected can bring about phonons more than electrons or holes. These approaches have been presented and discussed by several authors [3, 6, 25, 10, 5] and the last two approach which actively addresses the charge transport will be mentioned.

The Seebeck coefficient can be made large by having a density of states with the maximum asymmetry around the Fermi level, as large as possible density of states just above the Fermi level and small below. The states that will contribute most (per state) to the Seebeck coefficient are those located on the order of kT above the Fermi level. States far from the Fermi level do not contribute to the Seebeck coefficient. It has been the aim of many research efforts to find and to synthesize a material that has these features i.e. a density of states with i) an asymmetry around the Fermi level; ii) a large change with energy around the Fermi level; iii) a very high density just above the Fermi level. Changing the dimensionality of the system offers another degree of freedom for achieving this. Actually any semiconductor with carrier confinement in one direction will have a density of states curve have large spikes. These are called one-dimensional conductors, 2-D conductors, or quantum strings.

2.8 Effect of resonant states

Another way of enhancing the Seebeck coefficient of a semiconductor besides nanostructuring is by doping by elements yielding bumps/peaks in the conduction band. This have been reported by group III elements in VI-VI semiconductor such as PbTe, shown in Fig.2.5.[13] While the exact reason for the change of density of states and its systematics appears to be not well understood. The reason for the enhancement of the Seebeck coefficient with these bumps in the density of states becomes clear from the Mott relationship for α

$$\begin{aligned} \alpha &= \frac{\pi^2}{3}\frac{k_B}{q}k_BT\left\{\frac{d\Big[ln\Big(\sigma(E)\Big)\Big]}{dE}\right\}_{E=E_F} \\ &= \frac{\pi^2}{3}\frac{k_B}{q}k_BT\left\{\frac{1}{n}\frac{dn(E)}{dE}+\frac{1}{\mu}\frac{d\mu(E)}{dE}\right\}_{E=E_F} \end{aligned} \tag{2.12}$$

where *n(E)* is the contribution to the carrier concentration from the states with energy E and μ*(E)* is the contribution to the mobility from the carriers with energy *E*.

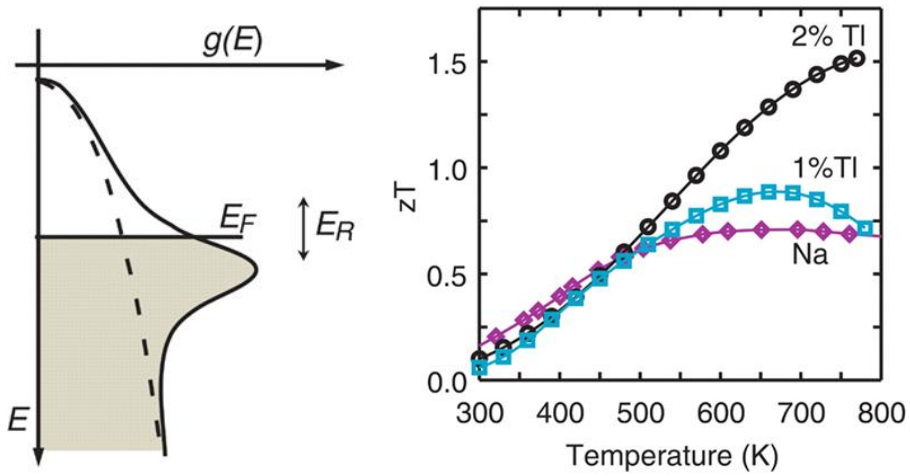

(a) (b)

Figure 2.5: Schematic representation to the effect of resonant states. (a) density of electron states of the valence band of pure PbTe (dash line) contrasted to that of Tl-PbTe in which a Tl-related level increases the density of states. The figure of merit ZT is optimized when the Fermi energyE_F of the holes in the band falls in the energy range E_R of the distortion. (b) The ZT values for $Tl_{0.02}Pb_{0.98}Te$ (circle dots) and$Tl_{0.01}Pb_{0.99}Te$ (square dots) compared to that of a reference sample of Na-PbTe (diamond dots) From Heremans et al. [13]

Chapter 3

Introduction to zinc antimony systems: previous research work

3.1 Motivation of this chapter

The purpose of this chapter is a review of synthesis and measurements of electrical properties of zinc-antimony(ZnSb) alloys and it with small additions of other elements to find what the effects of these elements has on the electrical properties in the previous work. The compound ZnSb has been reported in the literatures and studied for years. These informations are valuable to provide a source of reference so that we can expect some observations during experiments. Before this thesis work it was also unknown what would be the result of the synthesis process and measurement techniques used even for the pure compound. First we will give a introduction from phase diagram and bonding structure. The following part is about the research in terms of electrical properties. Comparison with previous work will also be a natural part of the chapters on discussion of results. At the end a briefly note on Zn_4Sb_3 will be presented since it possesses similar properties in certain points.

3.2 Zn-Sb phase diagram

It is a good way to start with the binary phase diagram for understanding the crystalline of zinc antimony system. Fig.3.1 shows the binary phase diagram of Zn-Sb[16]. We can consider the left part of phase diagram as a separate binary

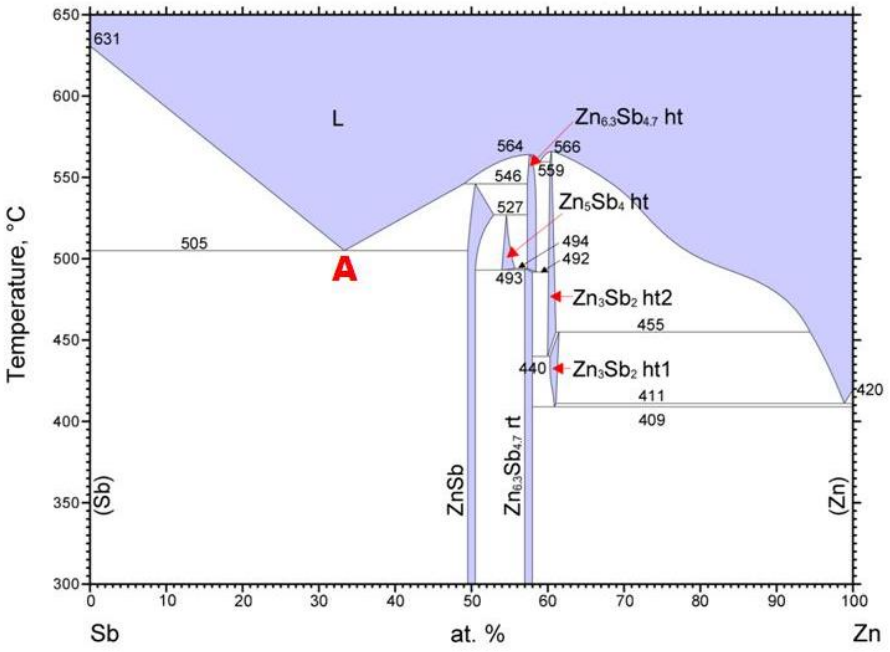

Figure 3.1: Binary phase diagram of Zn-Sb[16]

system, which consists of (Sb) and ZnSb. The temperature of solidification is within a range between 631°C and 505°C. The point "'A" represents the eutectic temperature $T_{(Sb)-ZnSb}$=504°C where the reaction L $\rightarrow$ (Sb) + ZnSb. The right part is more complex. The phase, which is often called Zn_4Sb_3 in literatures, can exist in two forms, labeled as $Zn_{6.3}Sb_{4.7}$ht and $Zn_{6.3}Sb_{4.7}$rt .

There are two categories of crystal growth, which are growth from stoichiometric melts or growth from non-stoichiometric melts. The former one is that the nucleation starts from the nucleus which has the same or similar composition with the final crystal. And the later one has opposite phenomena and the crystal will experience a phase transition, which is applied for the crystalline in this thesis.

From Fig.3.1, it is indicated that for the composition of 50%Sb and 50%Zn, when

the temperature declines after melting, ZnSb is not the first phase to crystallize.A cooling leads to the composition forms Zn_4Sb_3. Afterwards, these crystals react with the melts and transfer to ZnSb at 545°C by peritectic reaction$Zn_4Sb_3 + L \rightarrow$ ZnSb. However, this peritectic reaction would not occur if the cooling is instantaneously during quenching, thereby causing the non-equilibrium of the solids, which is shown in Fig.3.2. As a consequence, the solids includes three phase: (Sb), ZnSb and Zn_4Sb_3.

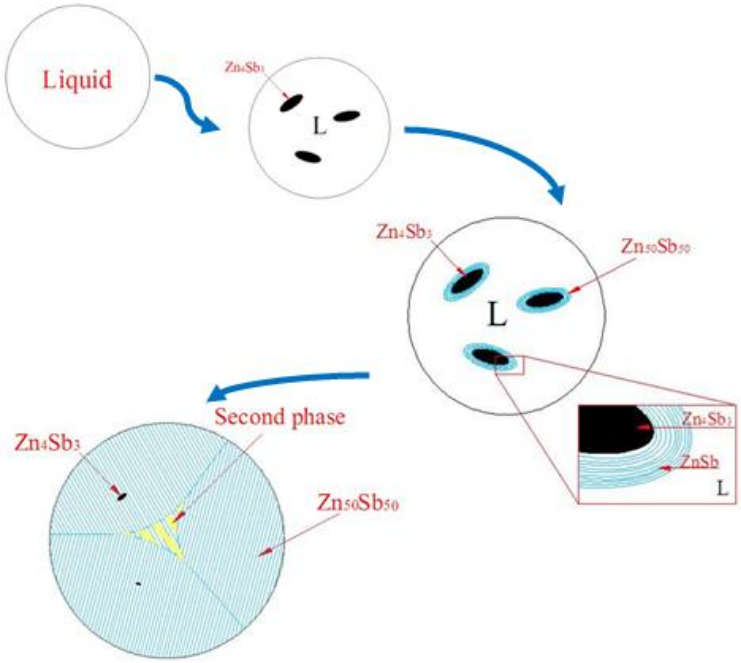

Figure 3.2: Schematic drawing of crystalline process of $50\% - 50\%$Zn-Sb binary system.Zn_4Sb_3 forms firstly. With temperature decrease, ZnSb crystallize. Zn_4Sb_3 acts like a core surrounded by ZnSb. If the cooling occurs instantaneously, Zn_4Sb_3 core left in the solid.

In the processes of annealing following the melting and quenching, the Zn_4Sb_3 nucleus experience a phase transition, transferring into ZnSb. The furnace keeps the temperature at 400°C. Solids tries to get an uniform phase to get equilibrium. Zinc atoms in Zn_4Sb_3 phase diffuse out and go into ZnSb phase surrounding the Zn_4Sb_3 nucleus. Eventually, the incursion of Antimony and spill of Zinc make the same composition of the phase, and nucleus disappear. As a consequence, the phase approaches uniform theoretically. Fig.3.3 shows the diffusion of atoms of Zinc and Antimony. In the case of sintering, atoms diffuse not only into the grain

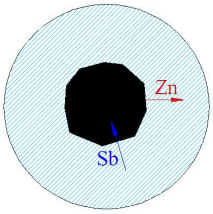

Figure 3.3: Schematic drawing of diffusion of zinc and antimony atoms. Inner: Zn_4Sb_3. Outer: ZnSb. To form the equilibrium state, zinc atom diffuses out from the inner core of Zn_4Sb_3 while antimony atom in the outer phase of ZnSb diffuses in.

boundary, but also between the boundaries due to a high pressure. However, due to the grain size is smaller by sintering, the diffusion distance is shortened. We will cover more details about annealing and sintering in Chapter 4.2.

When the samples have more than two components, it is helpful to use the ternary phase diagram. However, we will come to more details to discuss the composition with ternary phase diagram in Chapter 5. In this section, we only give a presentation to show the compositions given by the system as an example of $Zn_{46}Mn_4Sb$, shown in Fig.3.4.

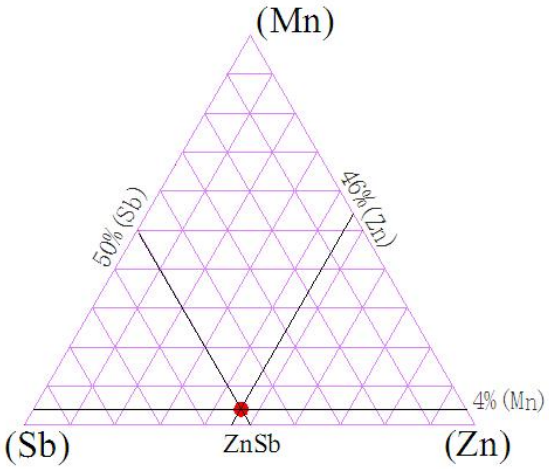

Figure 3.4: Ternary phase diagram of $Zn_{46}Mn_4Sb$. The atomic percentage in labeled on the diagram. The cross point is the final equilibrium phase.

3.3 Zn-Sb crystal structure bonding

The crystal structure of ZnSb is given by Almin[2] who reported it to be orthorhombic and belong to space group P/bca in 1948. Figure 3.5 shows the unit cell of ZnSb based upon the data given by Almin[2]. It has the similar structure with CdSb which is orthorhombic symmetry. The crystal lattice belongs to D_{2h}^{15} space group, processing two-fold screw axes C2x, C2y and C2z, which are parallel to the crystal axes. The Brillouin zone is a rectangular parallelepiped. The dimensions of ZnSb are suggested:

$$\text{a=6.218Å, b=7.741Å, c=8.115Å}$$

There are different ways to reveal the characteristics of the lattice and rationalize the basic building blocks. Two different ones regard the basic building blocks as either

- tetrahedra of $ZnSb_3$ and Zn_3Sb
- Zn_2Sb_2 polygons

They are presented in chronological order in the following. Each atom is surrounded by 4 other making up a distorted tetrahedron. Each Zn has three Sb and one Zn nearest neighbor. These four atoms construct a deformed tetrahedron. Likewise Sb has three Zn and one Sb nearest neighbor. The structure can roughly be described as a distorted diamond lattice. The position of each atoms are

Zn: 0.461 0.103 -0.122
Sb: 0.142 0.081 0.111

Viewed this way the building blocks of the compound are units of $ZnSb_3$ and Zn_3Sb. It may be the easiest to visualize this by a mapping of the structure to two dimensions retaining the interatomic spacing and the given number of nearest neighbors as seen in Fig.3.6. The structure is certainly built up this way, and it resembles that of common high tech semiconductors such as the III-V(e.g. GaAs) and II-VI(e.g. ZnS) or Si. When compared to the semiconductor GaSb where

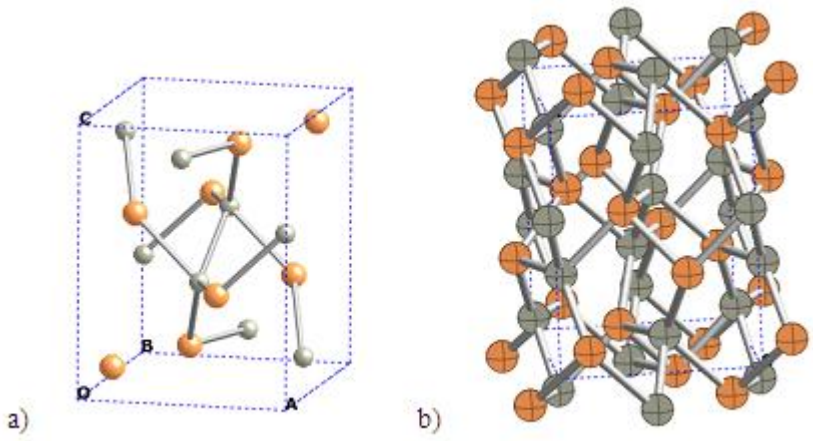

Figure 3.5: The crystal structure of ZnSb rendered by the program **CrystalMaker** from the data given by Almin[2]. a) Shows the unit cell which has 16 atoms. Sb atoms are orange/golden and Zn atoms are Grey. The unit vectors are the line segments OA. OB and OC. b) Shows an expanded cell. The stick is drawn between nearest neighbor atoms. The tetrahedral (distorted) units around each atom is clearly revealed.

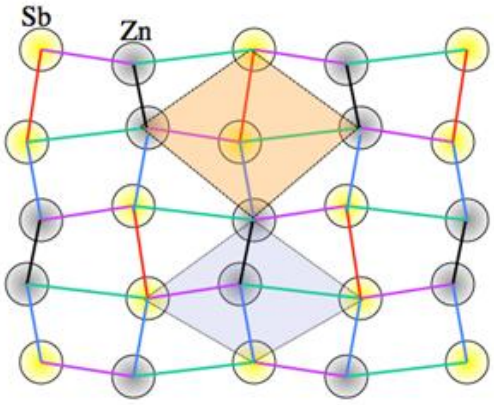

Figure 3.6: Schematic view of the ZnSb to visualize the interatomic distances. The distorted Zink Blende lattice is mapped into two dimension with the number of nearest neighbors preserved and the relative nearest neighbor distances visualized. Each atom is surrounded by four nearest neighbors; one of the same kind and three of the different kind. Distances with the same length have been given the same color. There are five different nearest neighbor distances in the structure : Sb-Sb: 0.281 nm, Zn-Zn: 0.258 nm, Zn-Sb: 0.266nm, 0.269nm and 0.274nm.

there is no change in electro-negativity between the atoms, while a small difference (0.1eV) is introduced by substituting Ga by Zn. However a difference in the total number of valence electrons pr. atom exists. In a glimpse of desire to put the systematics into a simplifying order, one can tentatively apply this systematics of the structure to bonding and features of the band diagram. Consider then that the density of states of ZnSb was similar to that of a covalently bonded semiconductor, then in a rigid band simplification one would just fill up the states with electrons. For the compound ZnSb, a II-V compound, there are clearly too few valence electrons to fill up the valence band completely; The Fermi level would then be in the top part of the valence band as shown in Fig. 3.7.

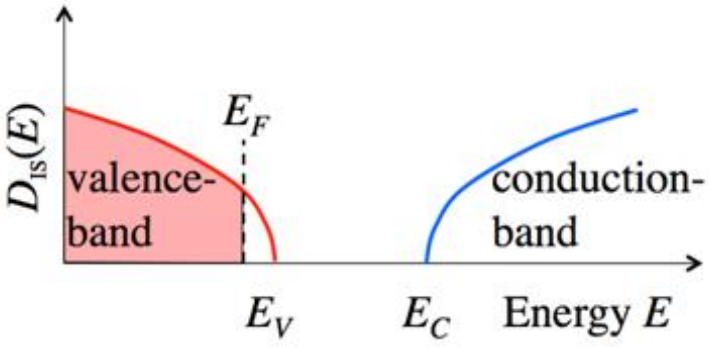

Figure 3.7: Schematic view of density of states of a semiconductor with the Fermi level in the valence band

The material would behave as a degenerate doped p-type semiconductor. ZnSb is normally a p-type semiconductor, and a high doping is desirable from a thermo-electric application point of view in order to optimize the power factor $\alpha^2\sigma$ or ZT. This simple point of view would lead to a hole density of half the atomic density i.e $2 \times 10^{22}\text{cm}^{-3}$. However, as presented in Fig.3.7, the hole concentrations observed in pure single crystal ZnSb are much lower than this which would be more in line with a description of a semiconductor with a fully occupied valence band (in the undoped state).

The other way of considering the building blocks of ZnSb is stemmed from Mikhaylushkin et al.[11] [19] where it is considered to be Zn_2Sb_2 arranged as illustrated in Fig.3.8. It should be emphasized that the structure is identical to that of Fig. 3.5.

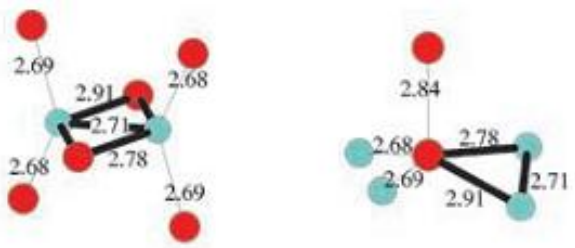

(a)

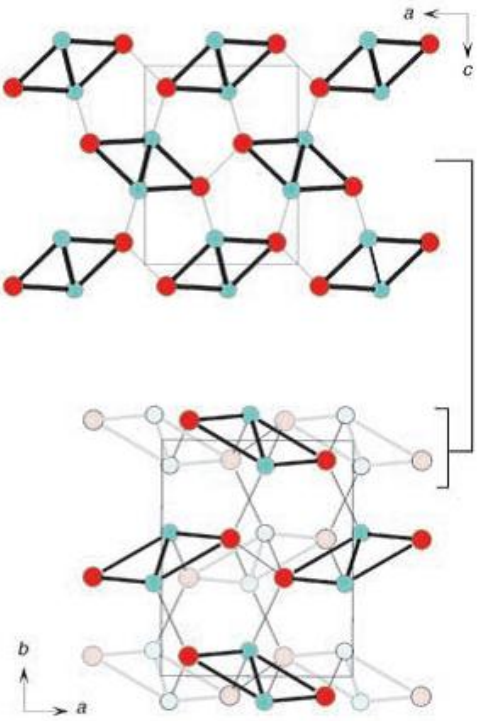

(b)

Figure 3.8: Crystal structure of orthorhombic ZnSb. Zn(green dot) and Sb(red dot) atoms, respectively. The rhomboid (diamond) ring Zn_2Sb_2 is used as central structural building unit and emphasized by bold lines, the remaining nearest neighbors contacts are drawn as thin lines. (a) Coordination environment for Zn(right) and Sb(left). The inserted numbers indicate interatomic distances in $\mathring{A}$. (b)Upper: a layer of diamonds in the ac plane; bottom: two layers of diamonds along the c direction related by glide operation. The layers are distinguished by dark and pale color. (From Mikhaylushkin et al.[11] [19])

Hausserman et al.[11] classifies the ZnSb compound with the term electron poor framework semiconductor(EPFS) where all the atoms participate in bonding, which is *sp*-orbitals, but where there are fewer than four electrons per atom. It is an idealization and they discuss how ZnSb (and Zn_3Sb_4) fits to the ideal. They also apply a different structural analysis of the same structure. First of all the first coordination sphere is increased, yielding a peculiar five-fold coordination with 4 atoms of unlike type and 1 of like type. (In a tetrahedral framework semiconductor there is four-fold coordination.) This adaption of one more atom in the first coordination sphere seems reasonable as the additionally included Zn-Sb bond of 0.294 nm is only slightly larger than the Sb-Sb bond(0.282 nm) while sufficiently smaller than the next bond distance (0.384 nm)belonging to the 2nd coordination shell of next nearest neighbors.

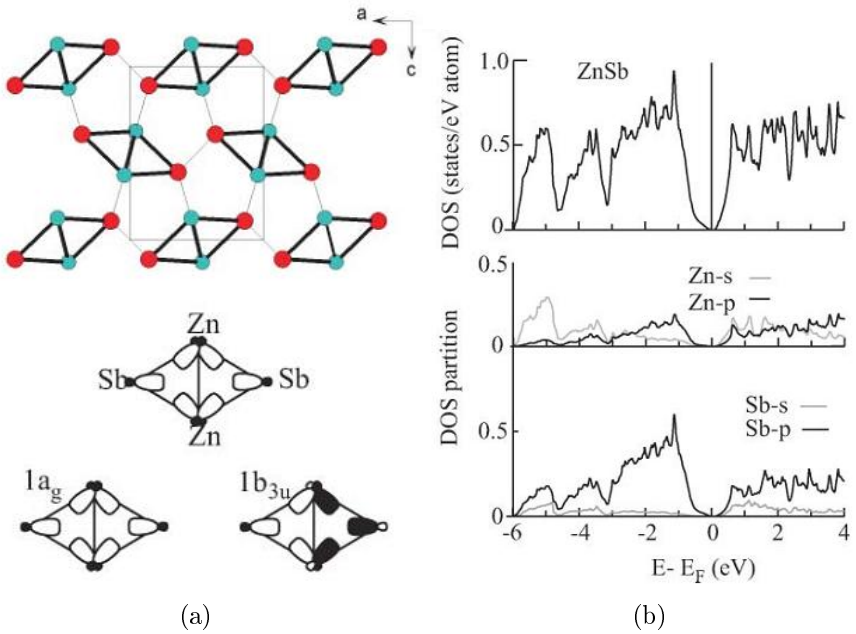

(a) (b)

Figure 3.9: Band calculations on ZnSb by Hausserman. (a) A layer of connected rhomboid rings (red is Sb, cyan is Zn), also the orbital basis set and two bonding orbitals; (b) gives the density of states vs. energy; the total is shown on top and the contribution from Zn and Sb *s* and *p* orbitals are shown at the bottom.[11]

The resulting structure can also be considered to be made up of Zn_2Sb_2 planar rhomboid rings as Fig.3.8 shows. The units are also chained together in rings whose projection forms pentagons in the [010] viewing direction also seen from Fig. 3.8. The arrangement of bonds and triangles(from the rhomboid ring) around each atom is described to occur in a tetrahedral fashion. "Thus, although higher coor-

dination numbers than four are realized, coordination is ruled by an underlying tetrahedral principle". By applying knowledge about the typical bonding for a rhomboid ring and counting the bonds to other rings it is rationalized that the structure should yield an electron precise situation and all valence electrons contributes to the bonding. In such a situation it is expected the Fermi level to be above the valence band in the band gap.

The result of electron structure calculations of Hausserman are shown in Fig 3.9[11], where it is seen that the Fermi level is just above the valance band and also that the contribution from the Zn p-electrons to the DOS are significant justifying the classifications of ZnSb as an EPFS.

3.4 Electrical properties of Zinc Antimony

3.4.1 Bandgap

The measurement of absorption edge of ZnSb has been reported by Turner, Firschler and Reese for unpolarized radiation, based on the p-type samples with rather high carrier concentrations $\sim 4 \times 10^{18}\text{cm}^{-3}$. The energy gap at room temperature was estimated to be approximately 0.52eV.[7]

Hausserman et al. give reference to reports of ZnSb as having an indirect band gap of 0.5 eV[11]. Zhang et al.[39] reports temperature dependent resistivity measurements yielding a band gap of 0.35eV. They point out that this is lower than what has been reported before by Shaver and Blair[29] on single crystal ZnSb, 0.56eV but comparable to what have been observed in doped material. Zhang et al.[39] attribute doping to excess Sb. Heavy doping can influence the band gap as was described in section 2.4. The doping effect of excess Sb is unclear. It could yield Zn vacancies or Sb interstitials.

3.4.2 Electrical property observations from literatures

It is interesting to compare the values of electrical resistivity, carrier concentration, and Seebeck coefficient which people have observed at room temperature. As a reference point, for an idealized semiconductor one would expect the Fermi level to be in the middle of the band gap, and the variations in carrier concentration would come about by changing the Fermi level position with variations in defect levels. One could therefore expect a large variation in resistivity values. The fact that ZnSb is orthorhombic as described in section 3.3 will make the transport properties of single crystals anisotropic and those of polycrystalline material an average over various crystal directions and also possibly subject to effects described in section 2.5. Table 3.1 summarizes several reports of resistivity on undoped ZnSb at room temperature.

One can see from Table 3.1 is that carrier concentrations at RT varies relatively little for undoped material. This can be interpreted as that the different cases have similar impurity concentrations and defect density. It could also be that ZnSb does not behave as a simple idealized semiconductor.

3.4.3 Doping effect

Undoped, pure, single crystal ZnSb is always found to be a p-type conductor. ZnSb can be doped, generally changing the bandgap with heavy doping. In the sense mentioned in the section 2.2, doping mans that the carrier concentration can be controlled by adding small amounts of foreign atoms. The phase diagram is generally not known for ZnSb with these additional atoms and the solid solubility is not known. The exact reason for the change in the conductivity is not known in all cases, but for many of the cases one cane make educated guesses from the systematics. Kostur and Psarev[17] reported that Ag, Au, Sn and Pb act as donors; one can speculate that this is due to Ag_{Zn}, Au_{Zn}, Sn_{Sb} and Pb_{Sb} substitutional positions. Further In and Te is reported to increase the hole concentration, increase the conductivity and decrease the Seebeck coefficient at relatively high concentrations. and some formation of InSb and ZnTe was reported. The element Ga is reported to act as a donor and one can guess by substituting Zn forming

Table 3.1: Summaries of properties from literatures

ρ $\Omega\cdot$ cm	p cm^{-3}	μ $cm^2/V\cdot s$	α	κ W/mK	ZT	Form	ref.
	4×10^{18}	10 (RT)	110 (RT)	1.1		single crystal	[14]
				1.14	0.6∼0.8 (573K)	poly-grind	[23]
0.4 (470K)			42 (370K)			thin-film	[8]
			820 (300K)			single crystal	[1]
	6×10^{16}		650 (300K)			single crystal	[1]
1.1×10^{-2}	6.3×10^{18}	94	196	2.3		single	[39]
0.2×10^{-2}	5.8×10^{16}	560	565			Stoich.	[17]
	$3 \times 10^{16}(p)$	850	400	30∼ 33		single crystal	[29]
0.7		170∼ 500	500 (300K)			single crystal	[15]
			740 (300K)			amorph. $Zn_{41}Sb_{59}$	[35]
1.2×10^{-3}			55 (RT)	1	0.15(RT) 0.45(650K)	Zn_4Sb_3 spark	[38]
2.5×10^{-2}			310 (RT)	1.3	0.16(RT) 0.65(650K)	Zn_4Sb_3spark +5%Cu_2Sb	[38]

Ga_{Zn}. Hole concentrations up to 1×10^{18}cm^{-3} has been reported for Ag doping and carrier concentrations up to 10^{19}cm^{-3} has been reported for Te additions. The case of Te additions have been studied by several groups. Ueda et al.[33] summarizes the efforts when presenting their own work; at low concentration(<1 at%) and high concentrations(>3 at%) the samples are n-type while around a small range around 2at% Te are n-type, possibly by forming substitutional Te atoms on Sb sites: Te_{Sb}. Excess doping with Te results in precipitation of the ZnTe phase and a change in conduction from n- to p-type.

Addition of Cd to ZnSb has be studied. One can expect that CdSb which has the same crystal structure as ZnSb[2] is soluble in all proportions. Additions of Cd is here not considered as doping in the sense introduced in section 2.2, but as the formation of solutions of the type $Zn_{1-x}Cd_xSb$. The band gap is expected to be between that of CdSb and that of ZnSb. The addition of Mn and Cr respectively to ZnSb will be explored in this thesis. The electrical effect of this addition is a priori unknown.

3.4.4 Effective mass

Martin et al.[18] measured on single crystals of ZnSb (with p=4×10^{14}cm^{-3} at 4K)and determined the effective mass of holes in the three different crystallographic direct. The measurements were done by two different methods called magneto-transmission where the hole cyclotron resonance is determined, The other technique was deducing the cyclotron effective masses from the Shubnikov-de Haas oscillations on a doped sample p=3×10^{17}cm^{-3} at 4K). The measurement by the different methods appears to agree well within experimental uncertainties. The cyclotron resonance effective masses along the crystallographic directions as 0.26×10^{-3}, 0.17×10^{-3}, 0.36×10^{-3} along the a-,b-, and c-direction respectively. All values are relative to the free electron mass. These appears too low to use for the density of states effective mass. Osipov and Aulas [1] report a density of state effective mass for the valence band of 0.8, and the components of the mass tensor along the three main directions having values of 1, 1.1 and 0.53. Those were determined by Seebeck measurements on single crystals.

3.4.5 Thermoelectrical properties

In 1965 it was stated by Shaver and Blair [29] that ZnSb has long been of interest as the p-type leg of thermoelectric couples used for power generation. Many of the then previous investigations into ZnSb have been empirical optimization of performance of polycrystalline specimens [ref 1 and 2 in [29]] ZnSb-CdSb alloy systems have also been investigated in this context.[ref 3 in [29]]. Shaver and Blair [21]summarizes work until 1965 by stating the power factor $\alpha^2\sigma$ of single crystal ZnSb is substantially larger than that of polycrystalline material. For n-type ZnSb made by Te doping the maximum power factor for 2.06 at% Te is reported to be $0.84 \times 10^{-3}\mathrm{Wm}^{-1}\mathrm{K}^{-2}$ at 573 K [33].

3.5 A note on some properties of Zn_4Sb_3

The purpose of this thesis is the study of ZnSb, thus the description of Zn_4Sb_3 is much less detailed. However it is possible to include Zn_4Sb_3 into the material while synthesizing ZnSb. Something will be included since the similarities with ZnSb.

As a good candidate of thermoelectric material, Zn_4Sb_3 has certain promising properties. Recently Zn_4Sb_3 has been far more studied than ZnSb. A higher interest can be understood by the lower thermal conductivity observed without any intentional nanostructuring. The low thermal conductivity may still not be well understood but the currently most favored explanation seems to be that it is associated with glass-like Zn interstitial sites in the structure Zn_4Sb_3[26][30]. In the thermoelectric context this means the interstitials are not ordered and they scatter phonons like an amorphous glass.

Zn_4Sb_3 has three modifications, α, β and γ phase. Particularly, β-Zn_4Sb_3 is outstanding due to it complex hexagonal crystal structure, whose space group is R3C. The structure of Zn_4Sb_3 is shown on Fig.3.10.[30]

The unique feature of β-Zn_4Sb_3 is that it combines a good electrical properties with

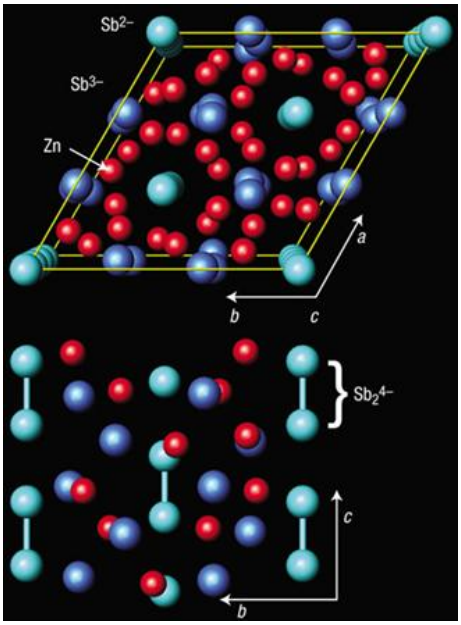

Figure 3.10: Structure of Zn_4Sb_3[30]

glass-like low thermal conductivity, which is a promising candidate for the power generator. The thermoelectric properties of β-Zn_4Sb_3 has been studied between 200°C ∼400°C by Caillat et al. And it was reported that β-Zn_4Sb_3 has a maximum ZT of 1.4 value at 400°C among other competitions.[32]

Chapter 4

Experimental methods

4.1 Motivation and organization of this chapter

The main job of this thesis is to characterize the electrical properties of ZnSb by various of the measurement, and verify the reliability of these measurements. This chapter consists of three parts. The first part describes the synthesis methods that have been used in this thesis. Tables listing the samples produced and used in this investigation are also given here. Different synthesis method will influence to the crystalline of materials, further the properties. After the primary melting and quenching, we used annealing and sintering to obtain the uniform phase. The next part describes the structural characterization techniques used in the thesis; Scanninig Electron Microscopy (SEM) and X-ray diffraction (XRD) has been helpful to determine the composition of the samples. The third part describes the electrical and theroelectrical measuring techniques used in the thesis. The main job is investigating the resistivity change with different conditions, for instance a changeable current input or temperature. Meanwhile, the carrier concentration and mobility is obtained by Hall measurement. And the thermal conductivity is calculated based on thermal diffusivity which is measured by laser flash method.

4.2 Synthesis of Zinc Antimony compounds

4.2.1 Methods of synthesis

There are different method for produce thermoelectric materials, since the melting points are quite different for different systems. From technological point of view, thermoelectric materials are categorized to three branches: low temperature with melting point 500-700°C; middle temperature with melting point 700-1000°C; and high temperature with melting point larger than 1350°C. The melting point is 546°C are showm in the phase diagram of Fig.3.1, reported by W.J.Turner et al.[36] Both in the synthesis and measurement process with high temperature, the melting is not expected to occur since it could induce a phase transition. Therefore, the temperature is a important factor which need to be monitored.

Even if powder metallurgy process is a good method, it still brings about some demerits, neither a controlled distribution of impurity nor any preferred orientation. Considering the melting point of both Zn and Sb, which are 420°C and 630°C, respectively, we used a common way to synthesis the samples, which is melting bulk Zn and Sb together with dopant elements (Cr or Mn) in a sealed quartz ampoules. However, since the melting point of Manganese and Chromium are high, they were grinded into powder, so thus diffusion into the grains well during melting and annealing will occur and mix in powder.

A SiO_2 glass tube with a diameter of 11mm was used. We firstly closed one end with a flame by oxygen and hydrogen torches. After putting the materials into the ampoule, it was vacuated and sealed off circumferentially at a position above the top of materials of approximately 30±2mm, thereby providing sufficient room. The SiO_2 glass tube is made of the non-thermal expansive materials so that it would not shrink while the surrounding being cooled. However, it is our experiences of synthesis that the Zn-Sn system has complications. It is fairly sensitive to the temperature variation during solidification. Hence, it was not surprising that the cracks were created during quenching procedure. The reason has been not clarified yet. But it is not inevitable to avoid this problem. A possible trick was employed in the materials synthesis of this thesis, that a thin film layer was coating on the inner wall of the SiO_2 tube so that an isolate layer formed between solid and

the inner wall. Acetone, of which chemical formula is $CO(CH_3)_2$, was applied for before putting the sample in. It produced a thin carbon film attached to the inner wall when it was heated and decomposed completely. The makable amelioration was observed even by microscope. The micro-cracks still exist, but much less than the one without coating. In addition, it was necessary to change the ampoule for the annealing, in order to prevent the carbon atoms to diffuse into the solid.

4.2.2 Raw materials and calculation of composition

The information on raw materials used for the synthesis in this thesis is following:

Antimony	INLOT 99.99% NTE-Basis
	ACEA·AESAR #0000030
	LOT : MM39539
Zinc	Shet 1∼3mm 99.99% 402583-1kg
	Batch number: 09502 EH
	EC231-175-3
	SIGMA-ALDRICH

The samples were melted in the SiO_2 glass ampoule with flame by oxygen and hydrogen torch and the predicted volume of the sample are shown on Fig.4.1. The volume was pre-calculated as $V = \pi r^2 \cdot h = \pi(0.55\text{cm})^2 \cdot 1.5\text{cm} = 1.4\text{cm}^3$.

There were two different batches of raw materials to be synthesized. The first batch was run through melting and annealing process; whilst the second batch was subjected to grinding and sinteirng after melting and annealing. The ingots were split into two parts, composing four groups of , in which included four compounds: $Zn_{46}Cr_4Sb$, $Zn_{49.5}Cr_{0.5}Sb$, $Zn_{46}Mn_4Sb$ and $Zn_{49.5}Mn_{0.5}Sb$. The requirements of shape for each group are:

- Group A: orthorhombic, used for AC and DC measurements;
- Group B: no geometrical requirements, samples are embedded in plastic for microscopy;

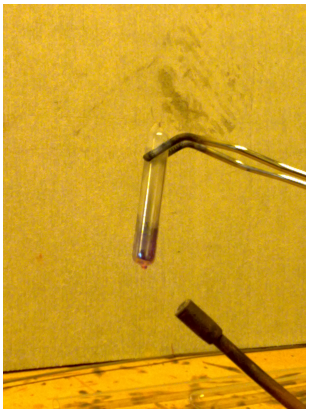

(a)

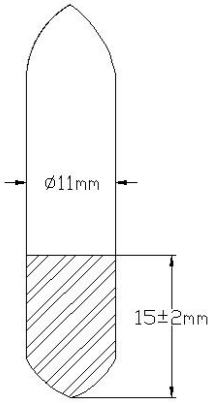

(b)

Figure 4.1: Synthesis: melting process and Schematic drawing of predicted volume. (a) the raw materials were sealed in a SiO_2 glass tube and melted by the hydrogen and oxygen torches. Melting temperature is around 900°C.

- Group C: orthorhombic, used for electrical properties measurements;
- Group D: disk, used for Hall measurements and Laser flash.

As an minutely illustration, the calculation of one of the batch, for group A and B is shown below. Approximately, the density of ZnSb is known as $\rho = 6.4\text{gcm}^{-2} \approx 6\text{gcm}^{-2}$ from the previous works. Thus the mass of ZnSb for the given volume is m_{ZnSb}=$V \cdot \rho$=8.5g; since $\mathcal{Z}_{\text{Zn}} : \mathcal{Z}_{\text{Sb}}$=65.38:121.78≈1:2, roughly the mass of antimony for the given volume is $m_{\text{Sb}} = \frac{2}{3}m_{\text{Zn}} = 5.699\text{g}$. The calculation of composition accords to

$$(\frac{mol}{at\%})_{\text{Sb}} = (\frac{mol}{at\%})_{\text{Zn}} = (\frac{mol}{at\%})_{\text{Cr/Mn}} \tag{4.1}$$

Therefore,

a) $Zn_{46}Cr_4Sb$
In practice, Antimony is weighted as as 6.2917g. Based on equation (4.1), the masses of Zinc and Chromium for $Zn_{46}Cr_4Sb$ with the given volume are

$$(\frac{6.2917/121.76}{50})_{\text{Sb}} = (\frac{m_{\text{Zn}}/65.38}{46})_{\text{Zn}} = (\frac{m_{\text{Cr}}/52.00}{4})_{\text{Cr}}$$
$$\Longrightarrow m_{\text{Zn}} = 3.1081\text{g}, \text{m}_{\text{Cr}} = 0.2149\text{g};$$

b)$Zn_{49.5}Cr_{0.5}Sb$
Antimony is weighted as as 6.0915g. Therefore,

$$(\frac{6.0915/121.76}{50})_{\mathrm{Sb}} = (\frac{m_{\mathrm{Zn}}/65.38}{49.5})_{\mathrm{Zn}} = (\frac{m_{\mathrm{Cr}}/52.00}{0.5})_{\mathrm{Cr}}$$
$$\Longrightarrow m_{\mathrm{Zn}} = 3.2382\mathrm{g}, \mathrm{m_{Cr}} = 0.0260\mathrm{g};$$

c) $Zn_{46}Mn_4Sb$
Antimony is weighted as as 6.1339g. Therefore,

$$(\frac{6.1339/121.76}{50})_{\mathrm{Sb}} = (\frac{m_{\mathrm{Zn}}/65.38}{46})_{\mathrm{Zn}} = (\frac{m_{\mathrm{Mn}}/54.94}{4})_{\mathrm{Mn}}$$
$$\Longrightarrow m_{\mathrm{Zn}} = 3.0302\mathrm{g}, \mathrm{m_{Mn}} = 0.2214\mathrm{g};$$

d) $Zn_{49.5}Mn_{0.5}Sb$
Antimony is weighted as as 6.1300g. Therefore,

$$(\frac{6.1300/121.76}{50})_{\mathrm{Sb}} = (\frac{m_{\mathrm{Zn}}/65.38}{49.5})_{\mathrm{Zn}} = (\frac{m_{\mathrm{Mn}}/54.94}{0.5})_{\mathrm{Mn}}$$
$$\Longrightarrow m_{\mathrm{Zn}} = 3.2586\mathrm{g}, \mathrm{m_{Mn}} = 0.0277\mathrm{g};$$

These ingots, stoichiometric calculated above, were separated into two parts Group A and B, one for electrical measurement and another for microscopy observations. Group C and D were made from the same ingots which synthesized by sintering, the details of calculation will not be listed here. Using the same method to compose the materials, Table 4.1 enumerates the composition of ingots.

4.2.3 Quenching and Annealing

After melting, the samples were rapidly immersed in cold water for quenching.This process influences the crystalline markedly. A rapid cooling yields the small crystalline; whilst a slow cooling promotes larges crystallites, or even a single crystal. For the purpose of an uniform phase, we preferred to a rapid cooling process. Considering the following process is annealing, the grain boundaries will be deformed and atoms will diffuse between grains. If the crystal has a larger grain size, certain

Table 4.1: Weights of samples for synthesis (g)

compound	Zn	Sb	Mn	Cr
Ingots for Group A and B				
$Zn_{46}Cr_4Sb$	3.1083	6.2917	–	0.2149
$Zn_{49.5}Cr_{0.5}Sb$	3.2375	6.0915	–	0.0260
$Zn_{46}Mn_4Sb$	3.0302	6.1339	0.2211	–
$Zn_{49.5}Mn_{0.5}Sb$	3.3779	6.1300	0.0294	
Ingots for Group C and D				
$Zn_{46}Cr_4Sb$	2.9794	6.0281	–	0.2063
$Zn_{49.5}Cr_{0.5}Sb$	3.2813	6.1732	–	0.0269
$Zn_{46}Mn_4Sb$	3.0591	6.1952	0.2235	–
$Zn_{49.5}Mn_{0.5}Sb$	3.2667	6.1425	0.0283	

atoms in the nucleation will be "ignored" or "tied up" by the circumambient atoms. Therefore, a smaller grain size shorten the diffusion length of atoms, being much easier to get a uniform phase.

Annealing was run after quenching. It provides a good opportunity to diffuse atoms. The furnace maintained the temperature at 400°C for more than 48 hour, providing energy to break bonds between atoms. The structure of Zn_4Sb_3 would be deformed. Zinc atoms move out of the grains. Defects, for instance dislocations are removed during the movement of atoms. Afterwards a certain new grains start to nucleate to substitute those deformed grains afterwards i.e. new ZnSb nucleus begin to grow in this case. When the new ZnSb phase grows uniform, the grain growth occurs in order to form larger crystal. The dopants diffuse into solid, substituting certain Zinc positions. The longer the time in annealing, the more uniform the phase we can get.

4.2.4 Sintering

As a alternating method to synthesis materials, sintering reduces the micro-cracks in solid, improving the homogeneity and purity of materials. Before sintering,

Figure 4.2: Synthesis: sintering instrument. 1- dimension detector; 2- lid; 3- programming; 4- supply current; 5- pressure gauge; 6- thermometer; 7- thermocouple; 8- furnace; 9- cooling water; 10- forcing press, 11- oil pump.

the samples were annealing in the furnace for 4 days which held temperature at 400°C. Afterwards, samples were first crashed and grinded in glove-box with argon environment, then been sealed by alumina film in order to avoid oxidation. After that, they experienced 0.8kp/cm^2 pressure to condensate.

The components of instrument for sintering are shown in Fig.4.2. It includes four parts: press(oil pump, pressure gauge and forcing press), heat(supply current, furnace, thermocouple and thermometer), programming and supplementaries(dimension detector, vacuum, cooling water, etc.). The pressure needs to be increase slowly from 1kp/cm^2 to 3.5kp/cm^2. The furnace is heated up by supply current and temperature is measured by thermocouple and thermometer. The vacuum pump is behind the instrument to vacuate the furnace. And we can can monitor the dimension by dimension detector during the plastic deformation.

The programming sets the process of sintering as 6 steps, which is shown on Fig.4.3. After the sample put in the furnace, it took 30 minutes to heat up to 2mV(260°C).

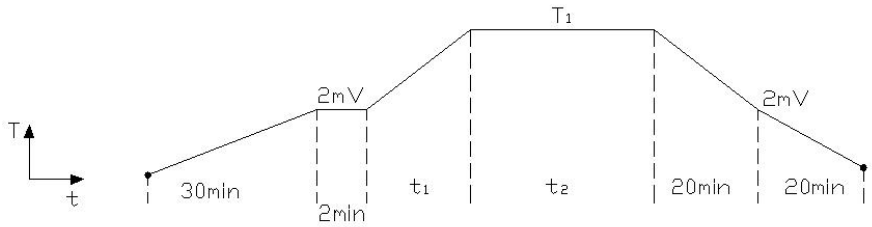

Figure 4.3: Synthesis: schematic drawing of sintering process. Temperature changes as time. Temperature measured by S thermocouple as unit of mV. T_1 and t_1 depends the time that the supplied current get 100A. t_2 depends the change of dimension of sample.

By this step, the atoms moved from surface into the solid and fill the porous. Then the pressure was increased slowly to generate condensation. Held the pressure and increased the current to about 100A continuously to heat the material up, the atoms diffused between lattice in this step. Atoms diffused into grain boundary by keeping the temperature and pressure. Afterwards, the material was in a high temperature and high pressure(3.5kp/cm^2) environments and plastic deformation carried on until there was no change for the volume of material. The following step was cooling down to 2mV and the pressure was decreased slowly. Finally, the pressure was kept 1 kp/cm^2 and current was removed slowly as well. The sintering temperature is listed in Table 4.2.

Table 4.2: Sintering temperature (°C)

$Zn_{46}Cr_4Sb$	$Zn_{49.5}Cr_{0.5}Sb$	$Zn_{46}Mn_4Sb$	$Zn_{49.5}Mn_{0.5}Sb$
459	447	445	428

4.2.5 Geometry and density

For the convenience of measurements, we expected to the samples have the geometry shown in Fig.4.4. The samples were cut with diamond cutter and grinded with the sandpaper progressively. The finest sandpaper is ×4000. Afterward the samples were polished by furs clothes in order to get the smooth surface.

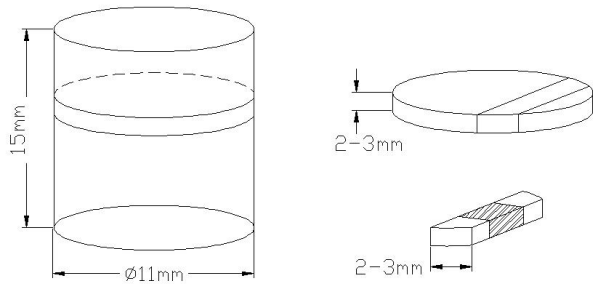

Figure 4.4: Synthesis: schematic drawing of expected geometry of sample split from ingot. Raw materials form a cylinder ingot, which would be cut to disk-shape first, then grind off the rest part to keep a bar-shape showed as the shadow.

Except for Group B, it is necessary to obtain the dimensions and density of samples so as the requirements of the measurements and calculations in the future. The

straightforward method to evaluate the density and mass is geometrical method. We can get the volume by conventional measurements. The density is derived by the ratio of mass and volume ρ=m/V. The results are listed in Table 4.3 and the samples are labeled identification, respectively.

Table 4.3: Summaries of sample geometry

Compound	ID	Height (mm)	Length (mm)	Width (mm)	Volume (mm^3)	Mass (mg)	Density ($g \cdot cm^{-3}$)
Group A							
$Zn_{46}Cr_4Sb$	#A1	1.286	2.768	1.635	5.820	34.1	5.859
$Zn_{46}Mn_4Sb$	#A3	1.370	3.515	1.903	9.164	53.9	5.882
$Zn_{49.5}Mn_{0.5}Sb$	#A4	1.910	3.667	1.695	11.872	69.9	5.888
Group B							
$Zn_{46}Cr_4Sb$	#B1	No geometrical requirments.					
$Zn_{46}Mn_4Sb$	#B3	Embeded in plastic for microscope and SEM.					
$Zn_{49.5}Mn_{0.5}Sb$	#B4						
Group C							
$Zn_{46}Cr_4Sb$	#C1	1.358	4.091	1.671	9.283	53.8	5.796
$Zn_{49.5}Cr_{0.5}Sb$	#C2	1.392	4.872	1.941	13.164	79.5	6.039
$Zn_{46}Mn_4Sb$	#C3	1.562	5.068	3.171	25.102	150.1	5.980
$Zn_{49.5}Mn_{0.5}Sb$	#C4	1.844	4.103	2.005	15.170	83.8	5.491
Group B							
$Zn_{46}Cr_4Sb$	#D1	Circle: ϕ12.7mm			148.720	932.5	6.270
$Zn_{49.5}Cr_{0.5}Sb$	#D2	Circle: ϕ12.7mm			273.785	1590.7	5.810
$Zn_{46}Mn_4Sb$	#D3	Square: a=8.058mm			112.198	702.8	6.2638
$Zn_{49.5}Mn_{0.5}Sb$	#D4	Square: a=8.000mm			127.044	763.3	6.0081
Comments: ϕ-diameter; a- length of edge.							

Another sophisticated approach is Archimedes, with which we can minimize the voids in the surface and the area near the surface. This method is base on buoyancy. When sample is buoyant in the liquid, the holes on the surface can be filled. The benefit is that we can get, even if not exactly, more precise value of the mass, turning out the density.

The first step was weight the sample in the air, denoting to m_{air} , which we have gotten in the geometrical method. In the next step, we used a lever dangled by

copper filament at both ends, one winded up the sample, and another was attached with the weight.

The value read on the weighter consists of sample, lever and copper filament, since the whole system was in balance, recording $m_{\text{balance}} = m_{\text{sample}} + m_{\text{rob}} + m_{\text{wire}}$. Finally, we immersed the sample into liquid, obtaining a mass in balance, recording m_{liquid}. The mass of liquid, which filled into the voids on the surface was figured out by $\Delta m = m_{\text{total}} - m_{\text{water}}$.

Since the density is proportional to the mass, the ratio of the density of liquid and sample equals to the ratio of the mass filled into the surface and the sample, i.e. $\frac{\rho_{\text{water}}}{\rho_{\text{sample}}} = \frac{\Delta m}{m_{\text{air}}} \Rightarrow \rho_{\text{sample}}$, we get the density of the sample. Fig.4.5 gives the sketch of Archimedes method.

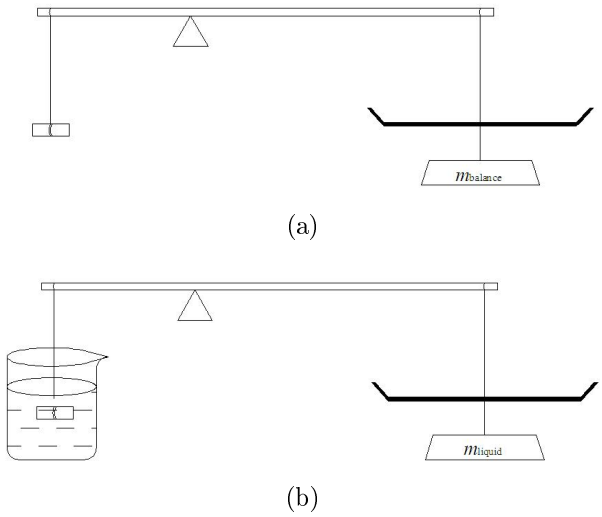

Figure 4.5: Synthesis: schematic drawing of Archimedes method. (a)Measure $m_{\text{balance}} = m_{\text{sample}} + m_{\text{rob}} + m_{\text{wire}}$; (b) m_{liquid}

It is worth to note that the capabilities to fill the voids are districted for different liquid. Some liquid with large surface tension would "ignore" these voids when they are as small as sufficient. Upon that, we used two liquids in practice, which were water and Methanol. Both of them do not react with samples.

Compared with Methanol, which has surface tension 22.70 $\text{mN} \cdot \text{m}^{-1}$ and density $0.7918\text{g} \cdot \text{cm}^{-3}$, water has relative large surface tension, which is 72.8 $\text{mN} \cdot \text{m}^{-1}$. It

turns out a small viscosity and small work of adhesion. In other words, water has large surface curvature and small wettability. That is to say, it is not as easy as Methanol to spread out on the surface of solid, i.e. Methanol fill the voids better. The experimental results of certain porou samples are summarized in Table 4.4. The experimental results showed a high surface tension of water, and the point is

Table 4.4: Density from Archimedes method with water and Methanol

Sample	ID	Water $(g \cdot cm^{-3})$	Methanol $(g \cdot cm^{-3})$
$Zn_{46}Cr_4Sb$	#A1	8.164	6.474
$Zn_{46}Mn_4Sb$	#A3	8.865	7.043
$Zn_{49.5}Mn_{0.5}Sb$	#A4	8.608	6.867

that there indeed are certain weenie voids in our samples, which probably would influence the further measurements. Besides, compared the results, we preferred to the density measured from Methanol, which are reasonable from theoretic views as well.

4.3 Characterization of materials

It is helpful to observe the samples by microscope before SEM and XRD. Stereo microscope and inverted compound microscope were mainly used in this thesis. Both of them use the reflected light, hence the ininformation of surface can be expressed. By the stereo microscope, which lights reflected by angles, the view of right eye is different with the left eye, hence the depth can be felt and get a stereo image of the surface. The cracks are observed by stereo microscope are more illustrative. By contrast, the view of the inverted compound microscope are same for both eyes, but with the reflected light perpendicular to the surface. The magnification is much larger($\times$1000) than the stereo microscope($\times$50). Therefore the grain boundaries and the area with different colors, which could mean the different phase (or maybe the same phase with various orientations using cross polarized light).

Scanning microscope was used for examine the microstructure of samples. When the electrons beam irradiates the surface of specimen, signals, for are yielded and

detected. The signals from surface are shown on Fig.4.6(a). Secondary electrons are induced by the extra nuclear electrons bombarded by incident electrons, which has the valid depth 5∼10nm. X-ray signal ascribes to the electromagnetic radiation with certain energies and waves, which are released during the energy level transition due to the inner electrons are excited. It is more widely applied for the deep area analysis.In this thesis, we mainly collected backscattering signal. Backscattered electrons stem from the partial of incoming electrons which are reflected by the nucleus and extra nuclear electrons. It is originated in elastic scattering, losing a few energy. Since the number of backscattered electrons is proportional to the atomic number, we used it to distinguish the component intuitively. The instrument we used is FEI Quanta200F. The composition of samples were analyzed by energy-dispersive X-ray spectroscopy(EDS). Fig.4.6 (b) and (c) shows the instruments and detector.

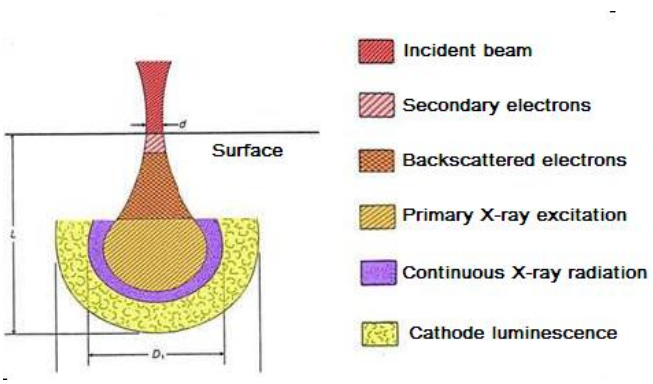

(a)

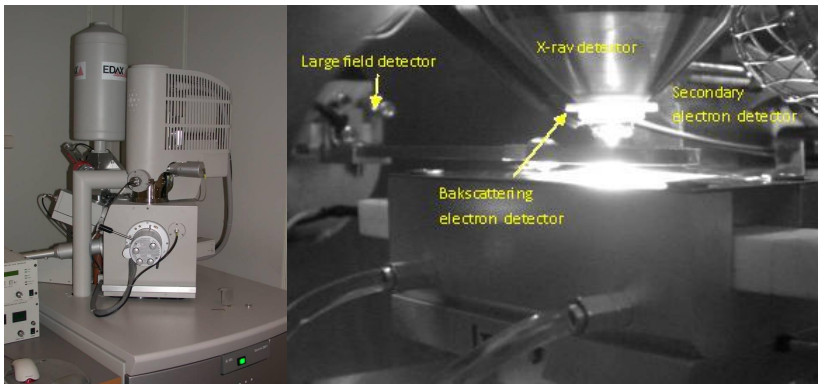

(b) (c)

Figure 4.6: Characterization: electrons yielded from surface and scanning electron microscope. (a) signal with different depth from surface; (b) the instrument used in this thesis; (c) detectors.[Figures are from the courseware of MENA3300,UiO]

While the EDS analysis gives us the composition of the different phases, the powder X-ray diffraction act as a "fingerprint" to identify the crystalline phases constitution. The position of diffraction peak is determined by the size and shape of the unit cell. The the intensity is given by the arrangement of the atoms, yielded from a particular plane (hkl)[4]

$$F_{hkl} = \sum f_n \cdot e^{[2\pi i(h\vec{u}_n + k\vec{v}_n + l\vec{w}_n)]} \tag{4.2}$$

The profile will be identified by the previous work. Alternatively, a standard XRD profile calculated by structure can be used. Fig.4.7 shows a XRD profile from **DIAMOND** program based on the structure calculation. The instrument used for the measurements in this thesis is Siemens D5000 with primary monochromator (CuKα_1). The calibration can be accomplished by the tabulated values or internal

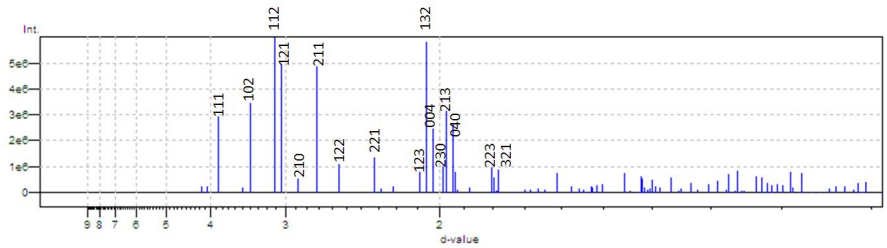

Figure 4.7: Characterization: XRD profile of ZnSb yielded from the program **DIAMOND** calculation. The peaks reflect the crystal planes responded to X-ray.

standard. Here, we induced silicon powder, which has distinguishable positions of the intensity peaks, mixed with sample powder to yield the XRD profile.

4.4 Electrical characterization

4.4.1 Contact resistance measurements

We start by explaining the reason for measuring the contact resistance and how it has been done in the thesis work. At the starting time of the thesis there was an activity of measuring the resistance of other thermoelectric material samples and

their temperature dependence. This was done by a standard four wire measuring technique; utilizing separate wire pairs for measuring the voltage and current. However the way the wires was arranged did not eliminate the influence of contact resistance to the sample. That arrangement is schematically shown in Fig. 4.8.

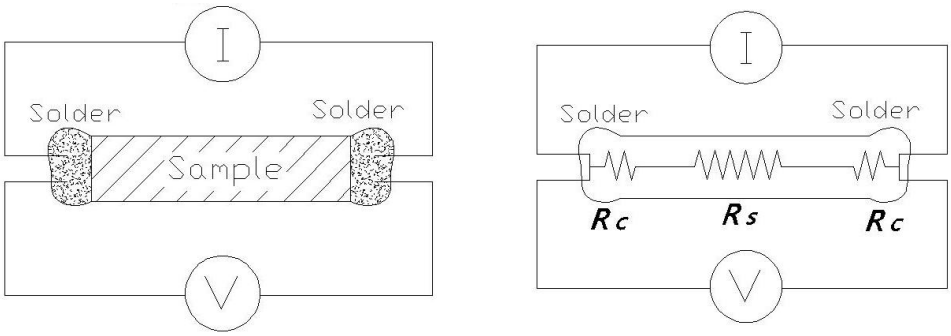

Figure 4.8: Electrical properties measurement: schematic drawing of connections which could be used for measuring resistance of a sample. (a) a bar shaped sample with solder 'blobs' at the end making contact to the sample. Wires are buried in the solder blob and connected to a current source I and the voltage measured by a voltmeter V; (b) the equivalent circuit diagram where R_s is the sample resistance and R_c represents the contact resistance.

The bar shaped sample of Fig.4.8 is soldered at the ends and wire leads are embedded in the solder for hooking up the current source, I, and voltmeter, V. In this configuration the contact resistance between the solder and the sample is not eliminated by the four wire measuring method. The current is passing through this contact and the equivalent circuit is shown to the right. In the general case the specific contact resistance of a metal semiconductor junction can be high. When current is flowing there will then be a voltage drop over the junction, equivalent to there being a voltage drop over the contact resistance R_c. Thus the measured voltage is not that over the sample alone and the true sample resistance is not measured by this configuration. The only contact resistance this hookup eliminates is that between the leads and the solder blob.

However there could still be practical reasons for using the hookup of Fig. 4.8 especially for temperature cycling measurements with limited possibility for using more elaborate contact hookups. But then the contact resistance should be measured

separate to indicate how large errors would be introduced. The measurement of contact resistance is also of interest in itself. For measuring the contact resistance we used a hook up and method schematically shown in Fig. 4.9.

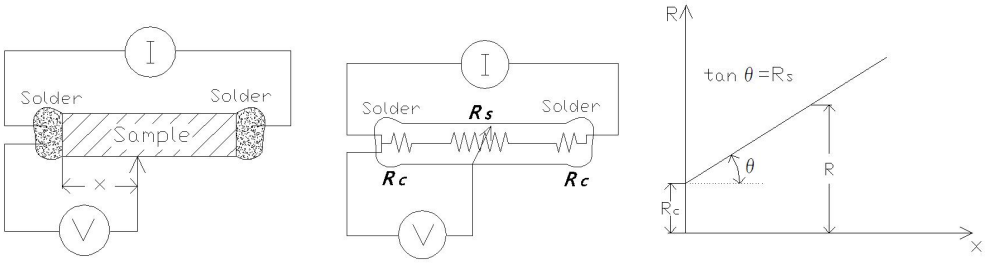

(a) (b) (c)

Figure 4.9: Electrical properties measurement: schematic drawing of method we used for measuring the contact resistance sample. (a) the bar shaped sample with solder 'blobs' at the end are as that of Fig.4.8 but the voltage is measured by a moveable needle probe contacting the surface of the sample. The distance between the probe and the end contact, x, is measured while the current and voltage is recorded. This is recorded at different positions along the surface, contact to the sample; (b) the equivalent circuit diagram where R_s is the sample resistance and R_c represents the contact resistance; (c) sketching the expected measured resistance R(x). The intercept of the curve through experimental point with the y-axis gives the contact resistance, while the sample resistance can be deduced from the slope $tan\theta = y/x$. Wires are buried in the solder blob and connected to a current source I and the voltage measured by a voltmeter V.

In the actual instrumentation AC current was used supplied by a signal generator at 42Hz. The current was varied by passing it through a variable decade resistor bank and the AC voltage across this resistor then gave the current, The voltage crossed the series resistor and the sample was measured by two Lock-In amplifiers.

A high precision micro-positioned probe was used as the variable position needle probe. The position of the probe was controlled by a screw. The feed distance of this screw was calibrated by scratching markings with the probe in a thin layer of carbon on a glass slide at regular turn intervals of the screw. The distance between the markings was then measured in another calibrated microscope. The feed was found to be 0.255mm (1/100inch) per turn. For the contact resistance

measurements we chose a spacing of 3 turns corresponding to 0.775mm between each measurement. A sketch is shown in Fig.4.10.

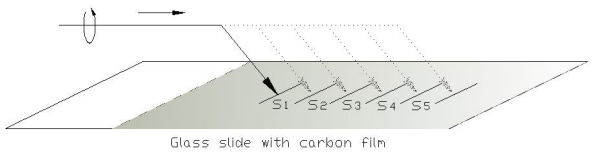

Figure 4.10: Electrical properties measurement: schematic drawing of the method obtaining progressive feed of probes. Thin carbon film is coating on the glassslide, with the progression, the fine probe marks each feed. i=5 feeds and 1 feed=$(s_1 + s_2 + s_3 + s_4 + s_5)/25$=0.255mm.

If the contact resistance should be very small, it would be difficult to measure with any precision with this method. Therefore it was decided to test out the method on a case where the contact resistance can be expected to be high. Contacting the ends of a bar directly could be expected to yield higher contact resistance than the soldered contact simply because the much smaller cross section the current flows through at the interface.

4.4.2 IV-measurements: DC and AC

Current-Voltage (IV) curves have been measured for the samples. The reasons for that are as follows. At the start of an electrical characterization task on an unknown material it is an invaluable test. It is invaluable among other reasons for ensuring that the contacts to the sample are ohmic. Since in general metals do not generally form ohmic contacts to semiconductors; sometimes they are rectifying Schottky barriers, sometimes unstable contacts, sometimes the current necessary for an electrical measurement may heat up the sample. This might be unwanted and can be observed by observing bending of IV curves. If the contact resistance is small IV curves give a good indication of the resistance and thus the resistivity of a semiconductor sample and can initially be used for comparing samples and observing trends pertaining to synthesis procedures. Here we have also used IV curves for eliminating unwanted offset voltages that can develop in a measurement because of effects involving thermal gradients and these combined with magnetic

fields and inhomogeneity and geometry imbalance of a sample. The implementation of the van der Pauw technique to be described in the next section 4.4.3 also measures the IV curves to determine resistances rather for these reasons. The measurements have been done with the sample in shielded metal box to prevent interferences and pick-up noise and in the dark to eliminate any light induced current.

For simple DC IV curves measurements we have mostly used a simple configuration as shown in Fig.4.8. The instrumentation consisted of a variable constant current source: *KELTHLEY* 6221 and a Voltmeter often used the *Stanford Research* SR830 in DC mode.

In general AC measurements can have some advantages to DC measurements. It allows to use a Lock-In technique to measure a response only at the frequency at which the sample is excited. This generally makes it possible to achieve a better signal to noise ration than achievable in DC measurements for the same power of excitation. That again permits one to use currents of lower power in AC measurements than in DC measurements for the same signal to noise ratio. In addition to less heating by possible by AC measurements, less thermal gradient develop, less effect of Peltier and Seebeck effect upon the measurements will arise. For AC measurements we have used a configuration like that shown in Fig4.11.

4.4.3 Van der Pauw Resistivity and Hall measurements

The resistivity was determined from the same measurements as described for measuring the contact resistance in section 4.4.1. The instruments are *KELTHLEY* 7001(channel controller), 2182A(voltmeter) and 6221(source current). In addition it was determined by four-point van der Pauw measurements.

Van der Pauw is a common method used measuring resistivity of semiconductors and the Hall voltage is often measured at the same time yielding the carrier-type (p or n), carrier mobility and carrier concentration. Fig.4.12 shows the contacts at the periphery of the sample. A photograph of the sample holder is shown to the right, while one of the many hookups of a current source and voltmeter is schematically

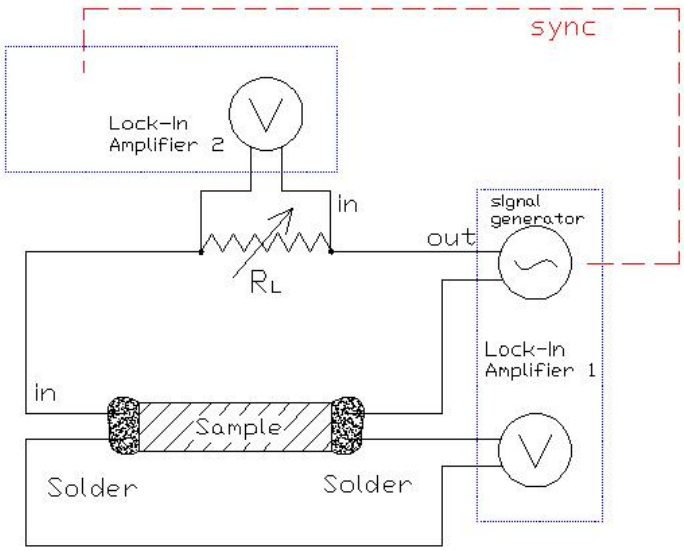

Figure 4.11: Electrical properties measurement: schematic diagram of the configuration of IV curves by AC measurements. The signal generator (built into the SR830 Locki-in amplifier) produced a sinus signal at 43 Hz. The current was varied by a variable serial resistor load resistor RL. The voltage across R_L was measured by a Lock-in amplifier (*Stanford Research* SR830)synced to the signal generator measuring the AC voltage of the same frequency as the generator. Similarly the voltage over the sample was measured by a lock in amplifier (SR830).

shown to the right. We will in the following describe the measurement technique.

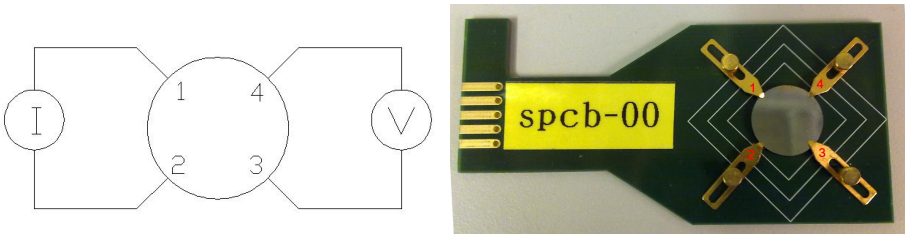

(a) (b)

Figure 4.12: Electrical properties measurement: Van der Pauw method. (a) schematic drawing of a sample with contacts at its periphery which are used for supplying current and measuring voltages. In the van der Pauw technique the voltage contact and current contacts are permuted and the direction of the current is changed; (b) one sample holder with a $Zn_{46}Cr_4Sb$ sample mounted.

Denoting I_{12} as the current input from contact 1 and output from 2, the voltage is measured between contact 3 and 4, denotingV_{34}, we get resistance R_{12-34}. Reversing the direction of current, we get R_{21-34}. Likewise the series measurements are run on

$$
\begin{aligned}
I_{32} - V_{41} &\Longrightarrow R_{32-41} \\
I_{23} - V_{41} &\Longrightarrow R_{23-41} \\
I_{34} - V_{12} &\Longrightarrow R_{34-12} \\
I_{43} - V_{12} &\Longrightarrow R_{43-12} \\
I_{41} - V_{23} &\Longrightarrow R_{41-23} \\
I_{14} - V_{23} &\Longrightarrow R_{14-23}
\end{aligned}
$$

The sheet resistance can be determined by two characteristic resistances R_A andR_B (resistance perpendicular to each other), where

$$R_A = \frac{1}{4}(R_{12-34} + R_{21-34} + R_{34-12} + R_{43-12}) \tag{4.3}$$

$$R_B = \frac{1}{4}(R_{32-41} + R_{23-41} + R_{14-23} + R_{41-23}) \tag{4.4}$$

According to van der Pauw equation[34]

$$exp(-\pi\frac{R_A}{R_{sheet}}) + exp(-\pi\frac{R_B}{R_{sheet}}) = 1 \tag{4.5}$$

where R_{sheet} is the sheet resistance. And this equation can be solved to find R_{sheet} the sheet resistivity, defined by$R_{sheet} = r/t$, where t is the thickness of the sample and ρ is the resistivity. The solution can be written as

$$R_{sheet} = \frac{\pi}{ln2}\frac{R_A + R_B}{2} f(\frac{R_A}{R_B}) \tag{4.6}$$

here f is a universal function of the ratio between R_A and R_B and has value going from 1 for R_A=R_B smoothly to lower values.

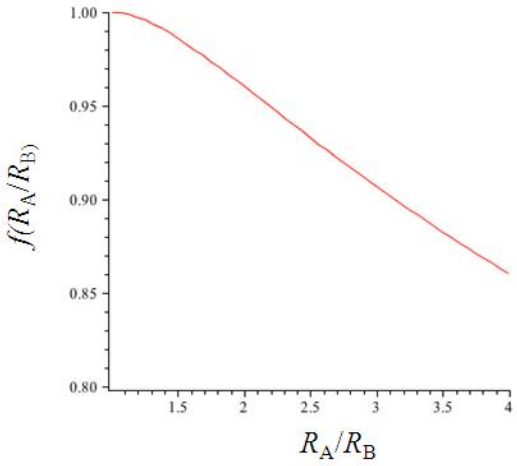

Figure 4.13: Electrical properties measurement: f-function for calculation of the sheet resistance with Van der Pauw method. When the ratio if R_A and R_B is closing to 1, f-function≈1. Simulated by **MatLab**.

The carrier type and carrier concentration and mobility were measured in the present of magnetic field. In the present of magnetic field, the current was input from contact 1 and output from contact 3, I_{13}, shown by Fig.1.14.

When a carrier is in a magnetic field, it experience both electromotive force and Lorentz force.

$$\vec{F} = q\vec{E} + q\vec{v} \times \vec{B} \tag{4.7}$$

An induced electrical field is created in y direction to balance the Lorentz force. This electrical field is given by

$$E_y = v_x B \tag{4.8}$$

Recalling equation (2.7), we have $v_x = j_x/qp$ in the case of p-type material. The induced electrical field can be direved by measureing the tranverse voltage across the sample, $E_y = V_y/w$, where V_y is the Hall voltage measured over point 4 and 2 when the current goes through point 1 and 3 in Fig.4.14, denoting V_{42} and I_{31}, respectively. And w is the width of the sample. Put them into equation (4.8), the carrier concentration can be solved by

$$\frac{E_y}{j_x B} = \frac{V_y/w}{(I/wt)B} = \frac{tV_y}{IB} = \frac{1}{qp} \tag{4.9}$$

where t is the thickness of the sample. And the mobility can be calculated by equation(2.8) $\sigma = qp\mu_p$.

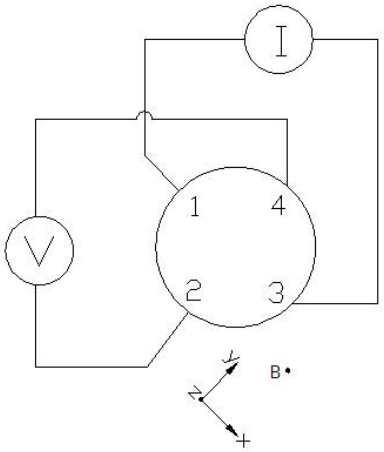

Figure 4.14: Electrical properties measurement: schematic drawing of Van der Pauw method measure carrier concentration and mobility.

Likewise, the Hall voltage $I_{31} - V_{42}$, $I_{24} - V_{13}$ and $I_{42} - V_{13}$. Since certain problems would be caused by the symmetry of sample and the placement of contacts, reserving the poles of magnets can solve it.

4.4.4 Cryogenic resistivity measurements

It is important in this thesis that investigate the resistivity change as a function of temperature in a low temperature range. A good way is using cryogenic resistivity measurements, which used the same configration as AC measurement except for

the sample experienced a temperature gradient. The sample is cooling down to 4K by liquid helium or 80K by liquid nitrogen, and being heated up back to room temperature. An AC current pass through the sample and the potential difference is measured at the ends of sample. The resistance is calculated and changes as a function of temperature. Conventionally, the sample is mounted in the sample

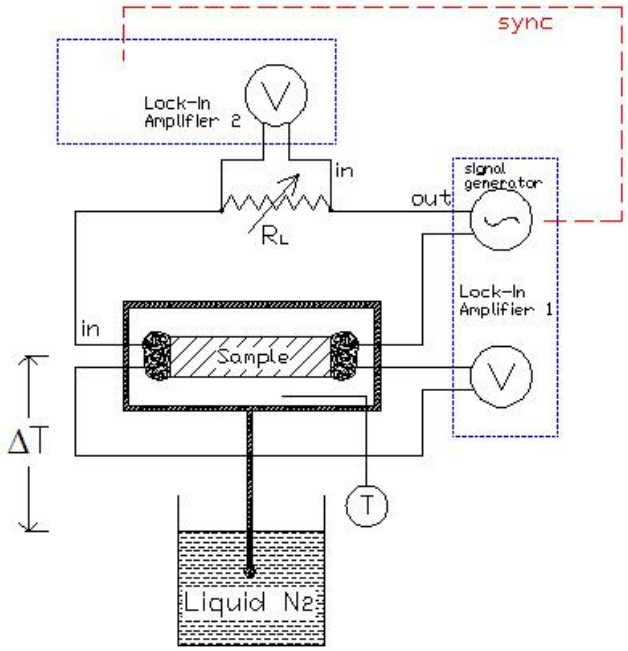

Figure 4.15: Electrical properties measurement: schematic drawing of cryogenic method. The measurement is similar with AC measurement, except for a temperature gradient is created. The sample is in a sealed chamber, which connected with amperemeter, voltmeter and thermometer. A rod is connected with the chamber and one end is immersed in liquid nitrogen, being 80°C. Chamber is heated by external heater.

chamber. A rod is connected with this chamber, another end is immersed into liquid nitrogen, creating a temperature gradient. A heater is applied on the sample chamber. The resistance is measured from 80K∼RT and continuous heating. However, the heater was not available during the work in this thesis. If we took the chamber out of the liquid nitrogen, warmed up spontaneously, the air condensation occurred, changing the entropy of the environment. The measurement became fluctuating time to time and and resistivity climbed fairly high which is untruly result. Principally, the sample would experience the exactly same in the process of both cooling down and heated up. Therefore, the measurements were carried on when the sample cooling down with liquid nitrogen. Yet, there was an-

other problem. The operation temperature range was shortened from RT∼120K. Fig.4.15 is the sketch of the circuit and setups.

4.4.5 Thermal conductivity: Laser flash measurements

Laser flash is a rapid and popular method to determine the thermal diffusivity and calculate the thermal conductivity in further. The thermal diffusivity can be determined by measure the heat difference of both sides of thin sample.

According to the conductance equation:[24]

$$\frac{\partial T}{\partial t} = \alpha(\frac{\partial^2 T}{\partial r^2} + \frac{1}{r}\frac{\partial T}{\partial r}) \tag{4.10}$$

the boundary conditions are defined as

$$\begin{cases} \frac{\partial T}{\partial r}\big|_{r=0} = 0 \\ \frac{\partial T}{\partial r}\big|_{r=R} = 0 \end{cases} \tag{4.11}$$

A detailed derivation and solution can be find in reference[24].

A disk sample is placed in the vacuum in order to satisfied the boundary conditions. And the thermocouple is mounted on the side of holder. The temperature increase with time. As long as the temperature is stable at the defined value, the laser beam is quickly pulsed to one side of the sample by several time, 3 in this case, which is called "shot". The shotted surface absorb the energy and transfer to the backside. Then the heat is emitted from the backside and radiate to the IR detector. The through-plane thermal diffusivity is determined if the density and specific heat are known. The density was measured and listed in section4.2.5. The specific heat was used 0.3J/k, which is determined by the past measurements with this particular instrument employed in this thesis, *NETESCH*® LFA 457 MicroFLASH^{TM} with Cape-Lahman pulse correction model. Illustration of the laser flash method is shown on Fig.4.16.

Furthermore, the thermal conductivity can be determined as

$$\kappa(T) = \alpha(T)\rho(T)C_P(T) \tag{4.12}$$

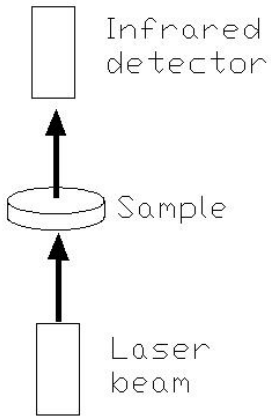

Figure 4.16: Electrical properties measurement: schematic drawing of laser flash measurement.

Here, ρ is the density of sample at room temperature, distinguished with the resistivity we used in the former text.

The samples for laser flash weresynthesized by sintering, which has been described in section4.2.4. Two sizes sample were prepared, circle with diameter 12.5mm and square with length side 8mm. The sample was coated by carbon in order to increase the energy absorbed on the laser side and detective signal on the backside. However, one of the sample, $Zn_{46}Mn_4Sb$ missed a corner. The reason is considered that during sintering the pressure is not released slowly enough, inducing brittleness in the sample. To avoid the laser passing through this corner, we used a piece of mica, which is a good isolator, to cover it, as shown on Fig.4.17. We will cover details about it in chapter 5. The sample holder has vary low thermal conductivity in order to guarantee the sample in a heat insulated environment. The temperature range was settled as RT to 300°C $\sim$ 350°C based on the melting point of the materials.

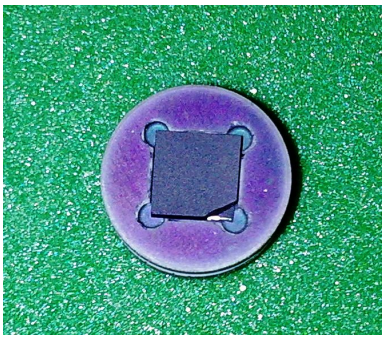

Figure 4.17: Electrical properties measurement: solution of laser flash measuring the imperfect geometry sample. $Zn_{46}Mn4Sb$ with a missing corner, covered by mica on the back side to block the laser penetrate.

Chapter 5

Result and discussion

In this chapter, the results with the measurements mentioned in last chapter will be systematically summarized. Most of the are listed and plotted. At the beginning, the results of synthesis are presented and we discuss the different result between annealing and sintering. It follows the analysis possible composition we expected to obtain from the synthesis in terms of crystallizing process. Based on these analysis, we summarized the results from characterization of samples, which includes microscope, SEM and XRD, to verify the composition of samples. Next, in the result of electrical measurement, the contact resistance is first to be given and the reliability of measurements will be discussed. Afterwards, we will come to the resistivity, carrier concentration and mobility. The temperature dependence of resistivity and thermal conductivity will be discussed.

5.1 Result of the synthesis process

The samples were melting in a SiO_2 glass tube which is made of the non-thermal expansive materials so that it would not shrink while the surrounding being cooled. However, the Zinc Antimony system is complicated as we mentioned in section 4.2.3. Hence, cracks occurred during the quenching procedure, shown in Fig.5.1.

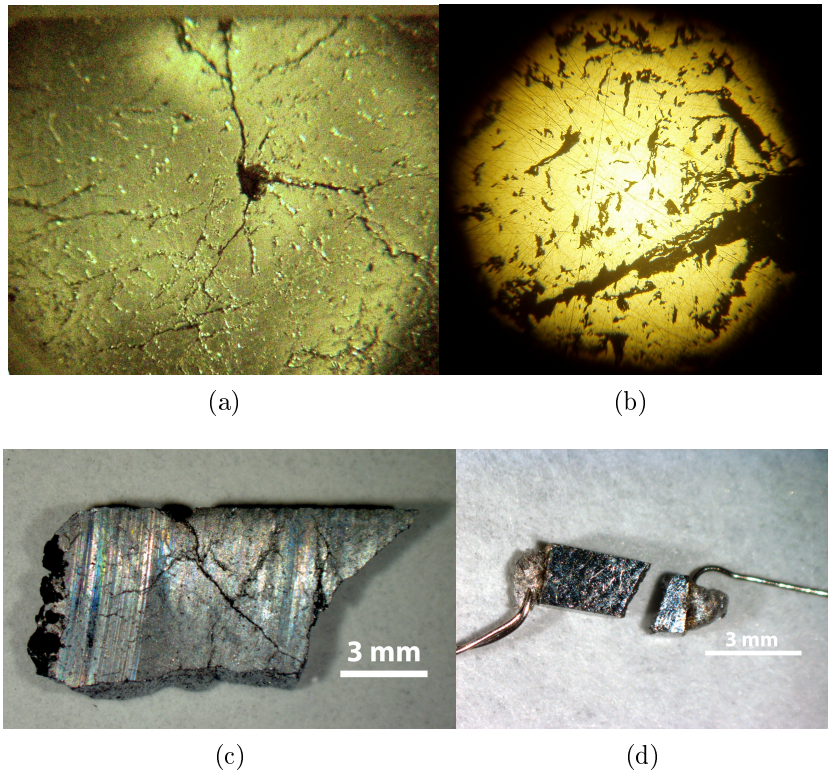

(a) (b)

(c) (d)

Figure 5.1: Experimental result: Damaged cracks of sample. (a) observation of $Zn_{49.5}Mn_{0.5}Sb$ by inverted compound microscope; (b) observation of $Zn_{49.5}Mn_{0.5}Sb$ by stereo microscope; (a) and (b) are the same position in the same ingot, synthesized by annealing. The cracks are along with anti-centripetal direction . (c) obvious cracks within $Zn_{46}Cr_4Sb$ which was cleaved from the ingot only been through melting and annealing. It was synthesized for the Group A and B; (d) the broken $Zn_{46}Mn_4Sb$ with solder. Sample ID: #A3

The top two (a) and (b) show the cracks of sample $Zn_{49.5}Mn_{0.5}Sb$ with inverted compound microscope and stereo microscope, respectively. It can be seen that the solids are forced in anti-centripetal direction since the contract from the wall of during quenching SiO_2 glass tube, leaving a void in the center. An undesirable outcome, shown in Fig.5.1(c), is that micro-cracks exist within the solids, which are not easy to be perceptible and detected from surface. It brought about that the probes were moving from time to time due to micro-force or expansions of the sample. As a consequence, the results of contact resistance measurement were variable, that it was difficult to find the resistance of material, reducing the reliability of measurements. An even worse damage is area defects due to a larger cracks, resulting in the sample separated into several pieces. Fig.5.1(d) is the consequence of those cracks, which led the samples to break.

When the ampoule with melted materials was rapidly cooling, the solid was "grasped"' by the inner wall of ampoule, resulted in an non-uniform force distributed within the solid. Consequently, the cracks occurred.The reason to cause the crack can be considered in terms of the grain size created by the synthesis method. Annealing can produce the larger grain size. Due to the different direction of crystal growth, two neighbouring grains align themselves in different directions. When the grain growth large, the larger force between boundaries is created as well due to the longer the length of grain edge. Even though the strain-stress between grain boundary is along with the arbitrary direction, when the strian-stress in a particular direction is large enough, dislocation forms, leading to the crack. the net strain-stress of the sample distributes non-equilibrium. As a result, These cracks could cause line defects, leading to severe influences to the motion of carriers. Although grinding and polishing improved the quality of surface, the micro-crack might exist both on the surface and within the solids.

By contrast, sintering can cause the small grain size due to the crashing and grinding process after annealing. Samples are formed by fine powder under high temperature and pressure. The expansions of small grains in multi-orientations bring about the strian-stress distributed in all direction. Consequently, the strain-stress in all direction can be balanced out, which is a good solution for the cracks, reducing the brittleness of material effectively.

5.2 Discussion of synthesis process

Before presenting measurement results and characterization pertaining to the morphology, and phase uniformity of the samples, we will present an analysis resulting in a prediction of the phases and their distribution in the samples based upon the construction of like ternary phase diagrams. All the samples synthesized in this thesis have experienced melting. They contain Zn and Sb and a third element Cr or Mn. We can try to in the following to describe the cooling in terms of the ternary phase diagrams, tentatively rationalized from the binary diagrams. In particular we want to predict how what are the compounds present if the system had been cooled down slowly enough to go through equilibrium situations and how much of each compound would we have. Then there are two approaches that can be taken, (i) or (ii) will be described below, yielding different calculations and then the phase diagram can be drawn and the amount of different compounds expected for equilibrium processes estimated. We will take the $Zn_{46}Mn_4Sb$ as an example.

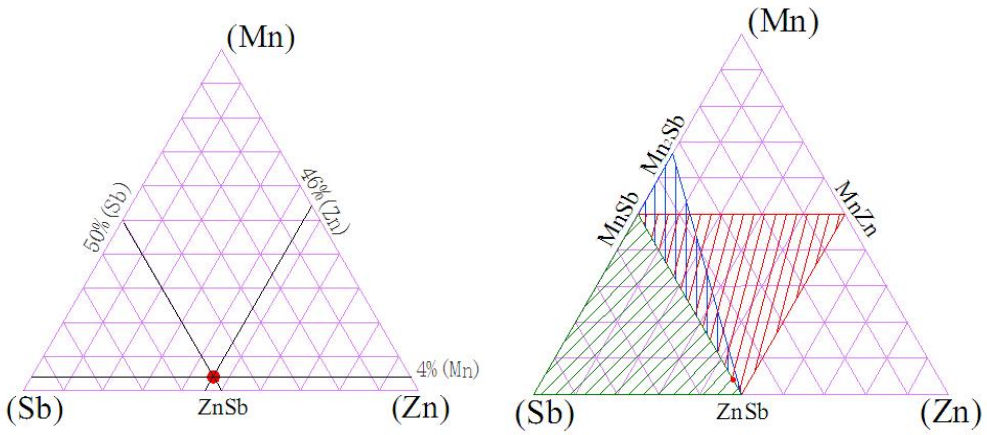

Figure 5.2: Discussion: ternary phase diagram of $Zn_{46}Mn_4Sb$. (a) ternary phase diagram of $Zn_{46}Mn_4Sb$, Sb-50%, Zn-46% and Mn-4% are supposed to cross on the point which represent the composition of solid; (b) the triangles where the cross point is sitting represent the possible compositions.

(i) Aimed at the whole system, it is the easiest way to build up a ternary diagram.

In Fig.5.2(a), the lines which represent to three elements: Sb-50%, Zn-46% and Mn-4%, are supposed to cross on one point, which is called ternary eutectic. This

point stands for the composition of the solid. This cross point sits within a triangle, of which the vertices are denoted the possible compositions, i.e. the final crystal consists of three of them. In this case, it is sitting on the sharing line of three triangles, shown in Fig.5.2(b). One is (Sb)-MnSb-ZnSb, the second one is MnSb-Mn_2Sb-ZnSb and the third one MnSb-MnZn-ZnSb, indicating three group of possible compositions.

(ii) The second process aims at the compositions individually.

If we have compound α, β and γ, and the final composition is sitting with in a triangle consists of these three, i.e. the final solid consists of phase α, β and γ.

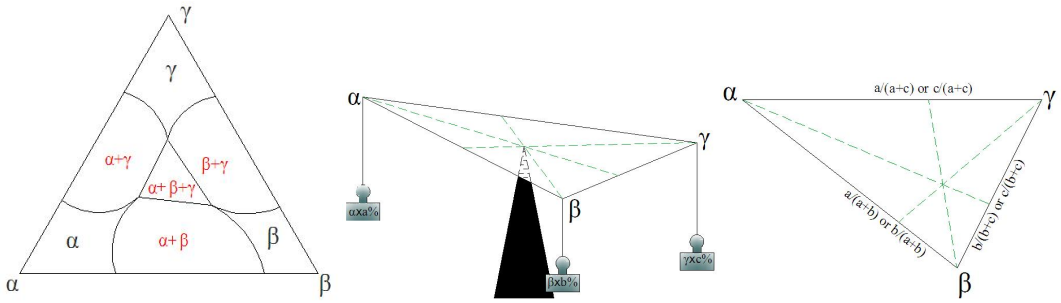

(a) (b) (c)

Figure 5.3: Discussion: schematic drawing of lever rule. (a) ternary diagram of α, β and γ; (b) the lever rule shows the portions of each composition; (c) we can get the point, standing for the portion of α or β at $\alpha - \beta$ binary system by either of a/(a+b) or b/(a+b). Likewise it applied for calculate the $\alpha - \gamma$ and $\beta - \gamma$ binary system.

If we know the percentage of each element, we can calculate each composition in binary system. Then the lines connected with the binary eutectic would cross together, giving us the final composition. This is can be accomplished based on the lever rule, shown in Fig5.3(b).

We still take the example of $Zn_{46}Mn_4Sb$, the cross point gives us the ternary eutectic, shown on Fig.5.4. Thus,

- Sb at Sb-Mn binary system $\frac{50}{50+4} \times 100 = 92.59$,

- Mn at Mn-Zn binary system $\frac{4}{4+46} \times 100 = 8$,
- Sb at Sb-Zn binary system $\frac{50}{50+46} \times 100 = 52.9$, which is not drew on the graph.

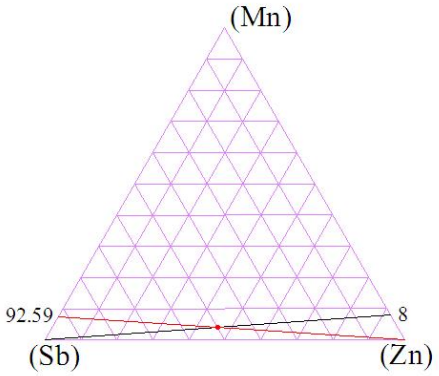

Figure 5.4: Discussion: lever rule to calculate the portion of elements in separated binary systems.Take $Zn_{46}Mn_4Sb$ as an example. The portion of Sb at Sb-Zn binary system, Mn at Mn-Zn binary system and Sb at Sb-Mn binary system are labeled on the graph.

We can apply this method reversely for the possible group to infer more precisely in advanced. In the triangle of (Sb)-ZnSb-MnSb, shown in Fig.5.5(a), the ternary eutectic is on the line of MnSb and ZnSb, indicating the zero percentage of Antimony in either (Sb)-MnZb or (Sb)-ZnSb.The same situation occur in both the triangle of MnSb-Mn_2Sb-ZnSb and MnSb-MnZn-ZnSb, shown in Fig.5.5(b) and (c): zero percentage of Mn_2Sb exist in either MnSb-Mn_2Sb or Mn_2Sb-ZnSb, and existence of MnZn is neither MnSb-MnZn nor ZnSb-MnZn.

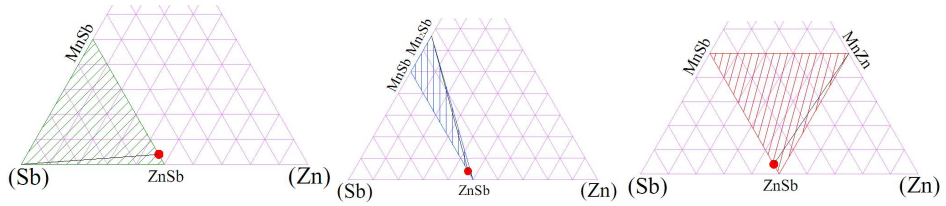

(a) (b) (c)

Figure 5.5: Discussion: an example of lever rule application for $Zn_{46}Mn_4Sb$. (a), (b) and (c) represent the possible composition group of solid. The red point sitting in the MnSb-ZnSb in each composition group, implying that there are no (Sb), MnZn and Mn_2Sb exist.

In sum, we predict that the crystal consists of two phases, which are ZnSb and MnSb by theoretic analysis. The advanced investigation will be carried on by chacacterization from Microscopy and X-ray diffraction.

5.3 Result of characterizations (Microscopy, SEM and XRD)

The observations from inverted compound microscope showed a obvious grain boundary. Fig.5.6 gives the image of samples as an example. The images are with the same scale bar and grain boundaries are clear visible. With partly crossed polarized light, the different orientation of crystal planes shows the different level of colors. The different synthesis methods can be compared by characterization. The middle two are from annealing and bottoms are from sintering. It is clear to show that with annealing, the grain size is larger than those with sintering. There is also a melting feature clearly to express by the image of microscope, particularly the dendritic shape in the (a)Zn_{46}Cr4Sb and bright stripes in the (b)$Zn_{46}Mn_4Sb$..

The bright areas observed by microscope are considered as Antinomy rich-phase based on the experience from the earlier course MENA3300, and it indicates which the dendritic areas are considered as the phase with dopant due to the smaller atom. It turns out if there is a Sb phase, some of the Mn must segregate out based on the lever rule which has been mentioned in last section. From the phase diagram, shown in Fig5.6(a) and (b), there are two possible second phase (in addition to ZnSb) exist in each case. Mn_2Sb ans MnSb in $Zn_{1-x}Mn_xSb$ and $CrSb_2$ and CrSb in $Zn_{1-x}Cr_xSb$.

The pure Antimony was found in all of samples by SEM. As shown in Fig5.7, Sb was detected by SEM with backscattered electrons, which is labeled "1" in (a), and EDS with strong signal in $Zn_{49.5}Mn_{0.5}Sb$ ($\#B4$) in (b). The intensity is 835.78, which is much high than Zn(11.12). Atomic percentage was defined as 95.99%. The 4.01% Zn is showed by small peak in the figure, which is considered by scattering from surroundings. In the observation of other samples of group B and D, atomic percentage is detected from 81∼95.99%, depending the positions.

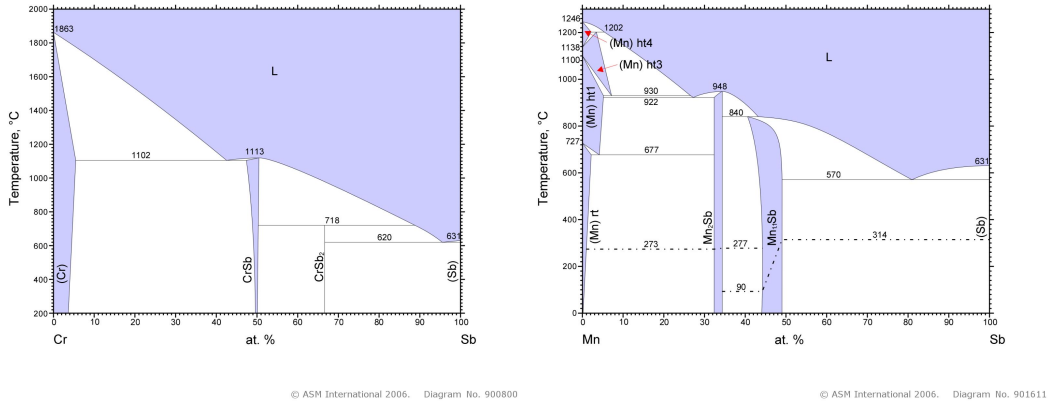

(a) (b)

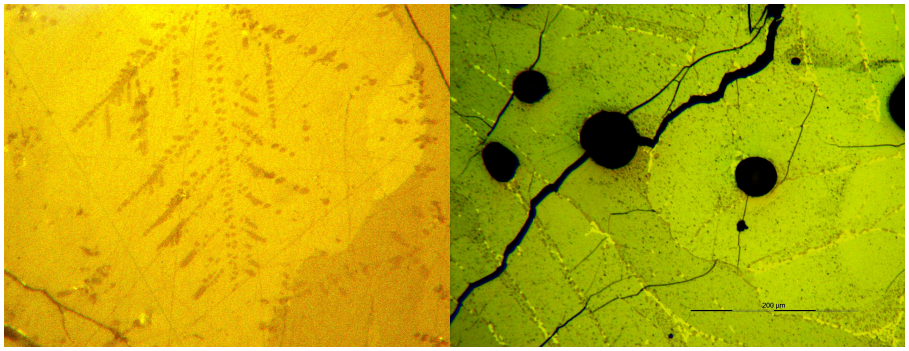

(c) (d)

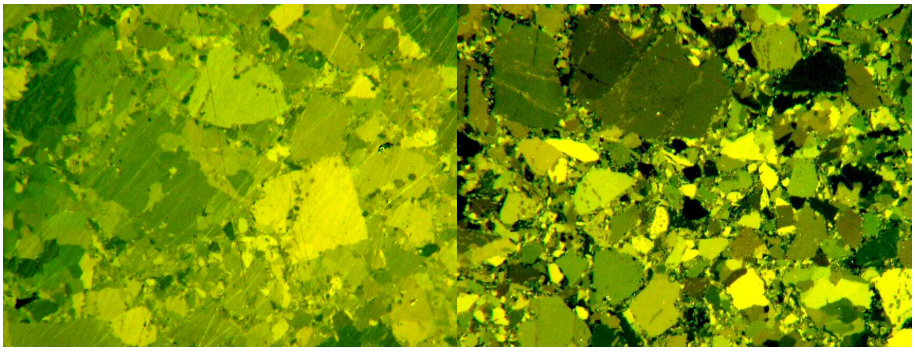

(e) (f)

Figure 5.6: Experimental result: observation of annealed and sintered sample of $Zn_{46}Cr_4Sb$ and $Zn_{46}Mn_4Sb$ by Microscope. The image are with same magnification. The scale bar is in (d), which is 200μm, is applied for all of the images in this figure. (a) phase diagram of Sb-Cr; (b) phase diagram of Sb-Mn; (c) $Zn_{46}Cr_4Sb$ from annealing, #$B1$; (d)$Zn_{46}Mn_4Sb$ from annealing, #$B3$; samples with larger grain size. (e) $Zn_{46}Cr_4Sb$ from sintering, #$D1$; (f)$Zn_{46}Mn_4Sb$ from sintering, #$D3$; samples have the fine small grain size.

The rests are considered scattering from surroundings. The main phase is detected as ZnSb , which is investigated at different position, are also labeled on Fig.5.7(a). The position of “2” and “4” are two different grain, and “3” is their boundary. The analysis by EDS shows the composition as 50.22%Sb, 49.78%Zn, 50.65%Sb, 49.35%Zn and 50.91%Sb, 49.09%Zn, respectively. The similar value of atomic percentage are also found at other samples as well.

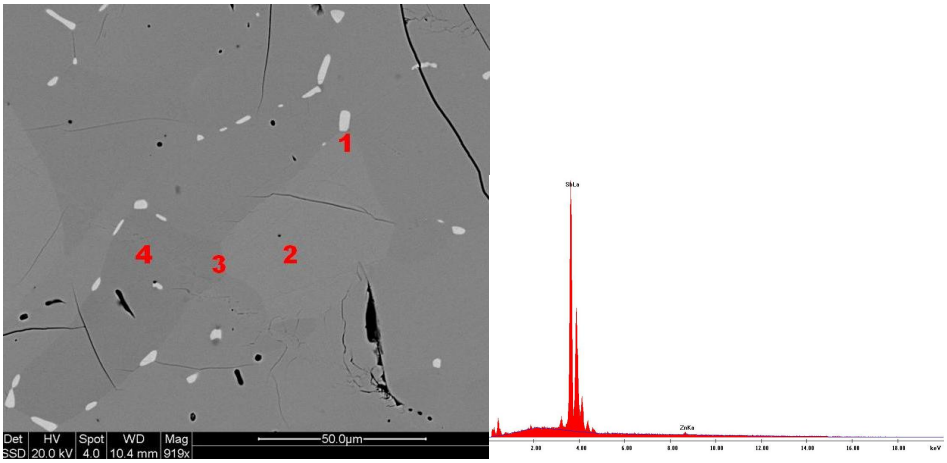

(a) (b)

Figure 5.7: Experimental result: $Zn_{49.5}Mn_{0.5}Sb$ investigated by SEM and EDS analysis. (a) Backscattered electrons image of $Zn_{49.5}Mn_{0.5}Sb(\#B4)$. Four positions are detected. “1” is defined as Sb, others three are defined as ZnSb. (b) EDS analysis, the high peak is labeled as Sb Lα and Zn yields a weak signal which is labeled as Zn Kα in the right.

In the observation to sample Group B, which is synthesis with annealing, the composition of the whole sample is 50.01%Sb, 2.46%Cr and 4.53%Zn in $Zn_{46}Cr_4Sb$ indicating the existence of Cr. The dendritic area, labeled "1”, is determined as 49.91%Sb, 41.70%Cr and 8.63%Zn, , with EDS analysis showed on Fig.5.8(a) and (b), considered as CrSb. The highest peak is SbL, while the next right one is CrL. The lowest two are ZnL and ZnK respectively. The detectable Zn is considered scattering. The melting temperature is around 900°C, which is high that the solidification tempperature of $CrSb_2$. CrSb forms fristly during quenching. With temperature droped down, the peritectic process occurs to create $CrSb_2$, and in further (Sb). During annealing, $CrSb_2$ disappeared by diffusion in order to balance the atomic portion. From the lever rule, we know the composition point is sitting in either ZnSb-CrSb-$CrSb_2$ or ZnSb-CrSb-(Sb). The (Sb) is evidently detected.

Therefore, the third phase should be CrSb rather than $CrSb_2$. The phase diagram of Cr-Zn[38] also suggests the existence of $CrZn_{13}$ and $CrZn_{19}$, which is not considered due to wee did not find a Zn-rich phase.

The third phase with 53.01%Sb, 38.76%Mn and 8.23%Zn in $Zn_{49.5}Mn_{0.5}Sb$ and 53.99%Sb, 45.86%Mn and 3.15%Zn in $Zn_{46}Mn_4Sb$ were found. They are considered as MnSb. Referred to the phase diagram of Mn-Sb, the solidification temperature of Mn-Sb is much high than Zn-Sb. When temperature droped, with the sufficient Sb, the binary phase in Mn-Sb system is MnSb and Sb. With the temperature decreased continuously, Zn-Sb start to solidify. Therefore, MnSb and Sb should be closed together. It is indeed found besides of Sb phase, which is showed on Fig.5.8(c). We are not surprise to obtain a relative weaker signal of Mn in the EDS analysis for this area due to the large scale of scattering from pure antimony. Fig.5.8(d) shows the three phases observed by SEM. The much more complicated phase diagram of Mn-Zn suggests the muti-phases exist, but most of them are Zn-rich, which are not found in our samples.

In the observation to sample Group D, which is synthesized with sintering, a third phase with 51.04%Sb, 40.30%Mn in $Zn_{46}Mn_4Sb$ and 65.89%Sb, 31.67%Cr in $Zn_{46}Cr_4Sb$ were found, defined as MnSb and CrSb. However, we did not detect these, except for the 81.72%Sb in $Zn_{49.5}Mn_{0.5}Sb$ and 81.37%Sb in $Zn_{49.5}Cr_{0.5}Sb$ in addition to the ZnSb phase.

X-ray diffraction results give us the more precise information about phase constitution. The XRD profiles are shown in Fig.5.9.

The upper two are a comparison of annealed and sintered $Zn_{46}Cr_4Sb$ and $Zn_{46}Mn_4Sb$, respectively. The bottom two are a comparison of 4% ad 0.5% Cr/Mn, respectively. Calibrated by Si, the profiles are fitted in the ZnSb.

From Fig.5.9 (a) and (c) we see that the sintered $Zn_{46}Cr_4Sb$ contains CrSb and $CrSb_2$ in addition to ZnSb. It may seem a little surprising that the sample contains $CrSb_2$ in $Zn_{46}Cr_4Sb$. The reason might be peritectic process occurred, or some zinc are lost during synthesis, or insufficient annealing time. By contrast it is very difficult to find the peak else than ZnSb in $Zn_{46}Cr_{0.5}Sb$. We know, however, from SEM that the sample consists of more than ZnSb. If we have only stoiciometric

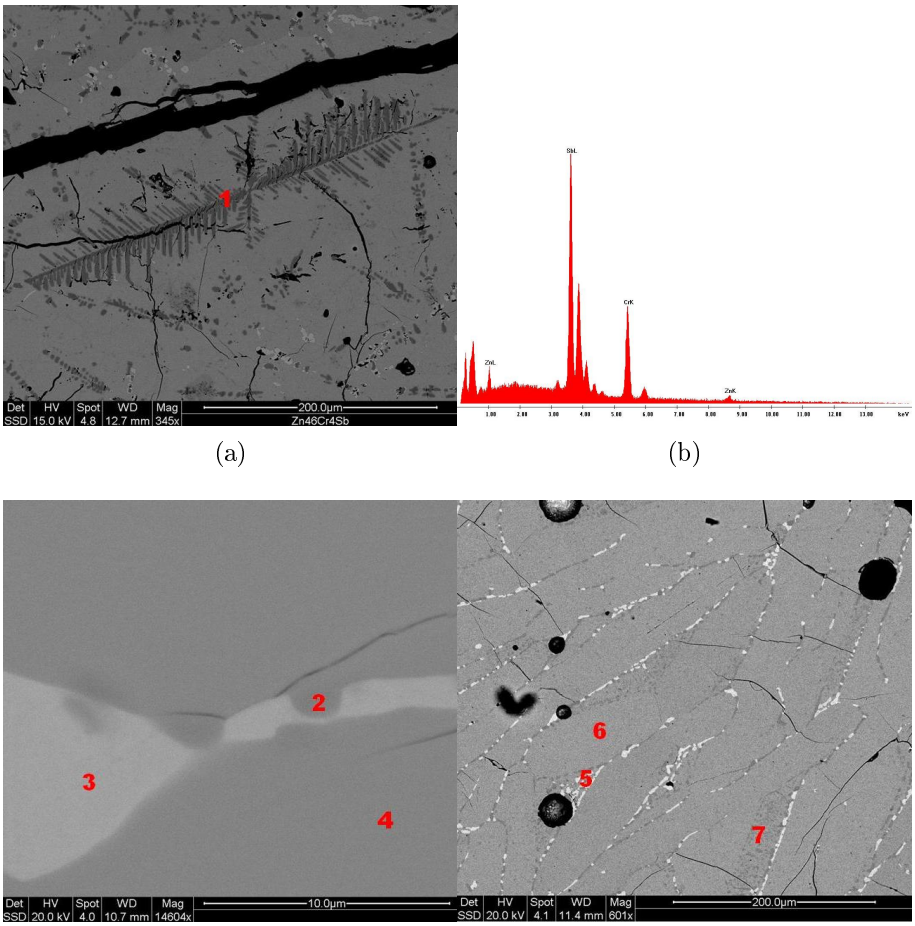

(a) (b)

(c) (d)

Figure 5.8: Experimental result: phase determination by SEM. (a) $Zn_{46}Cr_4Sb$, sample ID:#$B2$, the dendritic structure labeled "1". (b)EDS analysis for "1" in (a), the composition showed 51.07%4Sb, 39.94%Cr, 8.99%Zn which is considered as $CrSb_2$; (c) MnSb is found in $Zn_{49.5}Mn_{0.5}Sb$, "2"- MnSb, "3"- Sb, "4"- ZnSb; (d) multi-phase in $Zn_{46}Mn_4Sb$, "4"- ZnSb, "5"- (Sb), "6"- MnSb

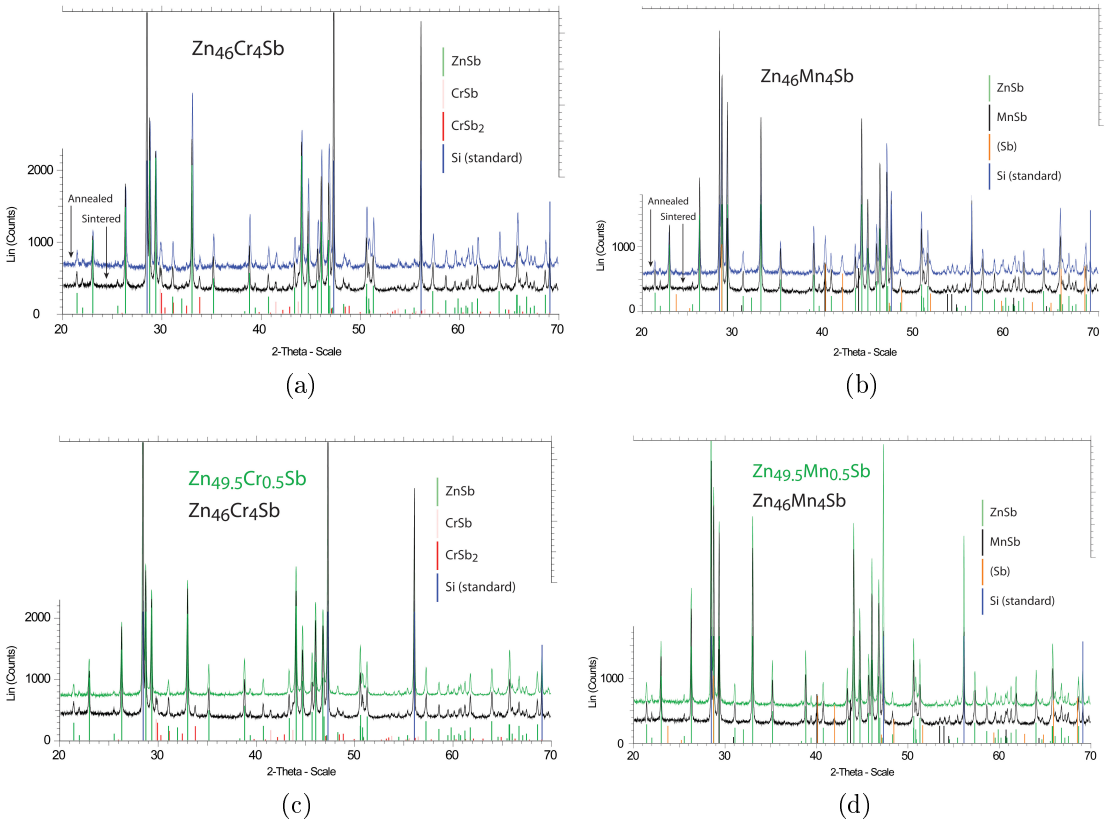

Figure 5.9: Experimental result: XRD profiles. (a) comparison of annealed and sintered $Zn_{46}Cr_4Sb$; (b) comparison of annealed and sintered $Zn_{46}Mn_4Sb$, (c) comparison of $Zn_{46}Cr_{0.5}Sb$ and $Zn_{49.5}Cr_{0.5}Sb$, (d) comparison of $Zn_{46}Mn_4Sb$ and $Zn_{49.5}Mn_{0.5}Sb$. The background has been shifted for clarity. Blue lines show position of the reflexes from silicon, used as an internal standard. The other lines that are marked are taken from literature.

ZnSb and CrSb in the samples, the lever rule tells us that the amount of CrSb in $Zn_{49.5}Cr_{0.5}Sb$ is only 1/8 of the amount in $Zn_{46}Cr_4Sb$. This amount would be difficult to be detected. In the figure of (b) and (d), The (Sb) and MnSb are confirmed in both of the of $Zn_{46}Mn_4Sb$ and $Zn_{49.5}Mn_{0.5}Sb$ in addition to ZnSb. It can be seen that a little more (Sb) exist in the sintered sample.

5.4 Result of Electrical properties

5.4.1 Contact resistance and I-V curves

The reasons for measuring the contact resistance was explained in section 4.4.1. Here we first comment on measurements of electrical properties of samples of group A. These were annealed but not sintered. They did contain cracks. Sometimes the polishing might mask the visual observation of cracks in routine observations which did not reveal obvious severe crack. However it was found that these samples were very fragile and they were easily broke apart. The pressure from the needle probe might be sufficient to break the sample in two. Many measurement series were started, but the samples broke before the measurements were completed. The sintered samples group C, were much sturdier than those that where not sintered.

Before presenting contact resistance measurements we want to show some data related to the measurements with needle end contacts (not soldered). These were predicted to have high contact resistance and provide an easy case for measuring the contact resistance. It turned out to be untrue; in further, be practically impossible to get reliable measurement data. In addition to the sample breaking for the non-sintered samples. We think the unreliability and instability of the data for those samples is due to instability in the point contacts. We find support for that from Fig 5.10 which shows several IV measurements on samples with needle end contacts.

For each of the samples shown in Fig.5.10 the IV curves should ideally be identical. They vary a lot from measurement to measurement and some are erratic. They are also nonlinear. One can only speculate for detailed reasons why mechanical

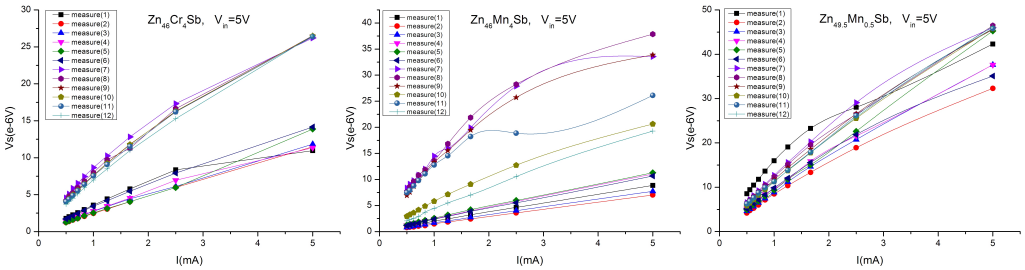

(a) (b) (c)

Figure 5.10: Experimental result: I-V curves measured with needle point contact probes. The curves were measured by AC current. There are three different sample pieces shown: (a) $Zn_{46}Cr_4Sb$(#A1); (b) $Zn_{46}Mn_4Sb$(#A3); (c)$Zn_{49.5}Mn_{0.5}Sb$(#A4). These IV-curves should for each sample have been identical. That they are not is interpreted as most probably due to the point contacts not being stable.

needle probes turns unstable, however it does not appear as a mystery that they do.

One contributing reason could be the probes being mechanically unstable over time, inducing the change of contact resistance. The probes are spring loaded, and the contact point can be dislocated by any expansion of the sample induced by any reason. If the sample or sample surface is partly porous the deformation or micro breakage could happen and contribute to displacement and instability of the contacting point. We have observed that our Zn-Sb based samples can have porous features, rationalized as related to the complicated phase sequences and thermal shrinking the Zn-Sb goes through by the synthesis as discussed previously.

We now report on contact resistance measurements on samples with soldered contact as described in section 4.4.1. The IV characteristics for these samples were in general stable. Both AC and DC measurements yielded linear IV curves and all of the measurements were repeatable. For soldered contacts, the measurement procedure with moving probes described in section 4.4.1 can be used to investigate the contact resistance. The experimental results are plotted on Fig.5.11.

The different discrete symbols are experimental measurements, and the lines are linear fits calculated by **MATLAB**. As outlined in section 4.4.1 the contact resis-

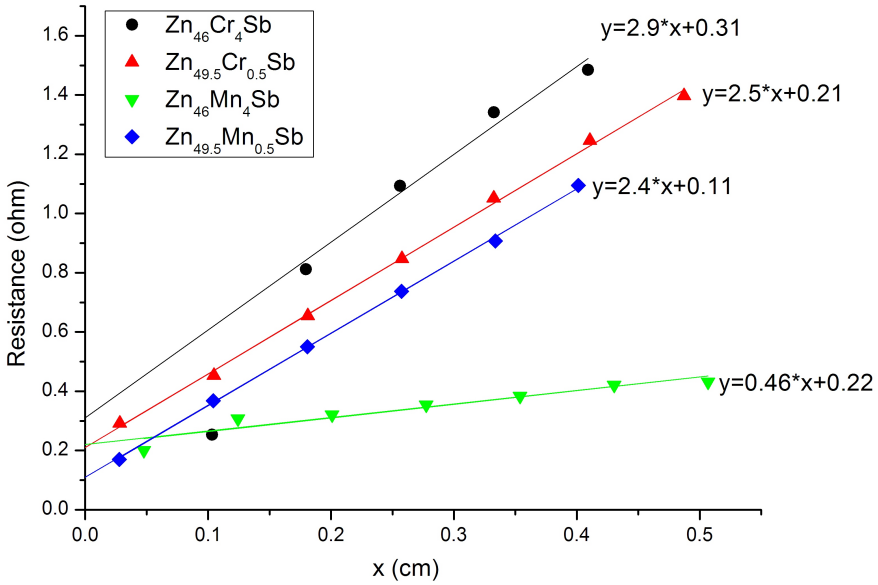

Figure 5.11: Experimental result: Resistance as a function of position of probes with soldered end contacts. Samples from group C. i.e. sintered material.

tance are given by the intercept of the lines with the y-axis. The experimentally observed contact resistances have been listed in table 5.1.

Table 5.1: Contact resistances of soldered contacts to samples that have been sintered.(Ω)

Contact Resistance R_c(group C)			
$Zn_{46}Cr_4Sb$	$Zn_{49.5}Cr_{0.5}Sb$	$Zn_{46}Mn_4Sb$	$Zn_{49.5}Mn_{0.5}Sb$
0.31	0.2 1	0.2 2	0.11

The total resistance of the sample is larger than 2Ω. Thus the contact resistance is a small fraction of the total resistance, except for this piece of $Zn_{46}Mn_4Sb$. However it can not be ignored. An IV curve through soldered end contacts can give a valuable indication of differences in resistivity of different samples, but we need to be cautious in our interpretations of differences in I-V curves as they also could be due to differences in contact resistance.

We will here describe some measurements that can be relevant for indicating how reproducible the contact resistance is for similarly prepared contacts to the very

same sample(s). The experiments were not planned to shine light on that question though. We used a sample series for which we had measured the contact resistivity with moving probes. Then the contacts were removed for doing other measurements. Then the contacts were re-soldered again and IV curves with AC measurements and DC measurements were performed. From the IV curves (which all were linear) we measured the total resistance ($R_s + R_c$). We then assumed that the resistivity of the sample and the sample resistance was unchanged from that measured by the previously described moving probe experiment. (We will present the resistivity data of that experiment in section 5.4.2). Initially we can say if we regard the resistivity as a property of the particular sample, this would be true. The deduced contact resistances are shown in Table 5.2. We stress that this is not intended as a measurement of R_c, it is an exploration of consistency and repeatability of data.

Table 5.2: Hypothetical contact resistance numbers deduced from IV measurements on re-soldered contacts to same samples as that of table 5.1.(Ω)

Contact Resistance R_c(group C)				
	$Zn_{46}Cr_4Sb$	$Zn_{49.5}Cr_{0.5}Sb$	$Zn_{46}Mn_4Sb$	$Zn_{49.5}Mn_{0.5}Sb$
AC	0.48	0.35	1.24	-0.47
DC	0.32	0.65	1.13	-0.53

It is seen that the deduced contact resistance are somewhat within the same order of magnitude as the values of Table 5.1. The AC and DC values are also similar to each other. The value of above 1Ω for $Zn_{46}Mn_4Sb$(C) appears higher. It seems reasonable that the contact resistance could change by re-soldering, however appearance of a negative contact resistance is unphysical. So either this is due to the total measurement uncertainties being of the order of the absolute value of the negative contact resistance or there is an untrue assumption behind the experiment. Both seem possible and may be related. For the measurement on $Zn_{49.5}Cr_{0.5}Sb$ in Table 5.2 we see that there is a difference between the AC and DC values of 0.3Ω. This can be taken as a rough indication of the experimental uncertainty and its value is not very different from the negative values of Table 5.2. There is also one perhaps questionable assumption in the experiment, namely that the sample resistance does not change by re-soldering the sample and that the sample resistance is stable. It is possible to think that the resistivity of the sample could be altered by the hot temperature and temperature cycling of soldering; Cracks could develop as a result of the thermal stress, the sample and its internal grain

boundaries could be subject to some oxidation causing altered carrier transport between the grains, diffusion can also change the morphology. Some relaxation of built in stress might also occur in the sample at any time causing a change in resistivity and contributing to the total measurement uncertainty for measurement of resistivity and contact resistivity of samples.

We now present a series of IV curves and discuss their features mainly in terms of whether thermoelectric effects itself influence the measurement of resistance of samples. Fig.5.12 shows IV curves measured by DC and AC respectively on on the same sample set consisting of sintered samples with soldered end contacts. Each sample has here been measured multiple times and the measurements fall on top of each other. The IV curves are evaluated as straight lines with no bends for neither the AC nor the DC measurements. Based upon what is written in textbooks on measurement techniques for thermoelectric materials (Chapter 8 in[10]), this is taken as an indication that thermoelectric effects do not influence the measurements of resistance, and therefor resistivity, for material parameters like that of the current set of samples of Fig. 5.12.

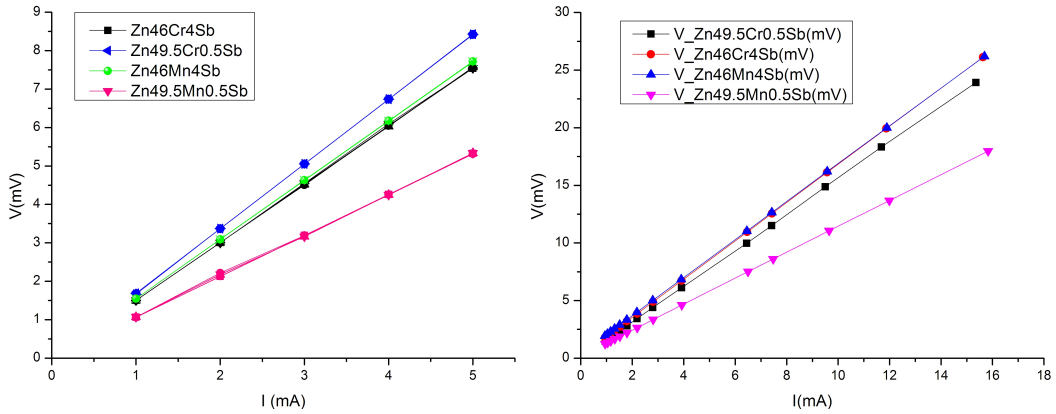

(a) (b)

Figure 5.12: Experimental result: I-V curve of AC and DC measurement. (a) DC measurements were taken 5 times for each sample. I-V curve are closed fitting; (b) AC measurements. IV curve of $Zn_{46}Cr_4Sb$ and $Zn_{46}Mn_4Zn$ are overlapped. Samples are from group C.

The parameters of relevance are mainly resistance, Seebeck coefficient, thermal conductivity, sample size. In addition the measurement current is also important. If these parameters had been less favorable then the thermoelectric effects like Peltier effect may cause a thermal gradient to built up over the sample. That

would again induce a Seebeck voltage that would come in addition to the resistive voltage drop across the sample and would influence the IV curves and resistance measured. These effects will in the general case be smaller for AC measurements if built up heat is not able to follow the signal frequency. It has been written that a measurement frequency of 50Hz is sufficiently high to suppress measurement errors caused by thermoelectric effect simply due to the heavy thermal load of regular contacts. We might thus expect to have suppressed these effects at our measurement frequency of 43Hz. In our case the total resistance of the sample is nearly the same for measurement with AC and DC and there is no systematic differences between them and they are considered identical within experimental uncertainty as shown in Table 5.3. It leads us to conclude that we can proceed with electrical measurements to determine the resistivity on these type of samples without significant measurement errors caused by thermoelectric effects.

Table 5.3: Total resistance deduced from IV measurements on soldered contacts to sintered sample pieces.(Group C)(Ω)

Total Resistance R=R_s+R_c(group C)				
	$Zn_{46}Cr_4Sb$	$Zn_{49.5}Cr_{0.5}Sb$	$Zn_{46}Mn_4Sb$	$Zn_{49.5}Mn_{0.5}Sb$
AC	1.663	1.576	1.641	1.129
DC	1.510	1.686	1.544	1.062

5.4.2 Resistivity

Table 5.4 shows a summary of the resistivity values determined from the data shown in Fig. 5.11. These resistivity values are determined from the slopes of the curves as explained in section 4.4.2.

Table 5.4: Resistivity measured by moving probes.Sample ID: Group C.

Sample	R_s (Ω)	Contact resistance (Ω)	Cross-section (cm^2)	Resistivity (Ω·cm)
$Zn_{46}Cr_4Sb$	2.9	0.31	2.27×10^{-2}	6.58×10^{-2}
$Zn_{49.5}Cr_{0.5}Sb$	2.5	0.21	2.70×10^{-2}	6.75×10^{-2}
$Zn_{46}Mn_4Sb$	0.46	0.22	4.95×10^{-2}	2.28×10^{-2}
$Zn_{49.5}Mn_{0.5}Sb$	2.4	0.11	3.70×10^{-2}	8.87×10^{-2}

The resistivity has also been measured by the the van der Pauw method as described in section 4.4.2. In the method very little current flows through the voltage contacts. Thus the contacts are less critical and mechanical pressure contacts was used for measuring the resistivity at room temperature. The results are stable and are summarized in Table 5.5. The same sample has been measured many times with different ranges of currents being used for constructing the IV curves made in the method. Current ranges from 10^{-7} to 10^{-3}A have been used. Fig.5.13 shows the IV curves collected by the measurement sequence in the van der Pauw measurement program for one of the listed current ranges. The curves are linear. The slopes are also independent of the current directions. Some IV curves have offsets on the voltage axis for zero current. These would have caused errors in the determination of resistivity if the only the resistances had been measured and not the slope of the IV curves. Using the slopes and averaging over all contact combinations eliminates much of the systematic errors that can occur in the method. We found that the values obtained for different current ranges are relatively close. In selecting weights for different measurements it is rationalized that the measurements at the smallest current values are least reliable due to smaller signal. The resulting resistivity listed in Table 5.6 is of the same order of magnitude as that of Table 5.3, but they have smaller values. These are different samples so it is reasonable that they do have somewhat different resistivity values. We see no reason to believe it has to do with the measurement techniques.

Table 5.5: Resistivity measured by van der Pauw method.Sample ID: Group D.

Sample	Thickness (cm)	Sheet resistance (Ω)	Resistivity (Ωcm)
$Zn_{46}Cr4Sb$	0.1192	0.206	2.45×10^{-2}
$Zn_{49.5}Cr0.5Sb$	0.2161	0.174	2.07×10^{-2}
$Zn_{46}Mn4Sb$	0.2367	0.104	1.24×10^{-2}
$Zn_{49.5}Mn0.5Sb$	0.2000	0.158	1.88×10^{-2}

We may comment on the value of the resistivity itself. Compared to a semiconductor like Si, this value around $2\times10^{-2}\Omega$cm corresponds to a medium doped Si piece ($n = 10^{18}\text{cm}^{-3}$ range) but to determine what carrier concentration we have we have to measure it by measuring the Hall mobility.

Compared with other method, the resistivity is much smaller. However, it is a ben-

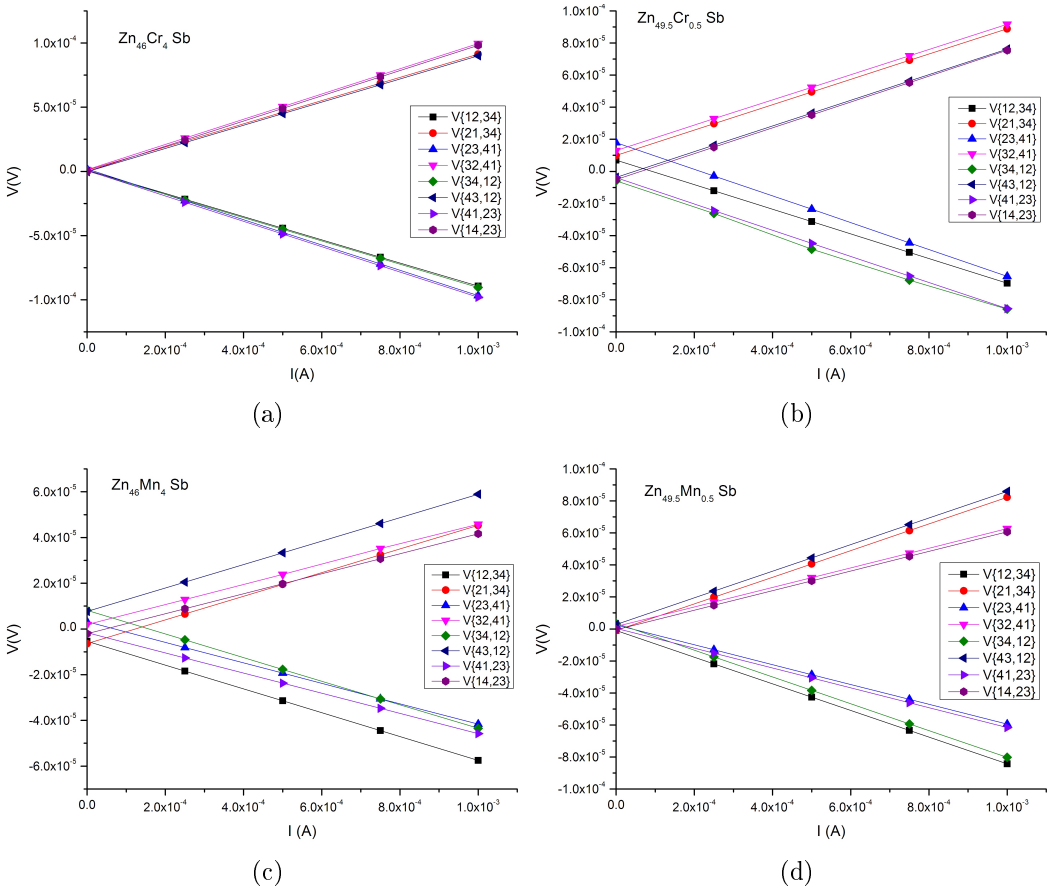

Figure 5.13: Experimexntal result: I-V curve of van der Pauw measurement. Current input:$10^{-7} \sim 10^{-3}$A. "V(12,34)" stands for current input from 1-2 in Fig.4.12(a) and voltage measured from 3-4. (a)$Zn_{46}Cr_4Sb$; (b)$Zn_{49.5}Cr_{0.5}Sb$; (c)$Zn_{46}Mn_4Sb$; (d)$Zn_{49.5}Mn_{0.5}Sb$. Samples are from group D.

efit of van der Pauw method which give zero contact resistance. The points measured the potential difference are far away from the points input current. Fig.5.14 gives the one of the I-V curves of samples. The applied current is $10^{-7} \sim 10^{-3}$A, showing a perfect linear relation between current and voltage. A small offset exist due to the difference bias current between two inputs, which is in the acceptable range. Also, we tested the small input current. When the current is set as $10^{-9} \sim 10^{-8}$A, the I-V curve shows more flat, and a 2∼3 orders of resistivity higher those showed on Fig.5.14. On can see from the result that with the same doped concentration, the resistivity of $Zn_{1-x}Cr_xSb$ is higher than $Zn_{1-x}Mn_xSb$ but not much, turning out the conductivity is higher in $Zn_{1-x}Mn_xSb$.

5.4.3 Carrier concentration and mobility

The carrier concentration and mobility was measured in the van der Pauw sample configuration in a applied magnetic field of 1.02 Tesla. To compensate for geometrical asymmetry, thermoelectrical effects (Seebeck effect) and magneto thermal effects (Nernst effect) we did the measurements perturbing the contact pairs for voltage and current both in forward and reversed direction of the magnetic field. Taking the average value of all minimizes their effects. The results are summarized in Table 5.6. The table show separate measurement series using different ranges of the current. They are all close to each other for the different ranges. The largest deviation is found for the smallest current (rightmost column) where the signals are the weakest.

Table 5.6: Carrier concentration($1/cm^3$) and mobility(cm^2/Vs)

Sample	$10^{-6} \sim 10^{-3}$	$10^{-6} \sim 10^{-4}$	$10^{-7} \sim 10^{-3}$	$10^{-7} \sim 10^{-4}$
Carrier concentration:				
$Zn_{46}Cr4Sb$	5.4840×10^{17}	5.3606×10^{17}	5.4857×10^{17}	4.9555×10^{17}
$Zn_{49.5}Cr0.5Sb$	2.7422×10^{17}	2.7416×10^{17}	2.7195×10^{17}	2.2130×10^{17}
$Zn_{46}Mn4Sb$	6.5766×10^{17}	6.2080×10^{17}	6.5233×10^{17}	6.6782×10^{17}
$Zn_{49.5}Mn0.5Sb$	3.0289×10^{17}	2.9768×10^{17}	3.0334×10^{17}	3.0436×10^{17}
Mobility:				
$Zn_{46}Cr4Sb$	30.029	30.752	30.009	34.129
$Zn_{49.5}Cr0.5Sb$	71.062	73.624	71.701	72.346
$Zn_{46}Mn4Sb$	49.710	53.535	50.129	47.503
$Zn_{49.5}Mn0.5Sb$	70.845	72.287	70.732	70.477

First it is important to comment that all the samples are found to be p-type by the sign of the Hall voltage. That is not obvious. One might expect ZnSb to be a p-type simply because that is the conductivity type that is reported for undoped ZnSb. Since we have added Cr and Mn respectively and these additions have not been reported before it is not obvious that it should turn out p-type. We do not know to which degree Cr and Mn will dissolve into ZnSb and don't know wether they will substitute for Zn or Sb or wether it prefer an interstitial position or wether it's electrical effect if any is that of influencing the native point defect structure.

Intrinsic ZnSb is found to be a p-type semiconductor as described in section 3.3 and 3.4. In a historical simplified perspective it was considered that ZnSb could tentatively have been understood as a material where the Fermi level was in the valence band and thus always led to p-type (unless very heavily doped) while current prevailing consensus seems to be describing it as an electron poor framework semiconductor where the Fermi level of intrinsic material is sitting in the middle of the band gap shown in Fig.3.9. In that view ZnSb could be p-type or n-type depending upon the character of dopants.

Let us discuss the expected character of the dopants used in this thesis. Firstly in the case of Cr, it has half full shell both in d and s. If the Cr occupies a Zn-site in ZnSb, the Zn-like bonding(the missing electron in $4s$) states will accept an electron from the valence band leaving a (localized) hole there, then Cr_{Zn} should acts as an acceptor. While for a Cr to occupy the Sb-site, we speculate that the five d-electrons would go into satisfying the bonding. This could yield the excessive s-electron provide electron to conduction band, thus, $\mathrm{Cr_{Sb}}$ act like a donor. If so it could a an donor.

In the case of Mn, it has two electrons in the outer $4s$ shell. If it occupies in Zn-site, the bonding of $\mathrm{Mn_{Zn}}$ might be satisfied without any exchange of the charge for this site due to the two $4s$ electron in $\mathrm{Zn_{Zn}}$ as well. It is nevertheless a foreign atom and will create localized electron states. These may be fall in the band gap and $\mathrm{Mn_{Zn}}$ can be acceptor-like or donor-like dependent upon whether they are occupied (donor like) or empty (acceptor like) at 0K. On the other hand, if the Mn occupies the Sb-site, it may be speculated that $\mathrm{Mn_{Sb}}$ could act as a double donor by the d electrons of Mn satisfying the bonding of the site and the two s electrons being given away to the conduction band.

For the compositions synthesized in this thesis, which are on the Sb-rich side for ZnSb it is expected that the solid is in favor of high Zn vacancy concentration. Therefore we would expect that Cr and Mn prefer to occupy the Zn-site much more than the Sb-site,which means that Zn-site situation to most probable among the substitutional site.

We now want to turn to dealing with the carrier concentrations which we have measured for the samples and that are given in Table 5.6. We see they vary from $2.2\times10^{17}\mathrm{cm}^{-3}$ to $6.6\times10^{17}\mathrm{cm}^{-3}$ for the different samples. This is a very small

range of hole concentrations. We find it surprising because the atoms and different overall compositions of dopants involved. If for example Cr acted as an acceptor then the carrier concentration should reflect the difference in Cr concentration. However the hole concentration is largest for the sample with the lowest overall Cr concentration. For the Mn case the hole concentration is largest for the highest overall Mn concentration, which viewed isolated supports the view that Mn acts a acceptors. However the range spanned by the overall composition of Mn is much larger (a factor of 8) than the range spanned by the hole concentration (a factor of 2). It weakens the view of considering Mn as an acceptor, but one could argue that it might hit the solubility limit somewhere in that range and the attainable hole concentration would then also saturate. However the Cr case covers essentially the same (small) range as that of Mn but in reverse order, and the variations in the systematics of the resistance of the different pieces of the samples make one suspicious that the variations observed in carrier concentration sort of reflect the variation in reproducibility of the sample synthesis procedures.

Even if the observed carrier concentration variations between different samples may not be a systematic reflecting the intentional differences between the samples it is natural to wonder why the carrier concentration ends up in this particular small range.

One could be speculated is that the material is close to intrinsic. However it should be aware that the intrinsic carrier concentration is not known for the material, there are uncertainties about how accurate models for calculating the intrinsic carrier concentrations and the uncertainties are about the values to plug into the model. In section 5.4.4 we will estimate the intrinsic carrier concentration at room temperature. We get a value of $3.4\times10^{16}\mathrm{cm}^{-3}$, which is not that far off the carrier concentration we measured. The material would be intrinsic if the solid solubility of the elements Cr and Mn was smaller than this value and other impurities did not provide doping. The carrier concentration could also end up in the small range of values if defects dominated. If the samples all have by hypothetically many defects and if these defects result in many states in the band gap, that defects often do that, the Fermi level could be pinned in the band gap. Under such hypothetical situations the Fermi level, and thus the carrier concentration, would not be sensitive to doping unless the concentration outnumbers the states. If the solubility of Cr and Mn in ZnSb is low, then it may not be possible to observe any effect of the doping that might occur. However, it is beyond of this thesis to

calculate the solubility of Cr or Mn in ZnSb.

5.4.4 Temperature-dependence of resistivity

Even if the temperature range is limited within 120K to RT, the Cryogenic method gives us a good understanding of resistivity change as different temperature. Fig.5.14 gives the results of cryogenic measurement, that the resistance changes as a function of temperature. The points marked with different symbols are measured results and lines are quadratic fitting curve. The resistance decrease with increasing temperature as a nonlinear relation.

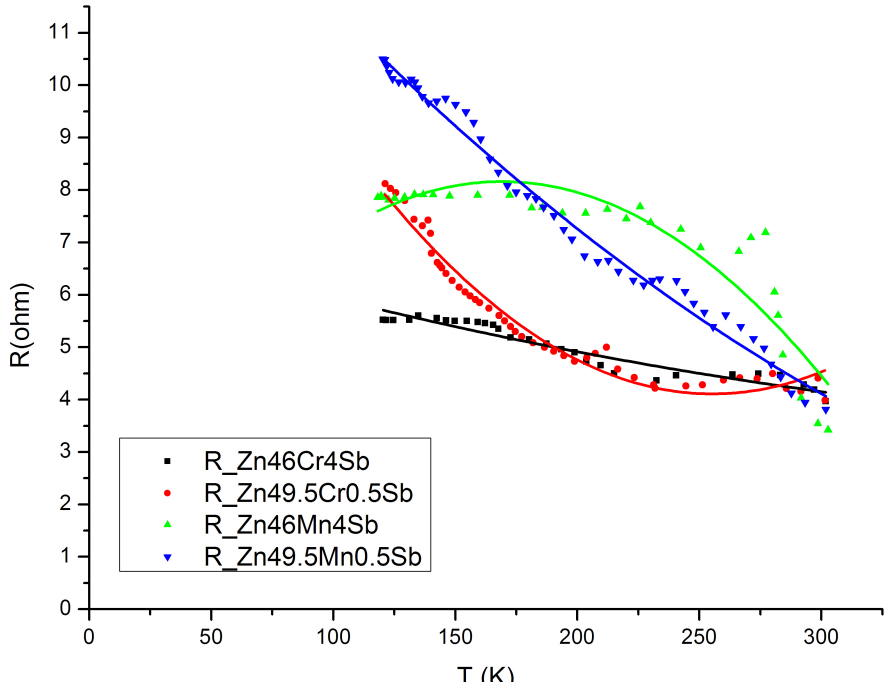

Figure 5.14: Experimental result: Resistance change as a function of temperature. Temperature range: 120K∼ RT. Sample ID:Group D

From the result, we can see that the resistance changes with temperature for different sample are similar. Even if they have different features, all of the curves agree the same tendency. This is not unexpected since carrier concentration of all of the samples are not significant distinguished. Before we discuss the temperature-

dependence of resistivity, one is supposed to be clear the factors influenced the resistivity.

Recalling equation(2.8), it gives

$$\frac{1}{\rho(T)} = \sigma(T) = qp\mu(T) \tag{5.1}$$

The variation of resistivity depends on the carrier concentration and mobility.

Based on equation(2.3) and (2.4), the intrinsic carrier concentration is calculated by[10]

$$p_i = 2(\frac{2\pi m^* kT}{h^2})^{3/2} exp(\eta) \tag{5.2}$$

where η is the reduced Fermi energy, which $\eta = -E_g/2kB$, whiere $E_g = 0.58eV$ at RT agreed by most of literatures. The intrinsic carrier concentration is $3.43\times10^{16}\text{cm}^{-2}$. The carrier concentration of the samples are measured as the order of $\sim 10^{17}$, which is close to the intrinsic carrier concentration.

The contribution from mobility depends on the scattering mechanisms, which are from acoustic lattice scattering, neutral impurity scattering and impurity scattering, labeled as -1/2, 0 and 1/2 shown in Fig.5.15. The carrier concentration

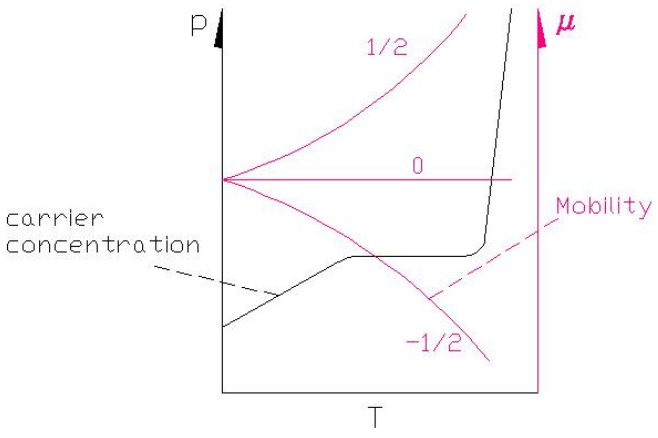

Figure 5.15: Discussion: Temperature-dependence of p and μ. Temperature-dependence of resistivity is influenced by carrier concentration (left axis) and mobility (right axis). 1/2, 0, -1/2 labeled on mobility stand for acoustic lattice scattering, neutral impurity scattering and impurity scattering, respectively.

change as a function of temperature is also shown in Fig.5.15. We can compare the measured curve with Fig.5.15. If it follows a tendency of mobility curve, then one can be estimated is the mobility dominate the temperature dependency of resistivity. Otherwise, it is dominated by the curve of concentration if the measured curve follow the carrier concentration curve. However, the measurements we have done in this thesis does not show a clear tendency. This leave us an interesting phenomenon.

5.4.5 Thermal conductivity

The measured thermal diffusivity is listed in Table 5.7. and calculated thermal conductivity based on equation(4.12) is plotted on Fig.5.16.

Table 5.7: Measured thermal diffusivity (mm^2/s)

T(°C	25	50	100	150	200	250	300	350
$Zn_{46}Cr4Sb$	1.137	1.055	0.904	0.804	0.74	0.708	0.711	–
$Zn_{49.5}Cr0.5Sb$	1.005	0.925	0.782	0.667	0.593	0.559	0.556	0.595
$Zn_{46}Mn4Sb$	1.959	1.820	1.547	1.391	1.283	1.224	1.202	1.253
$Zn_{49.5}Mn0.5Sb$	1.079	0.972	0.832	0.725	0.667	0.632	0.626	0.649

The results show the measurement of $Zn_{46}Mn_4Sb$ is significant higher than other samples. One of the reasons could be the material itself, another could be influenced by the perfection of geometry. The sample was broken and missed a corner during shaping. To fixed it, a piece of mica is used to cover the corner and stop the laser go through it. The mica is cover by an absorbing carbon film, just like the sample, prior to measurements. Even if mica is a good isolator in certain points, the heat could be transparent it with possibility. Compared with the thickness of sample, the thickness of a piece mica is fairly less. A small step is expected to observe on the curve of temperature over time. The comparison of detected signal of $Zn_{46}Mn_4Sb$ with imperfect geometry and$Zn_{46}Cr_4Sb$ with perfect geometry are showed on Fig.5.17. A bulging on$Zn_{46}Mn_4Sb$ proved the prediction.

Except for the $Zn_{46}Mn_4Sb$, other samples show a close, or even lower, value of thermal conductivity compared with those reported in literatures, such as

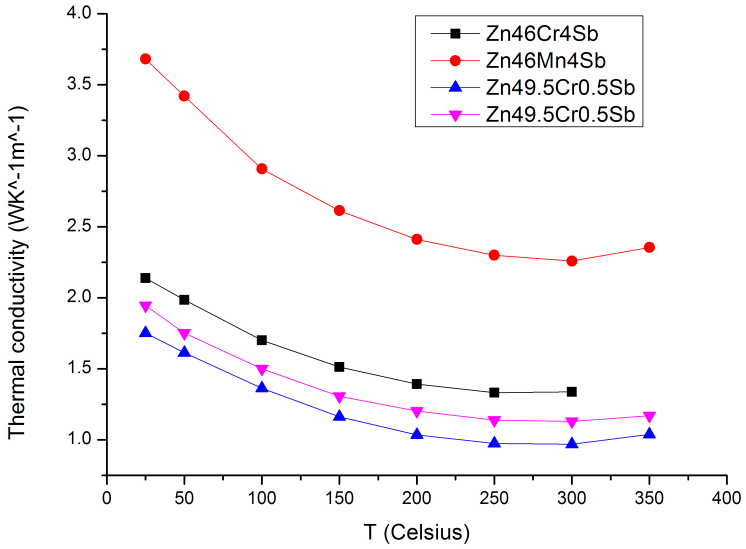

Figure 5.16: Experimental result: Thermal conductivity measured by laser flash. Temperature range: 25°C ∼350°C(300°C for $Zn_{46}Cr_4Sb$).

2.8$WK^{-1}m^{-1}$(RT) in ref.[30], 2.3$WK^{-1}m^{-1}$(RT) in ref.[39]. Also, compared with the measurements of ZnSb which has been done by LFA 457 MicroFLASH in previous work, that κ being around 2 $WK^{-1}m^{-1}$, they have no significance difference, indicating no instrument errors. The higher thermal conductivity of Zn_{46}Mn4Sb is considered that it could be stemmed from the heat transparent the missing corner, or could be the sample itself.

Let us discuss the value of the observed conductivity in terms of heat transport by phonons charge carriers in the material. The thermal conductivity is contributed from electrical thermal conductivity and lattice thermo conductivity, $\kappa = \kappa_e + \kappa_l$. The change of κ_e is proportional to the carrier concentration. However, considering values from Table 5.7, the difference between each samples is not scale of the difference of carrier concentration.

The electrical thermal conductivity can be calculated by Weidemahn-Franz law,

$$\frac{\kappa_e}{\sigma} = \frac{L}{T} \tag{5.3}$$

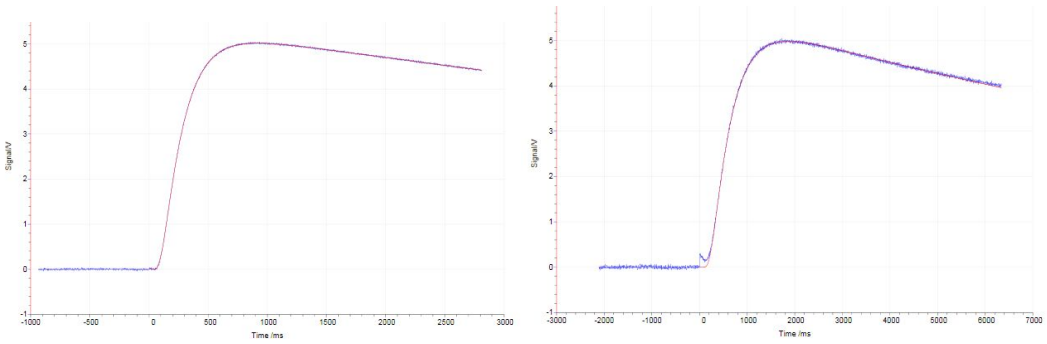

(a) (b)

Figure 5.17: Experimental result: comparison of signal vs.time for perfect and imperfect geometry. (a)$Zn_{46}Cr_4Sb$(#D1) has the perfect geometry, the round disk shown in Fig.4.12(b), for laser flash measurement, a round; (b)$Zn_{46}Mn_4Sb$(#D3) has an imperfect geometry as corner-off, shown in Fig.4.17. The signal yielded as a function of time, a small bulging is stemmed from the laser passing through the mica due to its transparency.

where L is the Lorenz number and $L = 2.44 \times 10^{-8} \mathrm{W\Omega K^{-2}}$. It gives

$$\kappa_e = LTqp\mu \tag{5.4}$$

The thermal conductivity contributed by κ_e at RT are calculated by inserting the measured values for μ and p and listed in Table 5.8.

Table 5.8: The thermal conductivity contributed by κ_e (W/mK)

$Zn_{46}Cr_4Sb$	$Zn_{49.5}Cr_{0.5}Sb$	$Zn_{46}Mn_4Sb$	$Zn_{49.5}Mn_{0.5}Sb$
2.7×10^{-3}	3.1×10^{-3}	5.4×10^{-3}	3.5×10^{-3}

Compared to the measured total thermal conductivity, this tells us that the electrical thermal conductivity contributes a small portions to the total κ.

Chapter 6

Conclusion

The objective of the work in this thesis is to synthesize the thermoelectric material ZnSb with additions of Cr and Zn, which would be suitable for the electrical characterizations, and implement locally measurements for the electrical characterization of these kind of samples.

Experimentation on thesis has been carried out. Additions of Cr and Mn to ZnSb have been studied for the first time to our knowledge and we synthesized several batched of the same compositions: $Zn_{46}Cr_4Sb$, $Zn_{49.5}Cr_{0.5}Sb$, $Zn_{46}Mn_4Sb$ and $Zn_{49.5}Mn_{0.5}Sb$. Two main sample strategies have been studied: i) melting, solidifying and annealing; ii) the same followed by grinding and sintering. Both could be made samples of, however, the first category was fragile and reliable measurements was therefore also difficult while the second category was much easier to handle a reliable electrical measurements could be made.

The samples underwent melting and annealing have large grain size, while the samples are subjected to the sintering afterwards possess small grains. Except for this, the sample synthesized by sintering have less oxidation.

By the synthesis, we got the multi-phase for the samples, which includes Sb and ZnSb in all samples. CrSb are found in $Zn_{46}Cr_4Sb$ and MnSb both in $Zn_{46}Cr_4Sb$ and $Zn_{49.5}Mn_{0.5}Sb$, which has been proved by SEM and XRD. It is difficult to

prove the existence of CrSb in $Zn_{49.5}Mn_{0.5}Sb$ due to the small quantity. A small peak of $CrSb_2$ is showed in $Zn_{46}Cr_4Sb$ XRD profile, might be stemmed from the eutectic process.

The measurements is difficult to run with fine probe contacts due to the serious micro-crack on or above the surface. However, solder contact is a good solution. The contact resistance of solder is measured by moving probes measurement, and estimated in AC measurements. In both case, it keeps a low value, within 1Ω, which verifies the feasibility of measurement methodologies. The similarity of results from AC and DC measurements indicates that either of those can be used for the investigate the electrical properties of samples.

The resistivity has been measured by moving probes for the bar-shape samples and by van der Pauw method for disk samples, both are sintered samples. The different piece of samples shows the different resistivity. The later one shows the value around $2\times10^{-2}\Omega$cm for the sample doped with Cr, and a relative lower value around $1\sim2\times10^{-2}\Omega$cm for the sample doped with Mn, which are lower than those bar-shape samples with $8\sim9\ \times10^{-2}\Omega$cm. The carrier concentration is in the range of 10^{17}, which is closed to the intrinsic carrier concentration. The mobility which has been measured is 30∼70 cm^2/Vs at room temperature, which is somewhat higher than reports in literatures for ZnSb. Based on the carrier concentration value and dependency on overall composition, one can be concluded is the doping efficiency is low to the materials prepared in this thesis. The temperature dependence of the resistivity indicate interesting difference between the different sample compositions and indicates some possible points to follow up in future work.

Thermal conductivity shows a similarity with the previous work. However, there also are some surprising results. The $Zn_{46}Mn_4Sb$ has a higher thermal conductivity, which could be either of the geometrical reason or material itself. This can be studied in the future.

Chapter 7

Suggestion of future work

Based on the experience of this thesis, the synthesis method can be improved in order to obtain more reliable measurement. The materials for electrical characterization are better to be sintered rather than annealed. The sintering temperature needs to keep 350∼400°C, in order to avoid melting.

The doping concentration is influenced by the dopant itself. The measurements found that there could be a saturated limitation below 4% of dopant. Therefore it is a possible work to calculate the solubility of dopant in host materials so as a reference to dope the materials.

The temperature-dependence of resistivity can be investigate in the large ranger of temperature. Measurements can be done in Helium cooling to obtain the change in a even lower temperature. It also could be different domination mechanism in the different temperature range. We discuss whether it is stemmed from the mobility or carrier concentration, which is mentioned in chapter 5.4.4.

Further theoretical considerations of the role of Cr and Mn in ZnSb should be undertaken. And other elements than Cr and Mn could also be explored.

Appendix A

List of selected Symbol

α	Seebeck coefficient
α_A	the Seebeck coefficient of materials A
α_B	the Seebeck coefficient of materials B
α_{AB}	the Seebeck coefficient of a coupled materials A and B
∇T	thermal gradient
ΔT	temperature difference
ΔV	potential difference
ε	electrical field
π_{AB}	Peltier coefficient of a thermocouple
I_Q	heat current
I_{QAB}	the rate of heat absorbed or liberated at the junction between A and B
β	Thomson coefficient
I	electric current
E_{out}	electrical energy output
η_C	Carnot efficiency
ZT	figure-of-merit
σ	electrical conductivity
ρ	resistivity

κ	thermal conductivity
κ_e	electrical thermal conductivity
κ_l	lattice thermal conductivity
$\alpha^2\sigma$	power of factor
L_{ij}	transport coefficient
$D_{1s}(E)$	density of state for idealized semiconductor
m^*	electron effective mass
h	Planck's constant
$f(E, E_F)$	Fermi-Dirac distribution
E_C	conduction band energy
E_V	valence band energy
E_F	Fermi energy
k_B	Boltzmann's constant
n	electron carrier concentration
p	hole carrier concentration
n_i	intrinsic carrier concentration
N_A^-	ionized acceptor concentration
N_D^+	ionized acceptor concentration
j	current density
q	elementary electron charge
v_d	drift velocity
μ	carrier mobility
η	reduced Fermi energy
τ	relaxation time
r	characteristic factor of scattering process
R_{sheet}	sheet resistance
B	magnetic field
C_P	heat capacity
R_c	contact resistance
R_s	sample resistance
L	Lorenz number

Bibliography

[1] *Proceedings Ict'97 - XVI International Conference on Thermoelectrics, 757-760, 771*, 1997.

[2] Karl Erik Almin. The crystal structure of cdsb and znsb. *Acta Chemica Scandinavica 2, 499-407*, 1948.

[3] G. Chen, M. S. Dresselhaus, and G. Dresselhaus. Recent developments in thermoelectric materials. *Int. Mater. Rev. 48 (1), 45-66*, 2003.

[4] Wayne D.Kaplan David Brandon. *Microstructural Characterization of Materials, 2nd.* WILEY, 2008.

[5] D.M.Rowe, editor. *CRC Hand book of Thermoelectrics.* CRC Press LLC, 1995.

[6] M. S. Dresselhaus, G. Chen, and M. Y. Tang. New directions for low-dimensional thermoelectric materials. *Adv. Mater. 19 (8), 1043-1053*, 2007.

[7] Terje Finstad. Electronic structure and functionality of thermoelectric materials workshop. *Reykjavik, Iceland*, 2007.

[8] D. M. Freik, Gaiducho.Gm, and S. P. Oleskiv. Forming conditions for thin semiconductor znsb films. *Izv Vuz Fiz+ (5), pp.147*, 1970.

[9] J. H. Goldsmid. *Thermoelectrics: Basic Principles and New Materials Developments*. Springer, 2001.

[10] J. H. Goldsmid. *Introduction to Thermoelectricity*. Springer, 2009.

[11] U. Haussermann and A. S. Mikhaylushkin. Electron-poor antimonides: Complex framework structure with narrow band gaps and low thermal conductivity. *Transactions 39 (4), 1036-1045*, 2010.

[12] Tao He, Jiazhong Chen, and H. David Rosenfeld. Thermoelectric properties of indium-filled skutterudites. *Chem. Mater. 2006, 18, 759-762*, 2006.

[13] J. P. Heremans, V. Jovovic, and E. S. Toberer. Enhancement of thermoelectric efficiency in pbte by distortion of the electronic density of states. *Science 321, 554*, 2008.

[14] H.Y.Fan H.Komiya, K.Masumoto. Optical and electrical properties and energy band structure of znsb. *PhysRev. Vol.133. A1679*, 1964.

[15] K.Masumoto H.Komiya and H.Y.Fan. The preparation and semiconducting properties of single crystals of $znsnas_2$ compound b. *Journal of Physics and Chemistry of Solids 26(1), pp.163-171*, 1965.

[16] K.Cenzual H.Okamoto. Zn-sb phase diagram. *ASM Alloy Phase Diagram Center*, 2007.

[17] N. L. Kostur and V. I. Psarev. Electrical properties of doped single crystals of znsb. *Izvestiya Vysshikh Uchebnykh Zavedenii Fizika (2), pp.39*, 1967.

[18] J. L. Martin, M. Goiran, and E. K. Arushanov. Far infrared magnetotransmission and hole crylotron resonance at high magnetic fields in p-znsb. *Physica B 177 (1-4), 481-484*, 1992.

[19] A. S. Mikhaylushkin, J. Nylen, and U. Haussermann. Structure and bonding

of zinc antimonides: Complex frameworks and narrow band gaps. *Chemistry-a European Journal 11 (17), 4912-4920*, 2005.

[20] J. P. Moore and R.S.Graves. Absolute seebeck coefficient of platinum from 80 to 340 k and the thermal and electrical conductivities of lead from 80 to 400 k. *Appl. Phys., 44 (3), 1174*, 1973.

[21] G. S. Nolas. *CRC Hand book of Thermoelectrics, pp. 33-31.* Taylor and Francis, CRC Press, 2006.

[22] G.S. NOLAS, X. LIN, and J. MARTIN. Open-structured materials: Skutterudites and clathrates. *LECTRONIC MATERIALS, Vol. 38, No. 7*, 2009.

[23] C. OKAMURA, T. Ueda, and K. Hasezaki. Preparation of single-phase znsb thermoelectric materials using a mechanical grinding process. *Mater. Trans. 51 (5), 860-862*, 2010.

[24] Lichang Qi Peichun Yang, Li Hou. Laser flash method for investigating the thermal diffusitivity of thin film. *Science and Techonology of New Diamond, pp.453-455*, 1990.

[25] P. Pichanusakorn and P. Bandaru. Nanostructured thermoelectrics. *Science and Engineering R R 67, 19-63*, 2010.

[26] O. Prytz, A. E. Gunnaes, and O. B. Karlsen. Nanoscale inclusions in the phonon glass thermoelectric materials zn_4sb_3. *Philosophical Magazine Letters 89 (6), 362-369*, 2009.

[27] P. Rogl. *Thermoelectrics Handbook: Macro to Nano, pp. 32-31.* Taylor and Francis, CRC Press, 2006.

[28] D. M. Rowe, editor. *Thermoelectrics Handbook: Macro to Nano.* Taylor and Francis, CRC Press, 2006.

[29] P. J. Shaver and J. Blair. Thermal and electronic transport properties of p-type znsb. *Physical Review 141 (2), pp.649*, 1966.

[30] G. J. Snyder, M. Christensen, and E. Nishibori. Disordered zinc in zn_4sb3 with phonon-glass and electron.crystal thermoelectric properties. *Nature Materials 3 (7), 458-463*, 2004.

[31] B. Streetman and S. Banerjee. *State Electronic Devices (6th Edition)*. Prentice Hall, 2007.

[32] J.-P.Fleurial T.Cailat, A.Borshchevsky. Thermal conductivity of $zn_{4-1}cd_xsb3$ solid solutions. *Materials Research Society Symposium Proceedings, pp103-8*, 1997.

[33] T. UEDA, C. OKAMURA, and Y. NODA. Effect of tellurium doping on the thermoelectric properties of znsb. *Japan Institute of Metals, Sendai, JAPON*, 2009.

[34] L.J. van der PAUW. A method of measuring the resistivity and hall coefficient on lamellar of arbitrary shape. *Philips Technical Review, Vol.20, pp.220-224*, 1958.

[35] A.I.Kolyubakin E.G.Ponyatovsky V.E.Antonov, O.I.Barkalov. Te znsb and gasb bulk amorphous semiconductors: Transport properties. *Physica Status Solidi B-Basic Research 198 (1), pp.497-501*, 1996.

[36] W.E.Resse W.J.Turner, A.S.Fischler. Physical properties of several ii-v semiconductors. *PhysRev.Vol.121. pp.759*, 1961.

[37] C. Y. Wu and W.D.Ken. A new computer-aided simulation model for polycrystalline silicon film resistors. *Solid State Electronics 26 (7), 675-684*, 1983.

[38] Moser Z. Zn-cr phase diagram. *ASM Alloy Phase Diagram Center*, 1992.

[39] L. T. Zhang, M. Tsutsui, and K. Ito. Effects of znsb and zn inclusions on the thermoelectric properties of β-zn_4sb_3. *Journal of Alloys and Compounds 358 (1-2), 252-256*, 2003.